Activity and Selectivity of Transition Metal (Fe, Mo and W) Carbides in the Fischer-Tropsch Synthesis

By

Veronica A. Patterson

B.Sc. Industrial Science

Submitted to the University of Cape Town in partial fulfilment of the requirements for the degree of

Master of Science in Applied Science

Department of Chemical Engineering
University of Cape Town
P/B Rondebosch
7701
South Africa

April 2007

Acknowledgements

I would like to thank Eric van Steen for his support, advice and encouragement throughout this work. He has a lot to teach and I have a lot to learn. This would not have been possible without him.

Thanks to Sasol for financial support and allowing me to make use of their facilities for this research. To my mentor, for always keeping me on my toes and helping me when I need it the most, I am most grateful.

Thanks to the iThemba labs for making the XRD facilities available to me.

The entire Centre for Catalysis Research, students and staff, you guys are great. It's been fun working with you all.

My family, who didn't always know what this was all about, only that this is important to me, thanks for all your prayers and support. You were always so patient. It's wonderful having a place I can be at home, right there with you. All my friends...wow, with friends like these, who needs enemies.

Synopsis

This study focussed on the Fischer-Tropsch activity and selectivity of transition metal (iron, molybdenum and tungsten) carbides. The carbide catalysts were prepared by a temperature programmed method. The properties of the materials were characterised by X-ray diffraction (XRD), transmission electron microscopy (TEM), BET measurements and temperature programmed desorption of carbon monoxide (CO-TPD). The performance of the materials was tested in a Berty reactor. A reduced, precipitated iron oxide catalyst was used as a reference catalyst.

Characterisation results show that the preparation method used in this study only resulted in a phase pure WC. Molybdenum carbide was a mixture of Mo_2C and other carbide phases (α-MoC_{1-x}). The iron catalyst prepared was a mixture of metallic iron and cementite (Fe_3C).

Fischer-Tropsch synthesis was carried out at typical high temperature conditions (T=330 °C, P=20 bar, H_2/CO=4) with CO_2 co-fed in the reaction. A higher Fischer-Tropsch activity was observed over the metallic iron/iron carbide catalyst mixture than on the early transition metal carbides, with molybdenum carbide showing a slightly higher activity than WC. It was postulated that the observed activities were a function of the electronic structure of the metal carbides, and therefore the strength of the resulting metal-carbon bond following CO adsorption. The number of valence electrons on the metals was used to explain this difference in activity. The slightly lower activity observed on the tungsten carbide than on the molybdenum carbide could be explained by the additional electron shell on the tungsten metal, compared to the molybdenum carbide. It was postulated that in WC, the additional electron shell hinders the adsorption of CO, so that Fischer-Tropsch activity is slightly reduced.

The product selectivity on the carbidised iron-based catalyst was more favourable, i.e. lower methane selectivity and higher chain growth probability.

The early transition metal carbides facilitated higher methane selectivity, and chain growth probabilities of less than 0.45 were observed for these two carbide catalyst. The olefin content of the product over these materials was also found to be lower than in the iron carbide/metallic iron catalyst, with the level of 1-olefins in this olefinic product also considerably lower than on the carbidised iron-based catalyst. These observations could be explained by the availability of surface hydrogen on the catalysts. High availability of surface hydrogen on the surface, due to less strong CO-adsorption results in high methane selectivity, low chain growth probability, low olefin content and low 1-olefin content.

Table of Contents

List of Figures

List of Tables

1. Introduction

Transition metal (iron, molybdenum and tungsten) carbides have been reported to show catalytic activity in reactions such as hydrogenation (e.g. in CO-hydrogenation). The carbides of molybdenum and tungsten have the observed activity due to the combination of the electrons of the carbon with the metal (Oyama, 1992a). This results in a resemblance of these compounds to the Group VIII metals (e.g. Pt) in physical properties as well as catalytic activity in some reactions (Vidick et al., 1986). Iron carbide has been shown to be the most abundant phase present in an iron-based Fischer-Tropsch catalyst (Malan et al., 1961).

1.1 Fischer-Tropsch synthesis

The Fischer-Tropsch process is the synthesis of long chain hydrocarbons and other aliphatic compounds from synthesis gas. The process is named after F. Fischer and H. Tropsch, the German coal researchers who discovered it in 1923. The process can be generally represented as:

$$CO + 2H_2 \rightarrow 1/n\ (CH_2) + H_2O \qquad \Delta H_{rxn} = -140\ kJ/mol\ (250\ °C) \qquad (1)$$

where the heat of reaction is an approximate value dependent on the average chain length of the product formed.

Synthesis gas, a mixture of hydrogen and carbon monoxide, is industrially reacted in the presence of an iron or cobalt based catalyst. Products such as methane, synthetic gasoline and waxes, and alcohols are formed. Water and/or carbon dioxide through the water-gas shift reaction (Patzlaff et al., 1999) are produced as a major by-product. Water-gas shift activity is mainly observed with iron-based catalysts.

$$H_2O + CO \rightarrow CO_2 + H_2 \qquad \Delta H_{rxn} = -39.5\ kJ/mol\ (250\ °C) \qquad (2)$$

The Fischer-Tropsch process is performed at two different regimes (Dry, 2002), namely high temperature and low temperature. In the high temperature Fischer-Tropsch synthesis (P~20 bar; T~300-350 °C), mainly hydrocarbons in the range of C_1-C_{20} are produced, i.e. products in the gasoline boiling range, low molecular weight olefins and some oxygenates. The low temperature process (P~20 bar; T~220-240 °C) is mainly used for the production of high molecular weight linear waxes (Dry, 2002).

1.1.1 Reaction pathways in the Fischer-Tropsch synthesis

The Fischer-Tropsch synthesis is a polymerisation reaction, in which the monomers are being produced in-situ from the gaseous reactants hydrogen and carbon monoxide. Thus, all reaction pathways proposed in literature will have three main reaction steps, i.e.

1. generation of the chain starter (initiation)
2. chain growth (propagation)
3. desorption (termination)

Numerous reaction pathways have been proposed to explain the observed product distribution in the FT synthesis. It can be assumed that not a single reaction pathway exists on the catalyst surface during the FT synthesis, but that a number of parallel operating pathways will exist. The four most popular mechanisms are the 'alkyl', 'alkenyl', 'enol' and 'CO-insertion' mechanisms (Claeys and van Steen, 2004).

The alkyl mechanism is presently the most widely accepted mechanism for chain growth in the FT synthesis (Claeys and van Steen, 2004). Chain initiation takes place via dissociative CO-chemisorption, by which surface carbon and surface oxygen is generated. Surface oxygen is removed from the surface by reaction with adsorbed hydrogen yielding water or with adsorbed carbon monoxide yielding carbon dioxide. Surface carbon can be subsequently hydrogenated yielding in a consecutive reaction CH, CH_2 and CH_3 surface species. The CH_3 surface species is regarded as the chain

initiator, and the CH_2 surface species as the monomer in the reaction scheme. Chain growth is thought to take place by successive incorporation of the monomer, CH_2 surface species. Product formation takes place by either β-hydrogen abstraction or hydrogen addition yielding 1-olefins and n-paraffins as primary products (Fischer and Tropsch, 1926; Craxford and Rideal, 1939).

In the alkenyl mechanism (Maitlis et al., 1996, 1999), the formation of the first C-C bond is thought to occur through the coupling of methylidyne (CH) and methylene (CH_2) to form a vinyl surface species ($CH=CH_2$), which is considered as the chain initiator. Chain propagation involves the addition of a methylene species to a surface vinyl species, yielding a surface allyl species. This is followed by an allyl-vinyl isomerisation forming a surface alkenyl species. Product desorption involves the hydrogen addition to an alkenyl species yielding 1-olefins.

In the enol mechanism (Storch et al., 1951), chemisorbed CO is hydrogenated to enol surface species. Chain growth occurs through a condensation reaction between enol species under elimination of water. The occurrence of branched hydrocarbons is thought to originate from the involvement of a CHROH surface species. Termination of the chain growth process of desorption yield oxygenates and 1-olefins.

In the CO-insertion mechanism (Pichler and Schulz, 1970) chemisorbed CO is the monomer. The chain initiator is thought to be a surface methyl species. Chain growth takes place by CO-insertion in a metal-alkyl bond leading to a surface acyl species. The elimination of oxygen from the surface species leads to the formation of the enlarged alkyl species. Product desorption can take place by hydrogen addition and β-hydrogen elimination of the alkyl or oxygen containing surface species, leading to the formation of n-paraffins, 1-olefins, aldehydes and alcohols.

1.1.1.1 Products of Fischer-Tropsch synthesis

A variety of products of different chain length with different functionality is formed in Fischer-Tropsch synthesis. The actual composition/product distribution of a Fischer-Tropsch process depends on reaction variables such as temperature and partial pressures of the reactants and product water, the reactor system used, as well as the properties of the catalyst. The main products of the FT synthesis are (Claeys and van Steen, 2004):

- n-olefins (mainly α-olefins, but also olefins with internal double bonds)
- n-paraffins

Typical side-products are:

- oxygenates (1-alcohols, aldehydes, ketones, carboxylic acids)
- branched compounds (mainly mono-methyl branched)

Only in high temperature processes fairly large amounts of branched compounds and aromatic compounds are formed.

1.1.1.2 Product distributions

The variety of compositions of Fischer-Tropsch products comprising of hundreds of individual compounds shows a remarkable order with regard to the class and size of the product compounds (Schulz and Claeys, 1999). A number of kinetic models for the Fischer-Tropsch product distribution have been developed. The Anderson-Schulz-Flory distribution is the simplest of these kinetic models (Schulz and Claeys, 1999).

The basis of the Anderson-Schulz-Flory (ASF), as well as all the other polymerisation kinetics, is the generally accepted principle that Fischer-Tropsch reaction proceeds via the addition of a C_1 monomer (Schulz and Claeys, 1999). The carbon number dependency of the product distribution can be described by:

$$M_N = (1-\alpha).\alpha^{N-1} \qquad (3)$$

if the rate of addition of C_1 monomers relative to the rate of desorption is independent of the carbon number of the growing chain. M_N is the mole fraction of the products with carbon number N and α is the chain growth probability. The so-called Anderson-Schulz-Flory plots are obtained by plotting M_N versus N on a semi-logarithmic plot, yielding a linear relationship, from which the chain growth probability is obtained.

The noted empirical deviations of the Fischer-Tropsch product distribution from the theoretically predicted ASF product distributions are:

- Higher than expected methane content i.e. low chain growth probability for C_1 surface species (Schulz et al., 2002)
- Relatively low ethene yield, which has been explained by strong re-adsorption of ethene leading to chain initiation and chain growth (Schulz and Claeys, 1999; Schulz et al., 2002)
- Increase in chain growth probability in the range C_7-C_8, indicative of increasing n-olefin readsorption for further chain growth (Schulz et al., 2002).

The high temperature Fischer-Tropsch (HTFT) synthesis is performed at conditions where condensation of higher carbon number products does not take place (Dry, 1996). This leads to decreased readsorption of higher carbon number olefins and therefore less secondary chain growth of these products.

1.1.2 Catalysts for Fischer-Tropsch synthesis

Extensive work has been done investigating the activity of Group VIII metals as Fischer-Tropsch catalysts. Vannice (1975) ranked the performance of alumina supported metals in terms of specific activity and selectivity as Fischer-Tropsch catalysts under various conditions at a total pressure of 1 atm. All Group VIII metals were reported to show some Fischer-Tropsch activity. Considering the specific activities of the current Fischer-Tropsch

catalysts, the specific activity of iron was placed higher than that of cobalt. In terms of average molecular weight of the hydrocarbon product the following sequence was obtained: Ru > Fe > Co > Rh > Ni > Ir > Pt > Pd.

The current industrially employed catalysts are iron or cobalt based catalysts, since they are amongst the most active and selective catalytically active metals, which are not too expensive. The cobalt-based catalyst is only used in low temperature (220-250°C) Fischer-Tropsch processes, while iron-based catalysts are used in both low and high temperature (330-350°C) applications.

1.1.3 Iron-based catalysts

The industrial cobalt-based catalyst is thought (Iglesia, 1997) to be active for the Fischer-Tropsch synthesis in its metallic form. The iron catalyst, on the other hand, is believed to be active in the carbide phase (Shroff et al., 1995; Biel, 2005), even though this is still debated (Li et al., 2001).

Malan et al. (1961) showed the phase composition of the iron catalyst as a function of time on stream in the Fischer-Tropsch synthesis (see Figure 1.1). The reduced catalyst contained α-Fe, which transformed rapidly into Hägg carbide, cementite and magnetite. The oxide phase Fe_3O_4 became more dominant with increasing time on stream, whereas the presence of carbide became less. Furthermore, Hägg carbide transforms into Eckstrom-Adcock carbide. It is indicated that with time on stream, the carbide phases become enriched with carbon (i.e. cementite → Hägg carbide → Eckstrom-Adcock carbide).

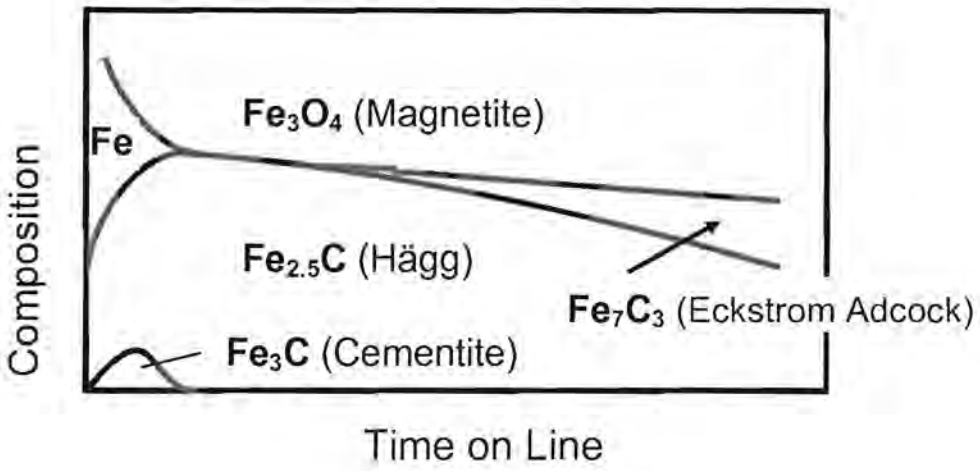

Figure 1.1: Phase change in iron-based catalyst as a function of time-on-line (redrawn from Malan et al., 1961)

It is well known that the distribution of iron phases of the catalyst changes with time on stream during the Fischer-Tropsch synthesis. For example, the metallic iron phase is mainly formed if the catalyst is reduced by H_2, which is readily converted to a mixture of iron carbides and Fe_3O_4 under reaction conditions (Dry, 1981). Although the active phase for the FTS reaction is still in debate, the oxidation of the metallic iron and/or the iron carbide phases is believed as one of the factors of catalyst deactivation. H_2O (the primary product in the Fischer-Tropsch synthesis reaction) is usually considered as an oxidising agent for these zero-valent iron phases (Dry, 1981). Apart from the oxidation of iron phases, several authors have pointed out the importance of graphite-like carbonaceous deposits on the deactivation of the iron catalyst (Niemantsverdriet et al., 1980; Dwyer and Hardenberg, 1984; Loaiza-Gil et al., 1999).

There is some uncertainty as to which phase of an industrial iron catalyst is active for Fischer-Tropsch synthesis. Herranz et al. (2006) suggested that Hägg carbide is the most active phase of iron carbide in Fischer-Tropsch synthesis. They performed different activation procedures, yielding either cementite or Hägg carbide as the dominant phase in the catalyst. These catalysts were tested using a fixed-bed reactor at 573 K and 10.1 bar.

Cementite was formed after pre-treatment with CO, while Hägg carbide was formed after pre-treatment with synthesis gas. It was found that the carbon monoxide conversion over the cementite was only 37% while over Hägg carbide it was 74%, while the two catalysts yielded similar products. The other notable difference was that the hydrocarbon production (CH_4 free) was higher on the Hägg carbide.

It was observed that, under Fischer-Tropsch conditions, cementite species can evolve into Hägg carbide, although the transformation is still incomplete after 10 000 minutes. This observed phase evolution is expected based on the results by Malan et al., (1961).

In a recent study, the deactivation of an iron catalyst was investigated. Ning et al. (2006) tested precipitated iron catalysts with and without additives (Zn, K, Cu) in a fixed bed reactor at 503 K and 16 bar. The catalysts were pre-treated by CO. For the pure iron catalyst, the CO conversion reached a maximum at 8 hours on stream, while an increasing conversion was observed when Zn, K and Cu were added simultaneously. X-ray diffraction analysis showed the formation of iron carbides (Fe_5C_2 and Fe_xC) after the CO pre-treatment, and for the pure iron catalyst, the oxidation of these carbides to Fe_3O_4. For the catalyst containing all the additives simultaneously, however, iron carbides were the only phases detected even after 29 hours on stream. Amorphous graphite-like carbonaceous compounds were not detected using laser Raman spectroscopy. These authors therefore suggested that oxidation of the iron carbides by H_2O is the main reason for the deactivation of the iron Fischer-Tropsch synthesis catalyst. The catalyst containing Zn, K, and Cu showed a higher CO_2 selectivity, indicating improved water-gas shift activity and thereby suppressing oxidation of the iron carbides. They, however, did not report on the partial pressure of water, as this parameter would confirm the improved water-gas shift activity that was reported.

1.1.4 Transition metal carbides

Early transition metal carbides have also been studied by several groups as catalysts for the Fischer-Tropsch synthesis. Patterson et al. (2003) compared the performance of the face centred cubic (fcc) phases of molybdenum and tungsten carbides in a continuously stirred tank reactor at a pressure of 20 bar over a temperature range of 494-573 K. The maximum carbon monoxide conversion on the molybdenum carbide catalyst was 40% while on tungsten carbide it was about 18%, under certain operating conditions. The authors reported a high water gas shift activity, especially in molybdenum carbide. The main hydrocarbon product was methane, thus indicating a low chain growth probability. The early transition metal carbides seem to show some activity to Fischer-Tropsch synthesis.

1.1.4.1 Stability of transition metal carbides under Fischer-Tropsch conditions

A thermodynamic analysis gives insight into the stability of transition metal carbides under Fischer-Tropsch conditions. In studying the phase stability of the metal carbides during the Fischer-Tropsch synthesis, the operating conditions under which the crystallites will still be in the carbide phase under reaction conditions can be defined.

These thermodynamic studies are carried out for bulk materials. The surface energy contribution of the crystallites will influence the phase stability. The contribution of surface energy becomes more important for crystallites in the nanometer range. The effect of the surface energy should therefore be diminished by working with relatively large crystals. The stability of large crystallites approximates the bulk materials for which the calculations are carried out.

It is therefore important to do a complete thermodynamic analysis of the metal carbides under Fischer-Tropsch conditions.

The conditions in the Fischer-Tropsch reactor are oxidising due the presence of CO_2 and H_2O. It is therefore anticipated that the metal carbides can be oxidised. Typical oxidation equations expected for iron carbide under Fischer-Tropsch conditions are shown below:

$Fe_3C + 5CO_2 \rightarrow Fe_3O_4 + 6CO$ (4)

$Fe_3C + 4CO_2 \rightarrow FeO + 5CO$ (5)

$2Fe_3C + 11CO_2 \rightarrow 3Fe_2O_3 + 13CO$ (6)

A similar set of oxidation equations can be set up for molybdenum and tungsten carbides.

$Mo_2C + 7CO_2 \rightarrow 2MoO_3 + 8CO$ (7)

$Mo_2C + 5CO_2 \rightarrow 2MoO_2 + 6CO$ (8)

$Mo_2C + 3CO_2 \rightarrow 2MoO + 4CO$ (9)

$WC + 4CO_2 \rightarrow WO_3 + 5CO$ (10)

$WC + 3CO_2 \rightarrow WO_2 + 4CO$ (11)

Thermodynamic data for the species involved have been put together to calculate the various phases that will be present at different conditions. Thermodynamic information is graphically shown in Figures 1.2-1.4.

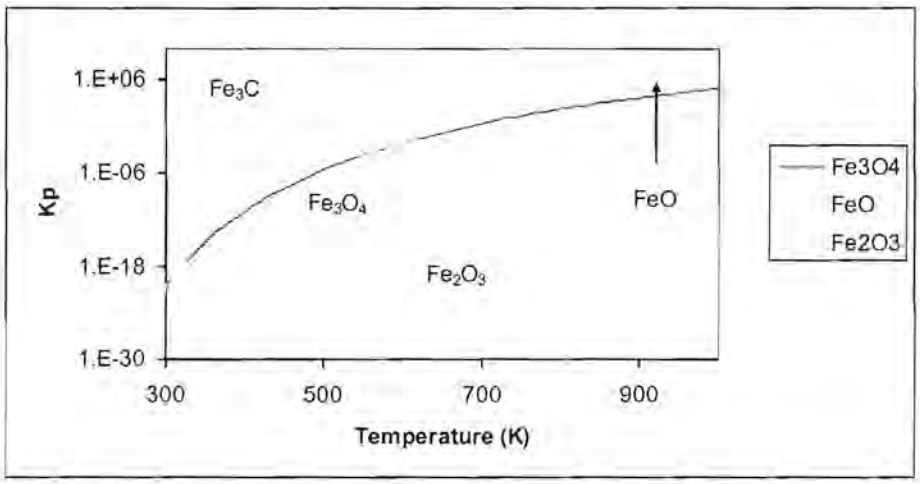

Figure 1.2: Thermodynamic equilibrium plot for Fe_3C oxidation by CO_2 (Thermodynamic data from Knacke et al., 1991)

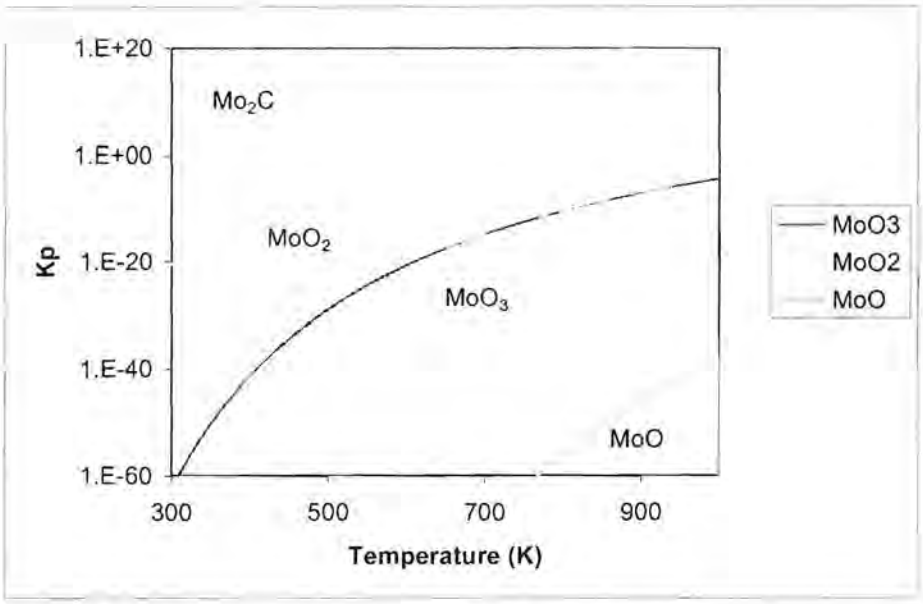

Figure 1.3: Thermodynamic equilibrium plot for Mo_2C oxidation by CO_2 (Thermodynamic data from Knacke et al., 1991)

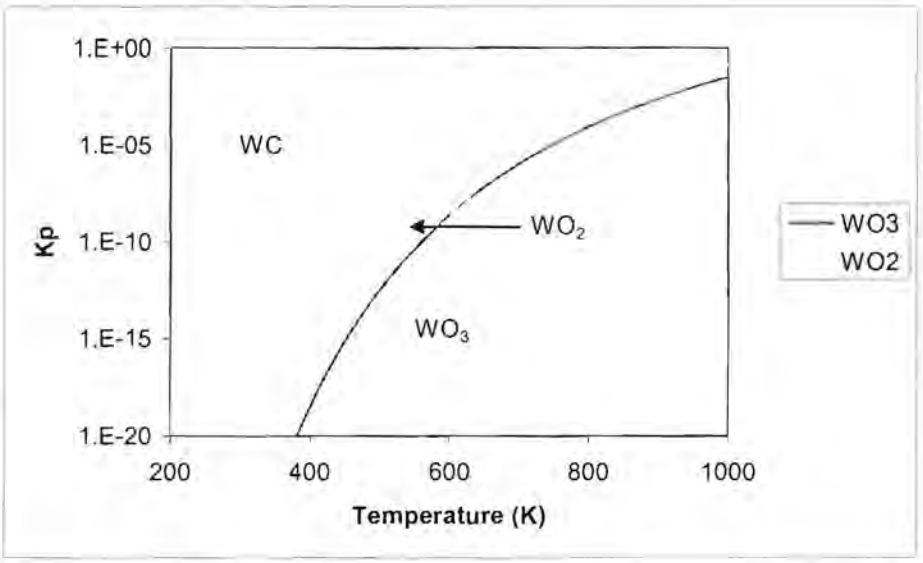

Figure 1.4: Thermodynamic equilibrium plot for WC oxidation by CO_2 (Thermodynamic data from Knacke et al., 1991)

These transformations could also result from H_2O oxidation if the favourable direction of the water-gas shift reaction is such that the partial pressure of water is higher than that of carbon dioxide. The occurrence of these phase

transformations in the catalysts could result in falsification of the reported results.

1.1.5 Potassium promotion on transition metals

Iron-based catalyst is industrially operated with a potassium promoter for Fischer-Tropsch synthesis. The effect of the potassium on the catalyst surface is believed to increase the electron density, resulting in the enhanced formation of unsaturated products such as olefins and oxygenates in longer chain hydrocarbon products.

In a study on the reaction kinetics for Fischer-Tropsch synthesis (Eliason and Bartholomew, 1999), rate data on unpromoted and potassium promoted iron catalysts were obtained. The catalysts were tested at 10 atm total pressure over a range of temperatures (200 – 240 °C) and H_2/CO ratios. These authors reported higher CO conversions, olefin content (C_2-C_4) and chain growth probabilities at $H_2/CO = 1$ for the promoted catalyst. It was postulated that potassium increases the strength of CO adsorption on the catalyst surface.

Luo and Davis (2003) studied the effect of a potassium promoter on the product selectivity and CO conversion over an iron-based Fischer-Tropsch catalyst compared to the unpromoted catalyst. These catalysts were tested in a CSTR at 270 °C and 13 bar. They obtained an 18% higher CO conversion on the promoted catalyst than the unpromoted iron catalyst. The olefin content in the C_2-C_4 fraction showed a significant increase with the addition of potassium, especially in C_2. The chain growth probability of the promoted catalyst was also found to be higher.

In a different study, charcoal supported molybdenum catalysts were also investigated as Fischer-Tropsch catalysts (Dun et al., 1985). The catalyst was tested in a fixed bed reactor at a pressure of 1.2 bar and a temperature of 573 K. The authors report a high activity in the unpromoted catalyst towards C_1-C_3 hydrocarbons. The activity of the potassium promoted molybdenum catalyst

was moderately reduced, while the selectivity shifted towards C_2-C_3 hydrocarbons.

Bian et al. (1998) studied the effects of Mo loading on a K-MoO_3/γ-Al_2O_3 catalyst. They tested the catalysts in a fixed bed reactor at 50 bar and 593 K. The total yields of mixed alcohols and hydrocarbons decreased, but with increasing Mo loading the selectivity towards mixed alcohols increased sharply, from 3% to 50%. The authors did not study the effect of potassium loading on the products, since this promoter was added at a constant loading.

It can be seen that the effect of potassium promotion is strongly dependent on the conditions of the catalyst testing in molybdenum-based catalysts. It is inconclusive from the literature what the effect of potassium promotion will be on a bulk molybdenum or tungsten carbide catalyst.

In one study, the use of a potassium promoter for a face centred cubic (fcc) and hexagonal close packed (hcp) molybdenum carbide catalyst was investigated (Woo et al., 1991). The experiments were done in a tubular down flow fixed-bed reactor system at a pressure of 80 bar and a temperature of 573 K. These authors found that without potassium promoter the main hydrocarbons were C_1-C_{12}. The promoter significantly enhanced the selectivity to alcohols of linear C_1-C_7.

1.2 Early transition metal nitrides and carbides

The alloying of main group elements, such as C, N, or O with early transition metals produces a class of materials known as carbides, nitrides, or oxycarbide/nitrides (Toth, 1971; Storms, 1967; Oyama, 1992c). These materials have high melting points (> 3300K), hardness (> 2000 kg mm^{-2}) and strength (> 3 × 10^5 MPa) (Toth, 1971; Oyama, 1996) and are employed commercially in advanced structural and cutting tool applications. Interestingly, although their physical properties are those of refractory ceramics, their electronic and magnetic properties are typical of metals. Thus,

they are good conductors of heat and electricity and have Hall coefficients, magnetic susceptibilities, and heat capacities similar to those of metals (Toth, 1971).

Monometallic carbides and nitrides often adopt simple crystal structures with the metal atoms arranged in cubic close-packed (ccp), hexagonal close-packed (hcp) or simple hexagonal (hex) arrays. The non-metallic elements, C, N and O, occupy interstitial spaces between metal atoms, and for this reason the materials are also known as interstitial alloys (see Figure 1.5).

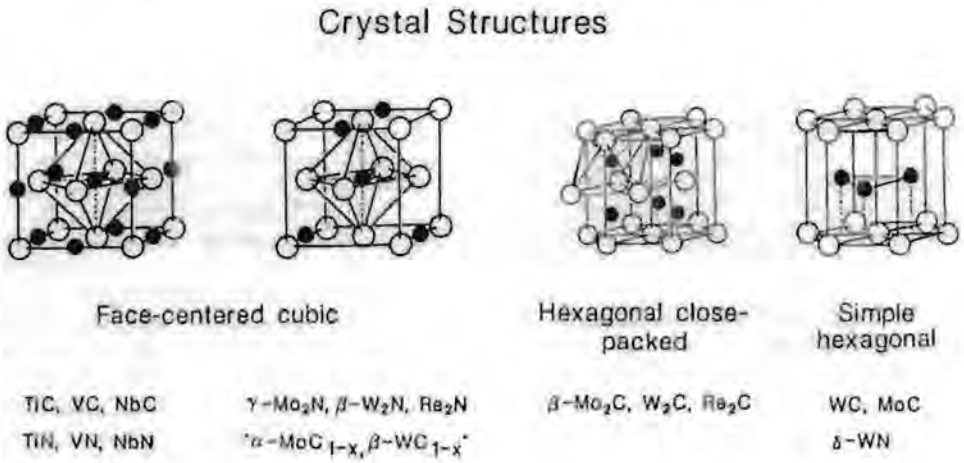

Figure 1.5: Typical crystal structures and compositions of nitrides and carbides (Reproduced from Oyama, 1992c)

The crystal structures adopted by the binary carbides and nitrides are similar to those found in noble metals. The resemblance is not coincidental, and has been explained using Engel-Brewer valence bond theory (Oyama, 1992a).

According to the Engel-Brewer valence bond theory (Engel, 1939; Brewer, 1967), crystal structure is determined by the number of outer-shell *sp* electrons per atom (e/a). Thus, for up to 1.5 *sp* e/a the bcc structure is obtained, for 1.7-2.1 e/a the hcp structure is produced, and for 2.5-3 e/a the ccp structure is attained. The number of *sp* electrons may be deduced from compilations of promotion energies determined from spectroscopic data or predictions (Brewer, 1984).

Oyama (1992a) investigated the trends in melting points, stoichiometry, and crystal structures of early transition metal carbides in terms of the Engel-Brewer valence bond theory. It was postulated that nitrogen and carbon combines its valence *sp* electrons with the metal *spd* bands to increase the metal's effective s-p count. The result of this combination of electrons is that crystal structure and chemical reactivity of the compounds resemble those of elements further to the right in the periodic table. These metal carbides therefore have excellent catalytic activity in a wide variety of reactions, such as methanation (Ranhotra et al., 1987), ammonia synthesis (Boudart et al., 1980), ammonia decomposition (Oyama, 1992b), hydrocracking (Lee et al., 1987), hydrogenation of benzene and cyclohexene (Lee et al., 1991) and hydroisomerisation of n-hexane (Ledoux et al., 1992), n-heptane (Ribeiro et al., 1991a) and methylcyclohexane (Ribeiro et al., 1991b). Considerable work has also been done in the area of hydroprocessing (Schlatter et al., 1988), where these materials have been shown to have high activity for both hydrodesulfurisation (HDS) (Markel et al., 1990; Nagai and Miyao, 1993) and hydrodenitrogenation (HDN) (Lee et al., 1993; Sajkowski and Oyama, 1996; Colling and Thompson, 1994).

1.2.1 Thermodynamic considerations in the preparation of nitrides and carbides

Strategies for the preparation of metal nitrides and carbides are numerous and involve widely differing starting metallic compounds, as well as different nitrogen and carbon sources. It is therefore instructive to consider the thermodynamics (Oyama, 1996) of various kinds of transformations.

Thermodynamic considerations are useful for determining conditions for nitridation and carbidisation. For example, in the nitridation of niobium the particular phase of the product (e.g. NbN, β-Nb_2N, or γ-Nb_4N_3) will depend on the temperature and pressure (Oyama, 1997). This holds true also for carbides. However, for carbides, competing reactions such as

$$2CO \rightarrow C + CO_2 \qquad (12)$$

$CH_4 \rightarrow C + 2H_2$ (13)

need to be taken into account, since they yield free carbon. These side reactions can be controlled by properly adjusting the gas composition by means of ratios of reactant gases such as $(CO)/(CO_2)$ or $(CH_4)/(H_2)^2$. Examples are given for WC and Mo_2C synthesis in Figure 1.6.

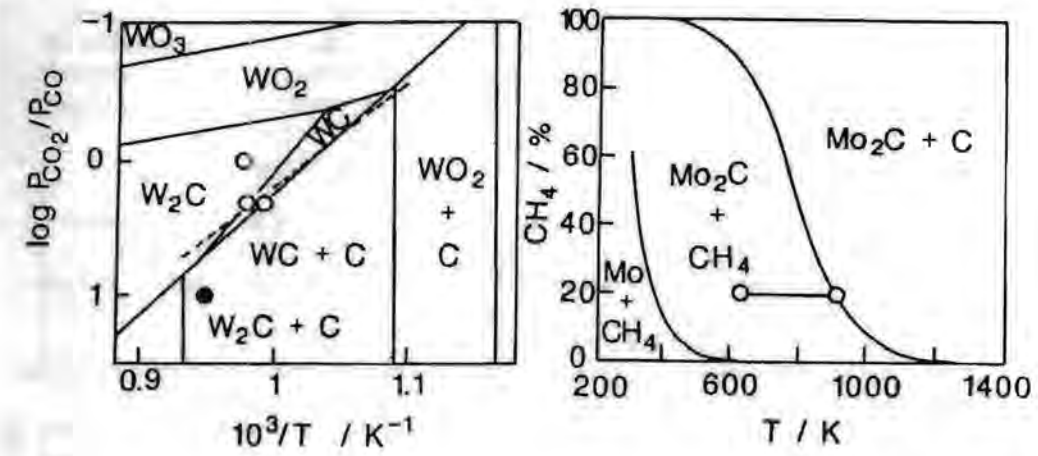

Figure 1.6: Equilibrium curves for the carbidisation of tungsten and molybdenum. The tungsten diagram shows experimental points for W_2C (open circles) and WC (solid circle). The molybdenum diagram shows the operating line for synthesis with 20% CH_4 in H_2 (reproduced from Oyama, 1992c)

These thermodynamic considerations are not limiting (except for free carbon deposition) as the synthesis can be carried out at non-equilibrium conditions. For example, in the nitridation or carbidisation of oxides it is possible to lower the temperature of reaction by sweeping away the product gases (Kapoor and Oyama, 1992):

$MO + H_xC_y \rightarrow MC + H_2O + CO$ (14)

$MO + NH_3 \rightarrow MN + H_2O + (1/2)\ H_2$ (15)

Water vapour produced during reaction is particularly problematic as it can inhibit the reaction or lead to hydrothermal sintering. Water vapour retards the synthesis process by inhibiting reduction. Thus for the same extent of reaction, higher temperatures are required (Kapoor and Oyama, 1992).

1.2.2 Temperature programmed preparation methods of nitrides and carbides

The temperature programmed reaction (TPR) method of preparation (Oyama, 1981) is a variation of the isothermal method. The TPR method consists of treating an oxide precursor in a reactive gas stream while raising the temperature in a uniform manner. By monitoring changes in the exit gas-phase composition, the end of the reaction can be ascertained and the product quenched. Because the synthesis involves direct transformation of an oxide to a nitride or carbide, it is possible to bypass the metallic state, which is the most prone to sinter (lowest Tamann temperature). In addition, the use of the temperature program allows an optimal balance between synthesis and sintering rates and results in products with high specific surface areas (S_g).

The resulting high surface areas are due to the topotactic transformation according to which the transformation of oxide to nitride takes place (Volpe and Boudart, 1985c). In this process nitrogen replaces oxygen in the lattice with minimal disruption of the metal atoms, so that in the case of molybdenum, the product γ-Mo_2N(100) planes are parallel to the original parent MoO_3(010) planes. Because of the density differences each original MoO_3 crystallite is transformed into a sponge-like porous agglomerate of γ-Mo_2N micro-crystals, retaining the original external size and shape of the MoO_3 parent. This retention of external morphology is known as pseudomorphism. Because of the gradual replacement of oxygen by nitrogen, there is a continuous transformation through oxynitride compositions.

The same process can be repeated using WO_3 as the starting material to produce β-W_2N. Interestingly, both the γ-Mo_2N and β-W_2N can be converted by topotactic transformations to the corresponding carbides of the high-temperature cubic structure, α-MoC_{1-x} (fcc) and α-WC_{1-x} (fcc), with $x \approx 0.5$. These phases retain the high surface area of their parent nitrides (Volpe and Boudart, 1985b; Lee et al., 1988).

1.2.2.1 Catalyst preparation

The method for the preparation of the metal carbides was proposed by Boudart and co-workers (Volpe and Boudart, 1985 a; Volpe and Boudart, 1985 b; Lee et al., 1987, 1988). This method is the temperature programmed reaction procedure for the preparation of high surface area face centred cubic crystallites.

The starting material is a high purity metal oxide. The carbide is prepared in a two step process. The first step is the nitridation of the metal oxide by reacting it in flowing ammonia and heating it at a certain ramp rate. The reaction is then rapidly quenched.

The second step is the carbidisation of the metal nitride. In this step the sample is heated at a ramp rate in a flowing methane-hydrogen mixture without removing the metal nitride from the reactor. The gas is then switched to an inert gas and quenched rapidly. The sample can finally be passivated using 1% oxygen in helium at 298 K.

1.3 Project objectives

In this study, the specific activity and selectivity of transition metal carbides will be determined for the Fischer-Tropsch synthesis.

The investigation of Fischer-Tropsch synthesis using iron, molybdenum and tungsten carbides as catalysts is to be carried out since this study will provide a foundation for the comparison of these metal carbides with the industrial Fischer-Tropsch catalysts, even though the effect of promoters will not be investigated. Early transition metals have been investigated as Fischer-Tropsch catalysts before (Patterson et al., 2003), but a detailed product distribution for low conversion reactions, and the activity per unit surface area, was not reported to allow for meaningful comparisons. If other transition metal carbides have been tested, it might be possible to determine the Fischer-

Tropsch activity and selectivity of these catalysts as a function of their electronic structure.

The investigation will deal only with the metal carbides prepared by the temperature programmed reaction method. It is important that the prepared carbides have large crystallites to promote phase stability in the Fischer-Tropsch environment. A precipitated iron oxide catalyst will be tested as a base case study for the carbides. The experiments will be performed below the limiting conversions to prevent oxidation of the carbides. Since the product selectivity depends strongly on the temperature and pressure, the experiments will be carried out at fixed temperature, pressure and H_2/CO feed ratio comparable to industrial operating conditions.

2. Experimental

2.1 Preparation of metal carbides

2.1.1 Metal oxide precursors

2.1.1.1 Iron oxide

The iron oxide was prepared by the reverse precipitation method. 161.3 g of iron nitrate nonahydrate (Aldrich) was dissolved in 400 ml of deionised water. The solution was heated to 80 °C. 100 ml of 25% solution of ammonium hydroxide (Unilab, Saarchem) was heated to 60 °C. The warm ammonium hydroxide solution was then poured into the iron nitrate solution under rapid stirring. The ammonium hydroxide was insufficient to cause precipitation, so more of the cold solution was added drop wise (about 5 ml) until a precipitate was formed. The solution was then stirred further for 15 minutes. The final pH of the solution was 7.5. The filtration and washing of the precipitate to remove the nitrates was omitted. The sintering that could result from the decomposition of nitrates in the heating process was acceptable, since large crystallites were desired (for stability under reaction conditions). The slurry was then poured into flat enamel or porcelain containers and placed in an oven at 120 °C overnight. The dried pieces were then broken up into smaller pieces (approximately 1 cm^2) and placed into a porcelain dish.

The dish was placed into a calcination oven and was calcined in air. The heating profile was as follows: 25 °C to 150 °C in 30 minutes and kept isothermal for 45 minutes, 150 °C to 230 °C in 30 minutes and kept isothermal for 45 minutes and then finally 230 °C to 400 °C in 30 minutes where it was kept isothermal for 4 hours before cooling down to room temperature. The product was then removed and crushed using a mortar and pestle to a particle size below 125 µm. This product was stored in a dessicator with silica gel as drying agent until it was used.

This procedure was repeated to prepare an additional iron oxide. This preparation was done in the Sasol laboratories. The only difference in this method from that used in the first preparation was that the drying was done at 150 °C.

2.1.1.2 Molybdenum oxide

Molybdenum trioxide was prepared by calcining 20 g of ammonium molybdate (Univar, Saarchem) in air by heating it to 330 °C in 2 hours and then keeping it isothermal at 330 °C for a further 4 hours. The calcination of air was done in a glass reactor in a furnace with a flow rate of air of 480 ml(STP)/min.

2.1.1.3 Tungsten oxide

Tungsten trioxide (Fluka) was calcined in air by taking the temperature up to 330 °C in 3 hours and then held isothermal for a further 3 hours. The flow rate of air was 480 ml(STP)/min. This calcination was merely done to remove all impurities and moisture from the powder.

2.1.2 Metal nitride intermediates

The transformation of the oxides into nitrides was performed in a quartz cell (see Figure 2.1) which was 310 mm in length and had an outer diameter of 65 mm. The sample bed had a diameter of 34 mm and was 210 mm in length. The outer bed had a side arm fitted at the top, at which the feed gases entered the system. There was a 30 mm coarse fritted disk at the bottom of the sample bed. This reactor was then placed in a tubular vertical furnace. A K-type thermocouple was placed in the porcelain heating cylinder within the surrounding furnace.

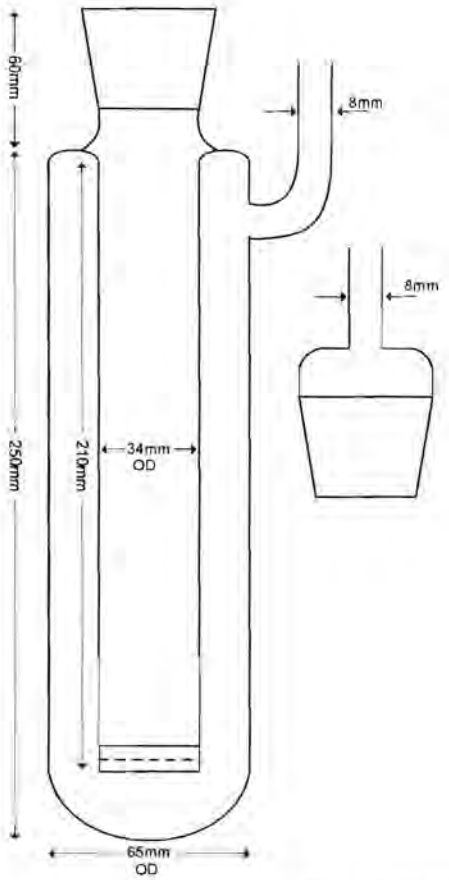

Figure 2.1: Quartz cell used in the set-up for catalyst preparation

Ammonia (Air products, 99.999%) was passed through the bed of metal oxide sample at an upward flow rate of 400 ml(STP)/min. The gas inside the reactor was at atmospheric pressure. The heating profile used is given in Table 2.1. The heating profiles for the transformation of molybdenum and tungsten oxide are identical to those given by Boudart and co-workers (Volpe and Boudart, 1985 a; Volpe and Boudart, 1985 b; Lee et al., 1987, 1988) and McGee et al. (2005) respectively. As will be shown, the transformation of Fe_2O_3 into iron nitride (Fe_2N) can be obtained with the given profile.

Table 2.1: Temperature profile used to transform oxide into nitride

Metal oxide	Fe_2O_3	MoO_3	WO_3
Temperature range I (°C)	25 – 450	25 – 357	25 – 270
Temperature ramp I (°C/min)	3.54	5.53	4.08
Temperature range II (°C)		357 – 467	270 – 560
Temperature ramp II (°C/min)		0.61	0.50
Temperature range III (°C)		467 – 707	
Temperature ramp III (°C/min)		2	
Isothermal phase	450 °C (2 hrs)	707 °C (2 hrs)	560 °C (15 min)

After the isothermal phase, the flow was switched to nitrogen. The cell was then removed from the furnace (once the furnace temperature was about 500 °C) to cool down to room temperature.

2.1.3 Metal carbide catalysts

Once the reactor had reached 25 °C the flow was switched to a CH_4/H_2 mixture (Air products, 20 mol% CH_4) with an upward flow rate of 200 ml(STP)/min. The heating profile is given in Table 2.2. The heating profiles used for the carbidisation of molybdenum and tungsten nitride are from Boudart and co-workers (Volpe and Boudart, 1985 a; Volpe and Boudart, 1985 b; Lee et al., 1987, 1988). It was initially thought that a similar final temperature (700 °C) would result in the transformation of iron nitride into iron carbide.

Table 2.2: Temperature profile used to transform nitride into carbide

Metal nitride	Fe_2N	Mo_2N	W_2N
Temperature range I (°C)	25 – 700	25 – 397	25 – 577
Temperature ramp I (°C/min)	5.63	6.20	4.60
Temperature range II (°C)		397 – 697	577 – 877
Temperature ramp II (°C/min)		1.25	1.43
Isothermal phase	700 °C (3 hrs)		

The cooling was again done in nitrogen by keeping the reactor in the furnace until a temperature of 500 °C was reached, after which it was removed from the furnace to cool down further to room temperature. The product was removed without passivation. The resulting products were black powders which had a metallic lustre.

The carbides were stored in a dessicator with silica gel as drying agent until it was used.

2.2 Characterisation of materials

The materials were characterised by X-ray diffraction (XRD), transmission electron microscopy (TEM) and BET surface area determination. The intermediate nitrides as well as the subsequent carbides were also characterised by XRD, TEM and BET. The temperature-programmed desorption (TPD) of CO was also performed on some of the materials. The spent catalysts were characterised by XRD and TEM.

2.2.1 X-ray diffraction (XRD)

The prepared crystallites were characterised using X-Ray Diffraction analysis to determine the phase purity of the metal oxide precursor, the intermediate metal nitrides, and metal carbides. Application of this method is based on the orderliness of the repeating planes that form a crystallite. When X-rays are directed on the particle, they are diffracted by these ordered planes yielding a pattern unique to a specific plane.

The XRD analyses were performed in a Philips PW3830 diffractometer equipped with a Cu K_α radiation source, using the step scan method. The X-ray diffractometer tube was operated at the following settings:

- Voltage 40kV
- Current 25mA
- 2θ range 20° - 80°
- Step width 0.05 °
- Step duration 1.5 seconds

The observed diffraction peaks were assigned by referring to the Joint Committee on the Powder Diffraction Standards (JCPDS).

The spent catalysts were characterised by XRD to observe any phase changes that might have taken place in the reaction. This however, was not done quantitatively as a different instrument was used for the analysis. The instrument used was a Bruker D8 Advance. The X-ray diffractometer tube was operated at the following settings:

- Voltage 40kV
- Current 40mA
- 2θ range 20° - 80°
- Step width 0.05 °
- Step duration 1.5 seconds

The observed diffraction peaks were assigned by referring to the International Centre for Diffraction Data (ICDD) supplied PDF-2.

The size of the crystallites was also determined using the peak broadening analysis. The application of the Scherrer formula leads to an estimate of the mean crystallite size. The width of an X-ray reflection on the lattice planes of crystallites depends on the characteristics of the crystallites and instrumental factors. The analysis of the diffraction line involves the separation of these factors. The elementary analysis method for the determination of the size of the crystallites gives a rough average size by determining the peak width at half height.

The elementary analysis of the broadening assumes that the lattice deformation of the particles is negligible. Moreover, the instrumental broadening is calculated in a simplified way. Scherrer (1918) showed that the thickness of the crystallite L = N.d_{hkl} in the direction perpendicular to the diffracting planes (hkl) can be obtained from the width β of the diffraction profile using the relationship

$$L = \frac{k\lambda}{\beta_{1/2}\cos\theta_0} = N \cdot d_{hkl} \qquad (1)$$

where

L = crystallite width (Å)

N = number of planes

d_{hkl} = distance between planes (Å)

k = constant (taken as 0.9, since peak width is taken at half peak intensities)

λ = wavelength of X-ray (1.54 Å)

$\beta_{1/2}$ = peak width at half maximum intensity (radians)

θ_0 = angular position of peak maximum

The size of the crystals is therefore inversely proportional to the width of the diffraction line. If both experimental and reference lines exhibit Gaussian profiles the true peak width is given by the Warren formula:

$$\beta_{1/2}^{\ 2} = \beta^2_{Observed} - \beta^2_{Reference} \qquad (2)$$

2.2.2 Transmission electron microscopy (TEM)

Transmission Electron Microscopy is an imaging technique whereby a beam of electrons is focused onto a specimen causing an enlarged version to appear on a fluorescent screen or layer of photographic film. This technique will be used to determine the morphology of the catalyst particles, as well as an estimate of the crystallite size.

The TEM analyses were performed on a LEO Omega 912 Transmission Electron Microscope operating at 120 kV. The finely milled sample was first dispersed in methanol. The fine particles dispersed in methanol were then pipetted out placing it onto a carbon coated copper grid. Images of the samples were then recorded at different magnifications.

The spent catalysts were all characterised by TEM in order to observe any changes in morphology that might have occurred during the Fischer-Tropsch synthesis. Carbonaceous deposits formed during the Fischer-Tropsch synthesis on the catalyst particles can also be determined.

2.2.3 BET surface area

BET analysis was used to determine the surface areas of the prepared samples. In determining this parameter, the catalysts can then be directly compared to other Fischer-Tropsch catalysts in terms of specific activity per unit surface area.

The BET surface area and pore size measurements were done in a Metrometrics Tristar by using N_2-adsorption at 77K. Pre-treatment was done in nitrogen at 90 °C for 60 minutes and then at 350 °C overnight. Pore volumes and the average pore diameter were calculated by Barret-Joyner-Halenda (BJH) method from the desorption isotherm.

2.2.4 Temperature programmed desorption of carbon monoxide (CO-TPD)

TPD experiments start off with the adsorption of a gas or mixture of gases onto a sample. This surface is then heated at a controlled rate. The adsorbates will desorb from the surface. Care must be taken, since chemisorbed species may react during this experiment. The results of the experiment are the rate of desorption of each product species as a function of the temperature.

The desorption behaviour of the materials was investigated by means of temperature programmed desorption of carbon monoxide. The experiment was carried out in a U-type quartz reactor on a Micromeritics AutoChem2910 (Micromeritics Instrument Corp., USA). Catalysts were treated under a carbon monoxide gas flow at a flow rate of 50 ml(NTP)/min.g_{cat} for 2 hrs. This step was the isothermal adsorption at 50 °C. The heating rate of desorption was from 50 to 950 °C at 10 °C/min, and was performed under helium flow.

The instrument was also used for the reduction of a catalyst (iron oxide) as pre-treatment for the Fischer-Tropsch experiment. For this the catalyst samples were exposed to in situ Fischer-Tropsch synthesis pre-treatment conditions i.e., heating under hydrogen at a rate of 10 °C/min to 420 °C holding for 16 hours, at ambient pressure and 1000 ml(NTP)/min.g_{cat} and thereafter desorption in CO flow ramping from 100 to 950 °C.

Carbon monoxide desorption was measured using a thermal conductivity detector which was calibrated at regular intervals using samples with known reduction behaviour (Ag_2O). The samples were heated within a regulated furnace and the temperature was measured by a thermocouple placed 2 mm above the sample.

2.3 Catalyst testing

2.3.1 Experimental set-up

The performance of the carbides in the Fischer-Tropsch synthesis was tested in a Berty reactor. The set-up consisted of three distinct zones, namely the gas feed lines, the reaction section and the product zone. Appropriate CO, H_2 and CO_2 flow rates for Fischer-Tropsch synthesis are set using mass flow controllers. The mass flow controllers used were Brooks Series 5800. The CO and H_2 flow rates are set to obtain a (H_2/CO) molar ratio of 4. The CO_2 was co-fed to the reactor as this is to mimic the feed in the industrial reactor. Argon is added to the feed as an internal standard. The pressure inside the reactor system was controlled and maintained at 20 bar using a back pressure regulator, situated in the product line.

The reactor temperature was controlled using PID control to accurately control the temperature at a specific set point. There were thermocouples situated in the following positions: inside the reactor, between the reactor and heating jacket, on the product line and in the hot knock-out pot. The exit line and the reactor are lagged by glass wool to prevent heat loss.

Heavy products were removed from the product mixture by hot and cold knock-out pots. The hot knock-out pot temperature was controlled by a temperature controller and was set at 200 °C to facilitate the removal of high molecular weight hydrocarbons from the product stream. The cold knock-out pot was maintained at 10 °C, using a cooling bath. This cold knock-out pot was used to remove water and oil fractions from the product stream.

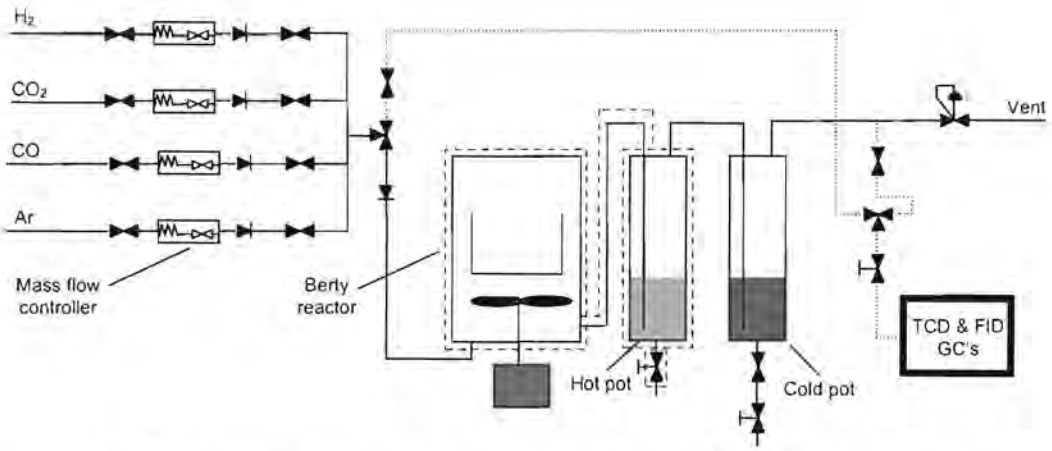

Figure 2.2: Experimental set-up for testing catalyst performance in Fischer-Tropsch synthesis reaction

2.3.2 Catalyst loading

The carbidised materials (Fe-C, Mo-C and W-C) or oxide (Fe-O) (5 g) was loaded into the reactor by dispersing it evenly at the bottom of the reactor basket. A small piece of glass wool was placed loosely on top of the catalyst to allow good mixing of the gases and keep the catalyst in place. The reactor was then closed with a thermocouple positioned so that it measured the temperature inside the catalyst bed. The reactor was sealed tightly. The heating mantle was then placed around the reactor with a thermocouple positioned between the reactor and the heating mantle to measure the temperature at the wall of the reactor.

2.3.3 Catalyst activation

The iron oxide is the only catalyst that was reduced before starting the synthesis. This was done at a temperature of 420 °C and pressure of 20 bar under hydrogen flow. The reduction was done for 16 hours (overnight), after which the temperature was brought down to synthesis temperature (330 °C) under argon flow at 3ml(NTP)/s.

2.3.4 Reaction start-up

The reactor temperature was then taken up to 330 °C under argon flow at 3ml(NTP)/s. The pressure was kept at 20 bar absolute pressure. A pressure test was done to ensure that there were no leaks in the system.

The magnetic drive was then switched on to commence stirring within the reactor. The feed was then introduced to the system. The gas flow rates were set to keep a H_2/CO feed ratio of 4.

The Fischer-Tropsch synthesis was carried out for about 96 hours for the carbidised materials (Fe-C, Mo-C and W-C) and 72 hours for the Fe-O, after which the reactor was shut down. The reactor was then cooled and the catalyst passivated using dry ice.

2.3.5 Product analysis

Inlet and outlet gas samples were taken periodically. The gases were analysed using two on-line HP Agilent 6890 gas chromatographs (GC). CO, H_2, CO_2 and CH_4 were quantified with an on-line GC equipped with a thermal conductivity detector (TCD), while the hydrocarbons were separated on an on-line GC equipped with a flame ionisation detector (FID). Argon was used as an internal standard for the quantification with the GC/TCD. Methane was used as connection between the TCD and FID analysis. Liquid products were collected with a cold trap during the Fischer-Tropsch synthesis and analysed with an off line GC/FID.

Table 2.3: Gas chromatograph and column specifications

	Analysis of permanent gases	**Analysis of organic product compounds**
GC	HP Agilent 6890	HP Agilent 6890
Stationary phase	Restek Shin Carbon	CP Sil 5 CB
Detector	TCD	FID
Carrier gas	Argon	Helium
Column length (m)	2	150
Column diameter (mm)	3	0.25
Column head pressure (bar, abs)	3	1.5
Column temperature (°C)	110	-60 – 250

2.3.6 Data analysis

2.3.6.1 TCD analysis

CO, H_2, CO_2, and $CO+CO_2$ conversion was calculated form the molar flow rates obtained from the GC-TCD analyses. TCD calibration was done by injecting a mixture of H_2, CO, CH_4, Ar and CO_2 of known composition. The response factors were calculated based on Ar from the peak areas and the content of each gas in the calibration mixture.

$$\dot{n}_i = f_i \cdot \frac{A_i}{A_{Ar}} \cdot \dot{n}_{Ar} \qquad (3)$$

with

$$f_i = \frac{x_{i,calib}}{x_{Ar,calib}} \cdot \frac{A_{Ar,calib}}{A_{i,calib}} \qquad (4)$$

as determined from a TCD analysis of the calibration gas mixture with known composition. In the equations, $\dot{n}$ is the molar flow, x is the mole fraction and A is the peak area of a component.

The correlation between the hydrogen and carbon monoxide conversions can give an indication of the extent to which the water-gas shift reaction takes place.

2.3.6.2 FID analysis

The hydrocarbons in the gas phase, as analysed by the on-line GC-FID is calibrated from the molar flow rate of CH_4 obtained from the TCD.

$$\dot{n}_i = \frac{A_i . f}{N_{c,i} . A_{CH_4}} . \dot{n}_{CH_4} \qquad (5)$$

with f the response factor equal to one for hydrocarbons and larger than one for oxygenates. By multiplying the molar flow rates of the hydrocarbons with the molar mass of the individual components, the mass flow rate can be obtained.

$$\dot{m}_{i,gas} = \dot{n}_i . M_i \qquad (6)$$

The mass flow rate of hydrocarbons in the oil phase was obtained as follows:

$$\dot{m}_{i,oil} = \left(\frac{A_i}{\Sigma A_i} \right)_{oil} . \frac{m_{oil}}{time} \qquad (7)$$

with m_{oil} the mass of oil collected over a given time.

The mass flow rate of hydrocarbons in the water phase was obtained using methanol as an internal standard.

$$\dot{m}_{i,water} = \frac{A_i}{A_{CH_3OH}} . \frac{m_{CH_3OH}}{time} \qquad (8)$$

2.3.6.3 Total mass flow rates and mass balance

The total mass flow rate of the hydrocarbons was then obtained by taking the sum of each component as calculated from the different phases.

$$\dot{m}_{i,total} = \dot{m}_{i,gas} + \dot{m}_{i,oil} + \dot{m}_{i,water} \quad (9)$$

This neglects the amount of the fraction in the hot trap, which was minimal. The total mass balance was obtained by the total mass flow of the products and unreacted feed expressed as a percentage of the total feed (excluding Ar) into the reactor.

2.3.6.4 Conversions and selectivity

2.3.6.4.1 CO conversion

The CO conversion (X_{CO}) is defined as the percentage of CO converted into organic products and CO_2 from the CO mass balance. X_{CO} is given by:

$$X_{CO} = \frac{\dot{n}_{CO,in} - \dot{n}_{CO,out}}{\dot{n}_{CO,in}}.100\% \quad (10)$$

2.3.6.4.2 H_2 conversion

The H_2 conversion is the percentage of H_2 converted to hydrocarbons during the Fischer-Tropsch synthesis.

$$X_{H_2} = \frac{\dot{n}_{H_2,in} - \dot{n}_{H_2,out}}{\dot{n}_{H_2,in}}.100\% \quad (11)$$

2.3.6.4.3 CO_2 conversion

The CO_2 conversion is the percentages of CO_2 formed or consumed through the water gas shift forward or reverse reaction. X_{CO2} is defined as:

$$X_{CO_2} = \frac{\dot{n}_{CO_2,in} - \dot{n}_{CO_2,out}}{\dot{n}_{CO_2,in}}.100\% \quad (12)$$

The implication of co-feeding of CO_2 is that the CO_2 conversion can be either positive or negative. CO_2 is normally formed through the water-gas shift reaction, so the conversion of CO_2 is expected to be negative. It can happen that the CO_2 is converted in the reactor, in which case a positive value for the conversion will be obtained. This conversion of CO_2 is thought to go to CO via the reverse water-gas shift reaction.

2.3.6.4.4 $CO+CO_2$ conversion

The $CO+CO_2$ conversion (X_{CO+CO2}) is defined as the amount of CO converted to hydrocarbon products only, as calculated from the $CO+CO_2$ mass balance. X_{CO+CO2} is given by:

$$X_{CO+CO_2} = \frac{\left(\dot{n}_{CO,in} + \dot{n}_{CO_2,in}\right) - \left(\dot{n}_{CO,out} + \dot{n}_{CO_2,out}\right)}{\left(\dot{n}_{CO,in} + \dot{n}_{CO_2,in}\right)} .100 \qquad (13)$$

The $CO+CO_2$ conversion gives the extent of CO conversion to hydrocarbons. In the case of CO_2 being converted, this will then add to the formation of hydrocarbons. This is assumed to take place by CO_2 forming CO through the reverse water-gas shift reaction, which is then converted to hydrocarbons.

2.3.6.4.5 Product selectivity

Methane selectivity (S_{CH4}) is the percentage of product that goes to methane per total hydrocarbon product, excluding CO_2 formation.

$$S_{CH_4} = \frac{\left(\dot{n}_{CH_4,out} - \dot{n}_{CH_4,in}\right)}{\left(\dot{n}_{CO,in} + \dot{n}_{CO_2,in}\right) - \left(\dot{n}_{CO,out} + \dot{n}_{CO_2,out}\right)} .100\% \qquad (14)$$

This expression is used to calculate the percentage of carbon atom selectivity of all the hydrocarbon product components. Selectivity is expressed as carbon percent, since this value is of industrial interest.

2.3.6.5 Selectivity parameters

2.3.6.5.1 Olefin content

The olefin content in the product was expressed as a percentage of the total sum of olefins with carbon number N per total sum of hydrocarbon products with carbon number N.

$$S_{Olefin,N} = \frac{\left(\Sigma \dot{n}_{ol,N}\right)}{\left(\Sigma \dot{n}_{HC,N}\right)} \cdot 100\% \qquad (15)$$

2.3.6.5.2 1-Olefin content

1-olefin content in the olefinic product with carbon number N was expressed as a percentage of the total linear olefin product with carbon number N:

$$S_{1-Olefin,N} = \frac{\Sigma\left(\dot{n}_{1-ol,N}\right)}{\Sigma\left(\dot{n}_{n-ol,N}\right)} \cdot 100\% \qquad (16)$$

2.3.6.5.3 Oxygenate content

The oxygenate content per carbon number fraction was expressed as a percentage of the total hydrocarbon (including oxygenate) product of that carbon number:

$$S_{OxygenateN} = \frac{\Sigma \dot{n}_{ox,N}}{\Sigma \dot{n}_{HC+ox,N}} \cdot 100\% \qquad (17)$$

2.3.6.5.4 Branched products

The branched products in the hydrocarbon product were expressed as a fraction of the total linear hydrocarbon product:

$$S_{Branched,N} = \frac{\dot{\Sigma} n_{branch,N}}{\dot{\Sigma} n_{LHC,N}} \cdot 100\% \qquad (18)$$

3. Results

3.1 Catalyst characterisation

3.1.1 X-ray diffraction (XRD)

3.1.1.1 Oxide precursors

XRD experiments were carried out to determine the phase purity of the prepared species and to estimate the average crystallite size within the samples. The prepared sample is defined to be pure if all the peaks in the XRD spectrum are attributable to a single phase. Additional peaks indicate the presence of another phase in the sample. The reference patterns are given in the appendix.

Figure 3.1 shows the XRD spectrum of the iron oxide precursor prepared by precipitation. The XRD spectrum indicates that the prepared sample is pure hematite (Fe_2O_3). From the preparation technique used, this is the phase that could be expected. The XRD pattern of iron oxide shows the most intense peaks at 33.3°, 35.7° and 54.2° characteristic of the hematite phase.

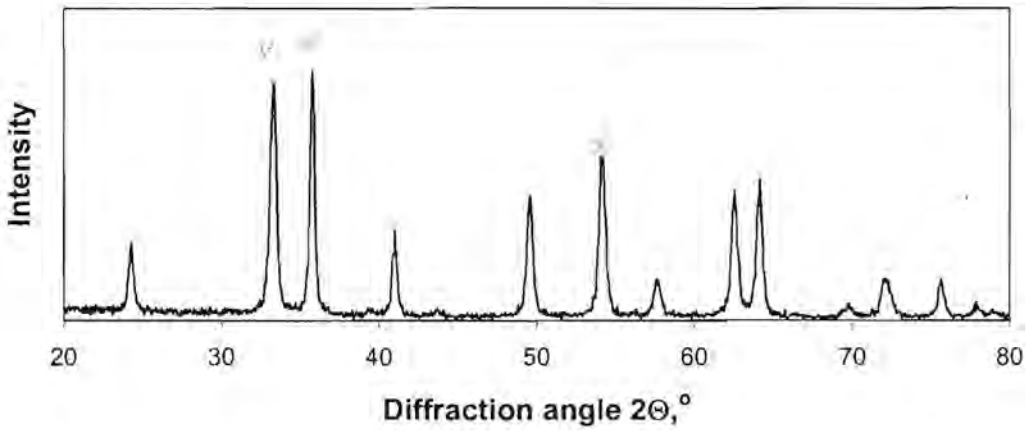

Figure 3.1: XRD pattern of iron oxide

The average crystallite size was estimated by line broadening analysis, using the Scherrer equation (β estimated from the width at half height of the peaks). There is an error in the crystallite size determination, which comes from the measurement of the width of the peak. The crystallite size of the hematite crystallites therefore appears to be 40 nm, as indicated in Table 3.1.

Table 3.1: Crystallite sizes of Fe_2O_3 as determined by XRD-line broadening

Diffraction angle 2Θ,°	$d_{crystal}$, nm
33.3	36±4
35.7	43±5
49.6	38±4
54.2	36±3
62.6	40±4
64.2	44±5

The XRD pattern of molybdenum oxide, prepared by calcination of ammonium molybdate, is shown in Figure 3.2. The phase appears to be pure, since all the peaks are attributable to MoO_3. The spectrum has its major peaks at 23.4°, 25.7° and 27.3°. These peaks can be attributed to the presence of MoO_3.

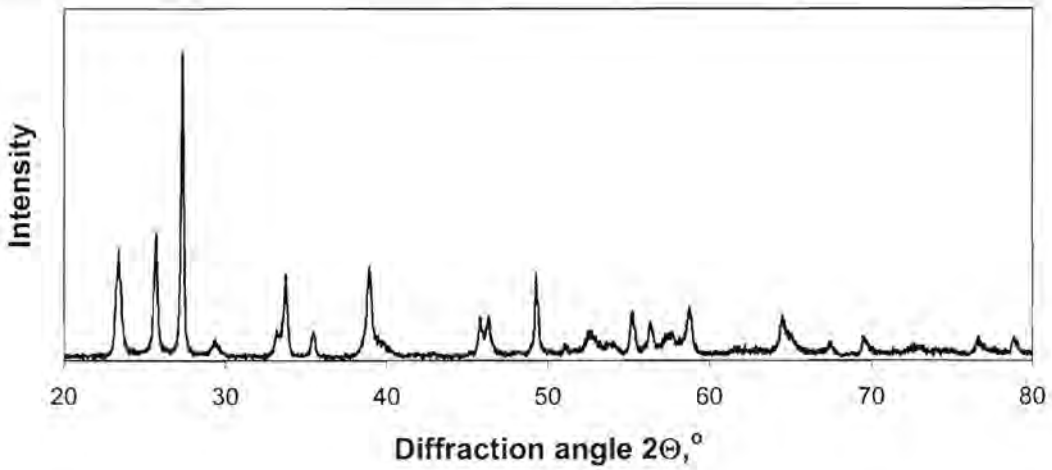

Figure 3.2: XRD pattern of molybdenum oxide

The crystallite diameters measured seem to have two main sizes, since there are peaks that are around 50 nm and others that are about 60 nm, possibly due to preferential crystal growth. However, the difference between the sizes is small enough, taking into account the error in measurement, to approximate the crystallite diameter to about 52 nm from the measured peaks.

Table 3.2: Crystallite sizes of MoO_3 as determined by XRD-line broadening

Diffraction angle 2Θ,°	$d_{crystal}$, nm
23.4	49±6
25.7	53±10
27.3	63±16
33.7	48±7
38.9	48±6
49.3	56±9

Tungsten oxide was obtained by calcining commercial tungsten oxide at 330 °C. It can be seen from the XRD pattern of tungsten oxide, that the phase present is WO_3, since the peaks occurring at 23.1°, 23.6° and 24.3° represent this phase of tungsten oxide. All the peaks are attributable to this phase, indicating that it is the only phase present in the sample.

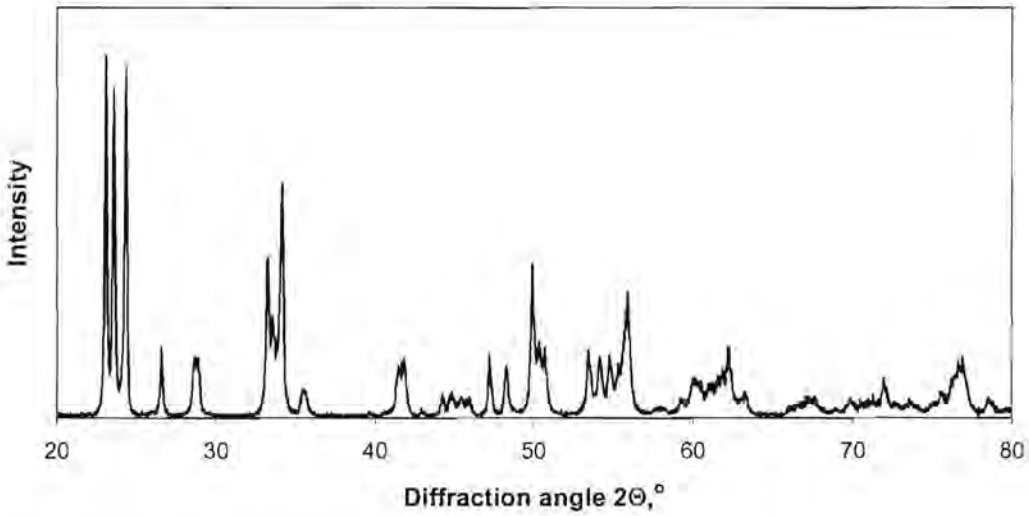

Figure 3.3: XRD pattern of tungsten oxide

The crystallites measure about 60 nm and 70 nm from calculations based on the major peaks. Since there is an error in the crystallite size estimation, the crystallites seem to be roughly spherical with a diameter of about 62 nm.

Table 3.3: Crystallite sizes of WO_3 as determined by XRD-line broadening

Diffraction angle 2Θ,°	$d_{crystal}$, nm
23.1	67±18
23.6	71±24
24.3	67±18
33.2	56±10
34.1	56±10
49.9	56±9

3.1.1.2 Nitride intermediates

The iron nitride was obtained by temperature programmed nitridation of the iron oxide precursor using NH_3. The XRD pattern of iron nitride, shown in Figure 3.4, shows major peaks at 40.8°, 42.9° and 56.6°, which indicates that

the phase of iron nitride present is Fe_2N. Since all the peaks can be attributed to Fe_2N, it can be said that the nitridation was complete and that the sample is phase pure.

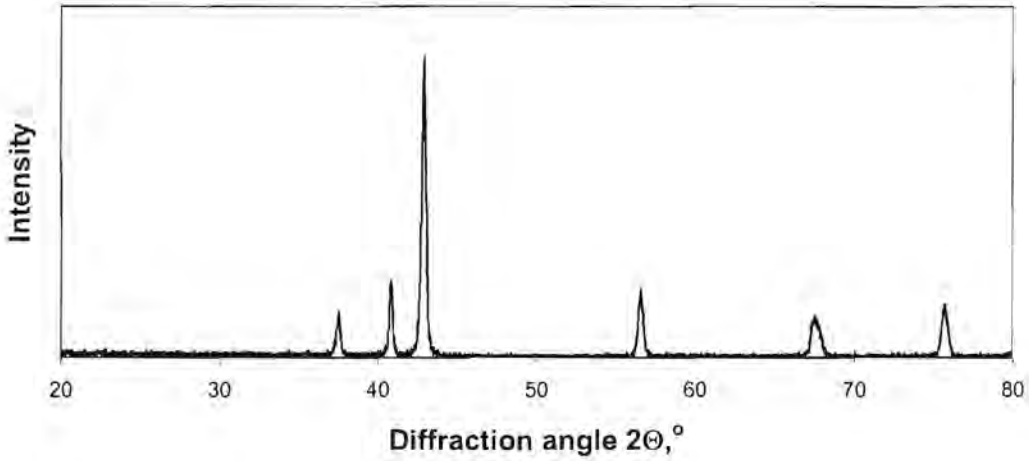

Figure 3.4: XRD pattern of iron nitride

The crystallite sizes (see Table 3.4) represented by all the peaks are roughly 48 nm, with the particles approximately spherical.

Table 3.4: Crystallite sizes of Fe_2N as determined by XRD-line broadening

Diffraction angle 2Θ,°	$d_{crystal}$, nm
37.5	53±9
40.8	54±9
42.9	44±6
56.6	49±7
67.6	38±3
75.7	43±4

Figure 3.5 shows the XRD spectrum of molybdenum nitride. The peaks that can be seen at 37.2°, 43.2°, 62.6° and 75.2° in Figure 3.5 indicate the presence of Mo_2N. The peaks are all attributable to this phase, indicating that the nitridation of the oxide was complete.

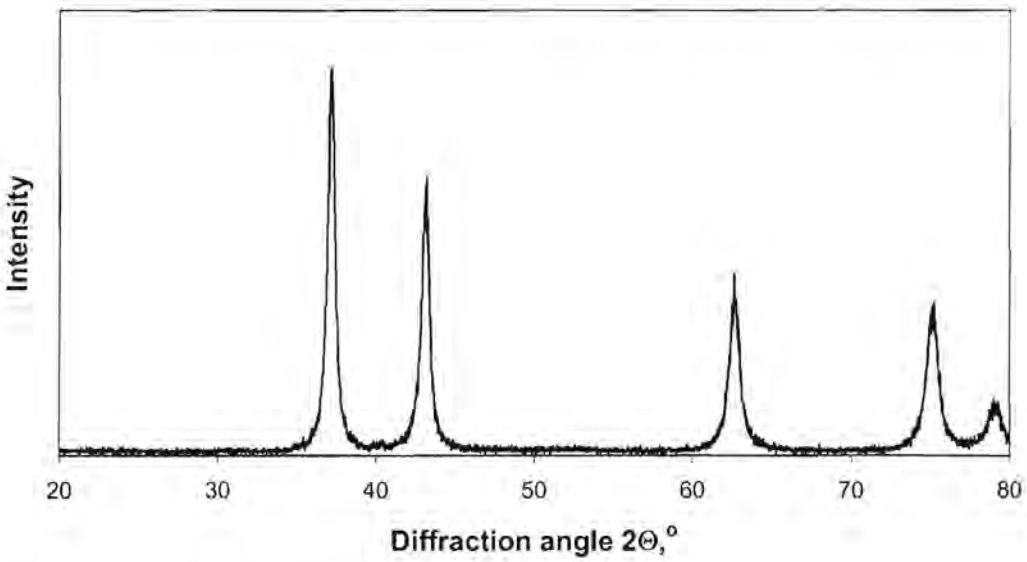

Figure 3.5: XRD pattern of molybdenum nitride

The crystallite size varies between 20 nm and 30 nm (see Table 3.5). It can therefore be said that the crystallites are roughly spherical with a diameter of about 24 nm.

Table 3.5: Crystallite sizes of Mo_2N as determined by XRD-line broadening

Diffraction angle 2Θ,°	$d_{crystal}$, nm
37.2	29±2
43.2	27±2
62.6	25±2
75.2	21±1
79.1	20±1

Figure 3.6 shows the XRD spectrum of tungsten nitride. The XRD pattern shows that the tungsten nitride is present in the β-W_2N phase.

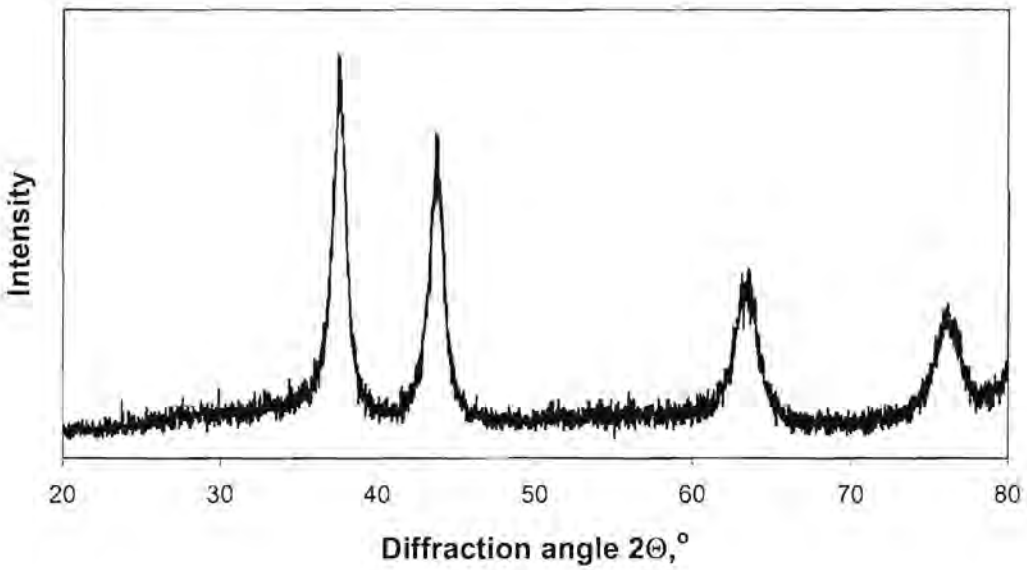

Figure 3.6: XRD pattern of tungsten nitride

The tungsten nitride crystallites are spherical particles with an average diameter of about 16 nm, and with the crystallite diameters ranging from 14 nm to 17 nm.

Table 3.6: Crystallite sizes of W_2N as determined by XRD-line broadening

Diffraction angle 2Θ, °	$d_{crystal}$, nm
37.5	17±1
43.8	16±1
63.4	14±1

3.1.1.3 Carbide catalysts

The carbide catalysts were obtained by the temperature programmed reaction of the nitride intermediates with a CH_4/H_2 mixture. The XRD pattern of iron nitride exposed to this procedure is shown in Figure 3.7. It shows peaks characteristic of synthetic cohenite (cementite), Fe_3C at a 2θ value of 42.9° and 43.7°. The larger peaks occurring at 44.7° and 65.0° indicate that metallic

iron is the most abundant phase in the sample. The observed phases indicate that the temperature at which this carbidisation was carried out was too high.

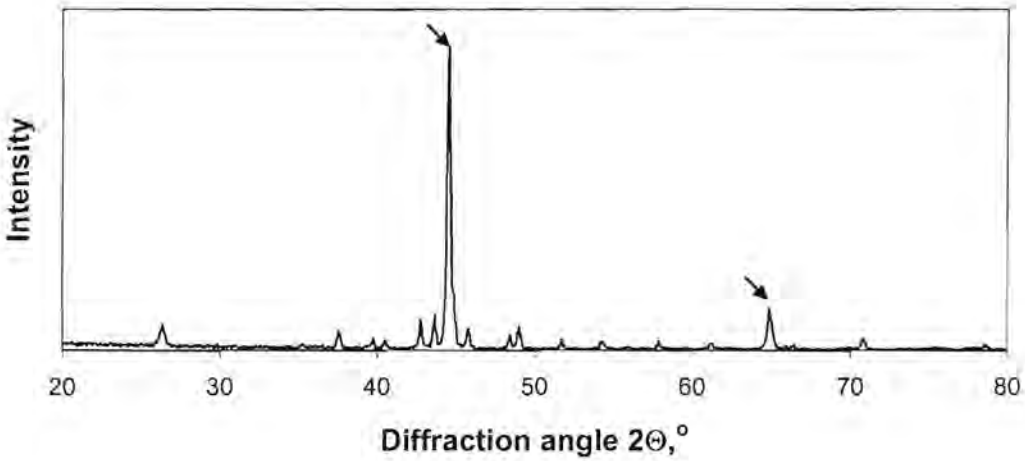

Figure 3.7: XRD pattern of (metallic iron ↘)/iron carbide mixture

The Fe crystallite size as calculated from the Fe peaks on the XRD spectrum of iron carbide/metallic iron is about 52 nm. The crystallite sizes estimated from the line broadening analysis on the Fe_3C peaks shows that these particles are larger than the Fe particles. These crystallites are calculated to about 66 nm.

Table 3.7: Crystallite sizes of Fe_3C as determined by XRD-line broadening

Diffraction angle 2Θ,°	$d_{crystal}$, nm
42.8	69±17
43.7	69±17
45.8	59±11
44.5 (Fe)	55±9
64.9 (Fe)	49±6

Figure 3.8 shows the XRD spectrum of molybdenum carbide. It can be seen from Figure 3.8 that the phase of molybdenum carbide present is Mo_2C. The most intense peak at 39.4° is characteristic of this phase. The peaks at 36.2,

42.5, 48.4, (61.4 overlapping), 73.7 and 77.9 are not attributable to this phase. These peaks seem to be due α-MoC_{1-x} phases.

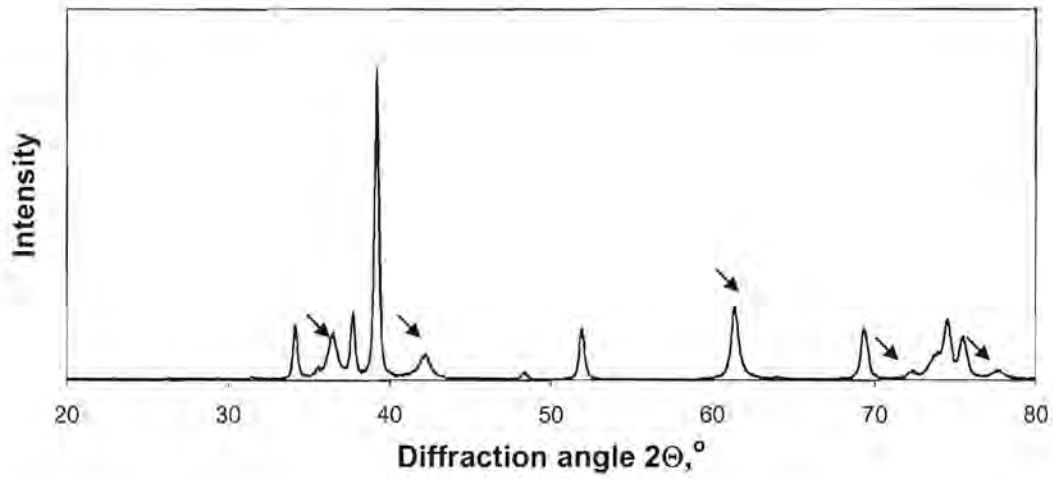

Figure 3.8: XRD pattern of molybdenum carbides (Mo_2C/α-MoC_{1-x} ↘)

The crystallite size is about 43 nm as calculated from the major peaks of the Mo_2C phase.

Table 3.8: Crystallite sizes of Mo_2C as determined by XRD-line broadening

Diffraction angle 2Θ,°	$d_{crystal}$, nm
34.1	48±7
39.2	48±7
61.4	39±3
69.4	38±3

Figure 3.9 shows the XRD spectrum of tungsten carbide. The XRD pattern of the tungsten carbide shows that the phase present is WC. The peaks assigned to tungsten nitride are not visible in the spectrum, suggesting that the nitride intermediate was completely transformed.

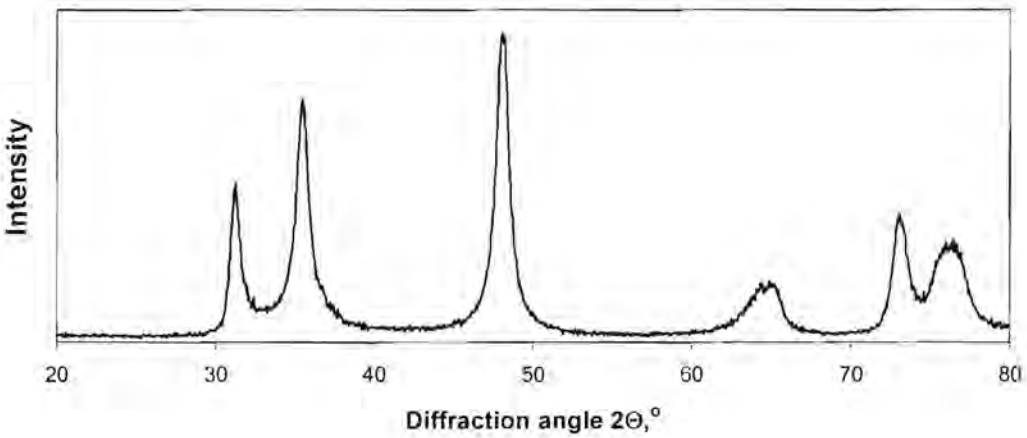

Figure 3.9: XRD pattern of tungsten carbide

The crystallite size for this species is found to be about of 22 nm as estimated from the peaks indicated in Table 3.9.

Table 3.9: Crystallite sizes of WC as determined by XRD-line broadening

Diffraction angle 2Θ,°	$d_{crystal}$, nm)
31.2	25±2
35.5	20±1
48.2	20±1

3.1.2 BET surface area

BET analysis was carried out to establish the surface area of the prepared species. From the measured surface areas, the crystallite size can be determined, assuming the particles to be spherical.

Table 3.10: BET surface area, volume and pore size of species

Species	Surface area (m^2/g)	Pore volume (cm^3/g)	Average pore diameter (Å)	Crystallite size (nm)
Iron oxide	30	0.120	158	38
Iron nitride	6	0.019	140	157
Metallic iron/ Iron carbide	1	0.005	192	794
Molybdenum oxide	7	0.054	314	186
Molybdenum nitride	10	0.061	247	-
Molybdenum carbides	14	0.045	129	49
Tungsten oxide	3	0.022	296	286
Tungsten nitride	20	0.042	83	-
Tungsten carbide	18	0.083	181	21

The surface area of the iron species shows a significant decrease upon transformation from the oxide to the nitride and an even further decrease in the carbidisation. The pore volume seems to follow the same trend as the surface area. The pore volume decreases with nitridation, and then decreases further when the nitride is transformed into the carbide.

The molybdenum species shows a slight increase in surface area as it transforms from the oxide, through to the carbide. The pore volume also increases between the oxide and the nitride, but then decreases to the carbide. The average pore diameter decreases as the molybdenum species is transformed to the nitride, and then decreases further on carbidisation.

Tungsten oxide has a low surface area, which increases significantly as it transforms to the nitride. The carbidisation does not seem to alter this surface area. The pore volume increases with decreasing oxidation number of the tungsten species. The pore diameter shows a marked decrease on nitridation and then an increase when it is transformed to the carbide.

The crystallite diameters calculated for the iron species show a gradual increase with transformation. The nitride and carbide species are likely to have agglomerated particles present, due to some degree of sintering. The molybdenum and tungsten oxides have rather low surface areas and therefore large calculated crystallite diameters. These measurements were repeated and found to have surface areas within 1 m^2/g of the reported values. These low surface areas of molybdenum and tungsten oxide were also reported by Patterson et al. (2003).

3.1.3 Transmission electron microscopy (TEM)

TEM photographs were taken of the prepared species. The TEM images of the various species show that there is a change in the morphology of the crystallites upon transformation. The oxides appear almost spherical. The nitrides are slightly more angular, but are still present as free particles. In the case of the carbides the crystallites are grouped together and form larger sintered or needle-like structures.

The single particles were in each case measured. The degree to which the samples were dispersed was not very extensive, so therefore only five single crystal diameters were measured. The sizes are therefore only included to give an indication of the particle size. In the case of the carbides, the needle thickness or distance between cracks of edges were measured instead of the crystallite diameter.

The iron oxide crystallites in the Figure 3.10 seem to be spherical particles with a diameter of 36 – 44 nm, with an average of about 40 nm. The larger dark particles are caused by crystallites that are superimposed on each other due to incomplete dispersion of the particles in the methanol when the sample was prepared for this analysis.

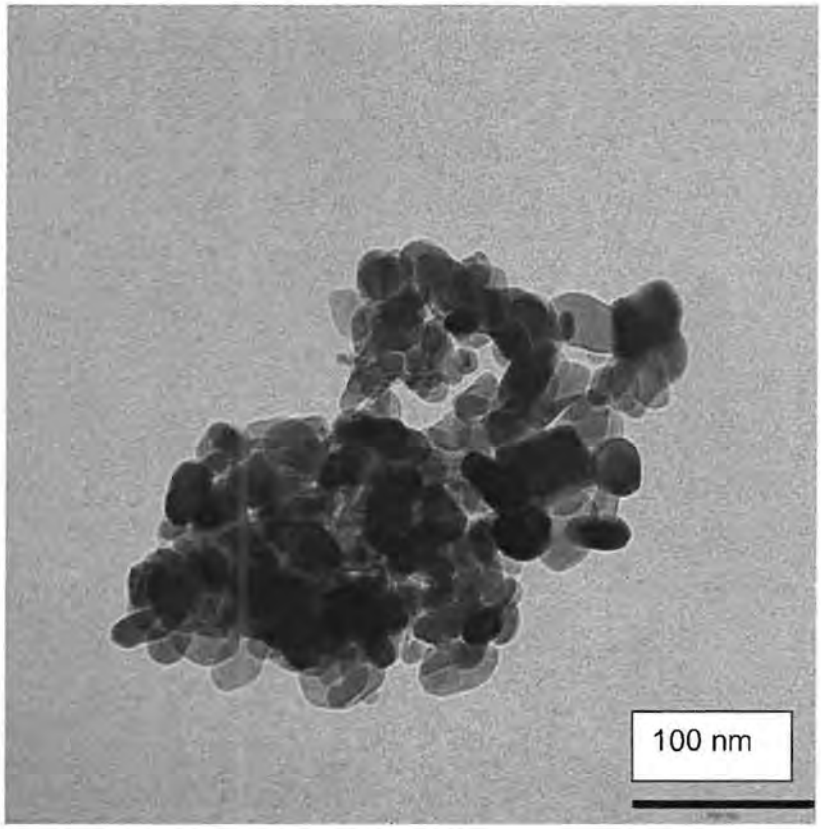

Figure 3.10: TEM image of iron oxide

It can be seen from Figure 3.11 that the crystallites of MoO_3 are mostly grouped in large clusters. There are a few single crystals visible. These crystals seem to be almost spherical, with sizes between 51 nm and 60 nm and an average crystallite diameter of 56 nm.

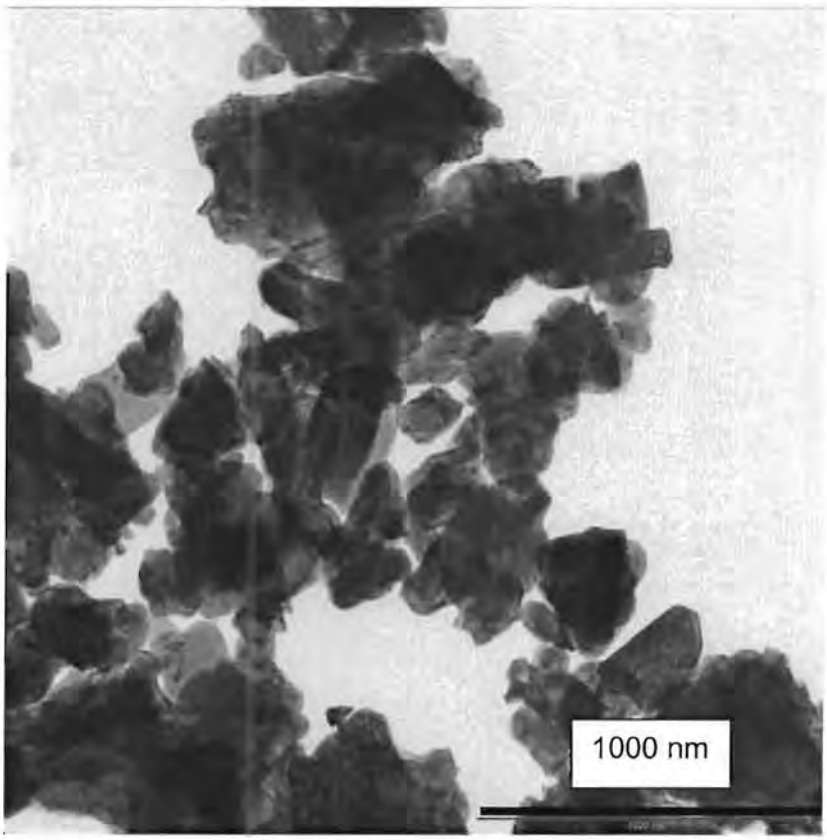

Figure 3.11: TEM image of molybdenum oxide

The WO_3 crystallites that can be seen from Figure 3.12, the TEM photograph of tungsten oxide, are spherical. The single crystals seem to be about 59 - 69 nm in diameter, with an average of 65 nm, although there are smaller particles present.

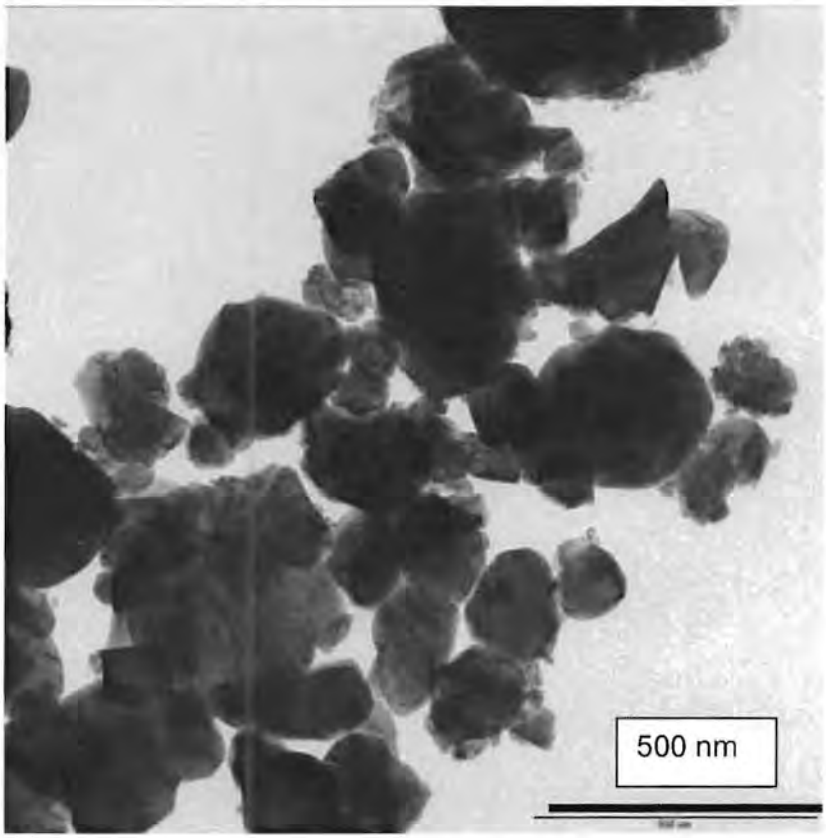

Figure 3.12: TEM image of tungsten oxide

The particles of the iron nitride intermediate shown in Figure 3.13 are largely superimposed, making it difficult to distinguish single crystals. There are crystallites visible that appear to be about 50 nm in diameter. The measured particles were found to have sizes between 47 nm and 57 nm.

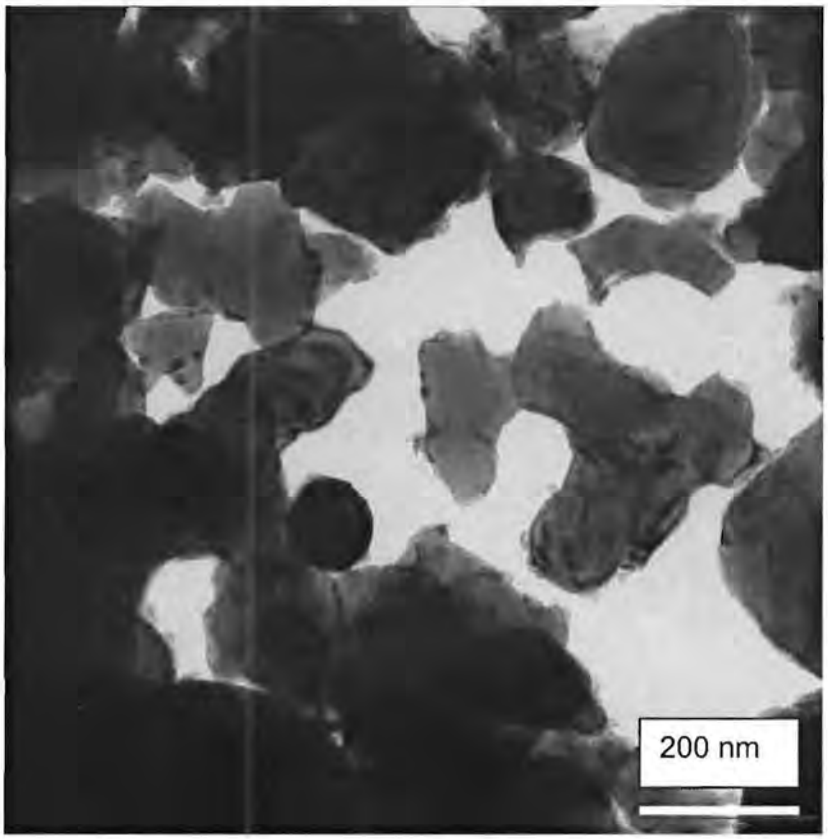

Figure 3.13: TEM image of iron nitride

The molybdenum nitride crystallites, shown in Figure 3.14, can be seen clearly even though they are mostly grouped together. The crystallites all seem to be spherical particles with a diameter of about 31 nm. The sizes of the crystallites measured range from 29 nm to 33 nm.

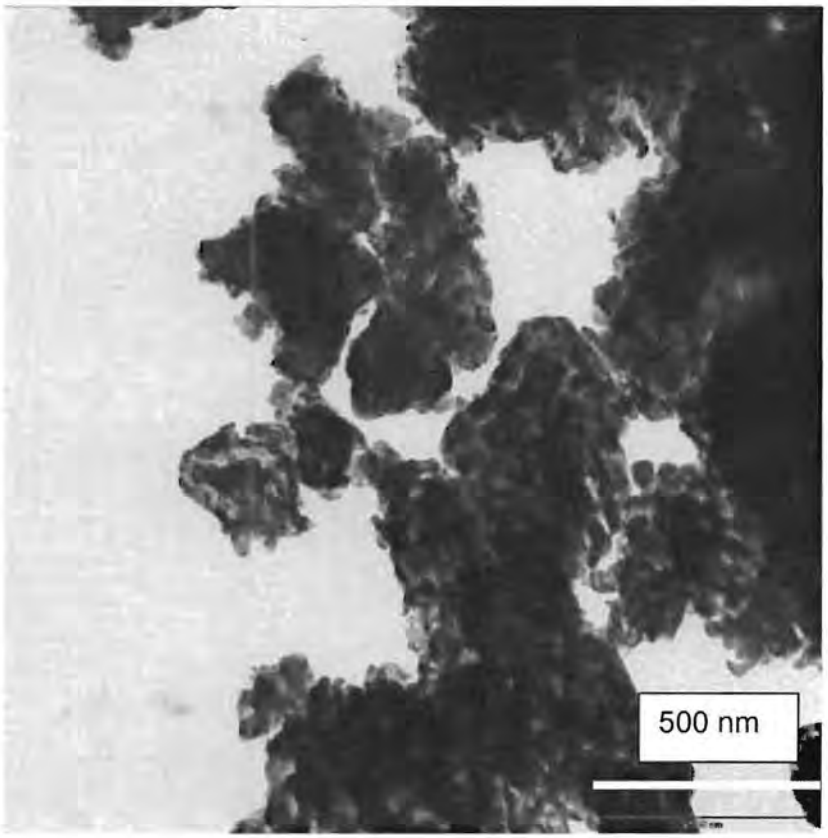

Figure 3.14: TEM image of molybdenum nitride

In the image of the tungsten nitride crystallites, Figure 3.15, it can be seen that the particles are essentially spherical. The single crystals appear to be, on average, 21 nm in diameter. The bulk of the particles however, are superimposed on each other. The measured single crystals range from 19 nm to 23 nm.

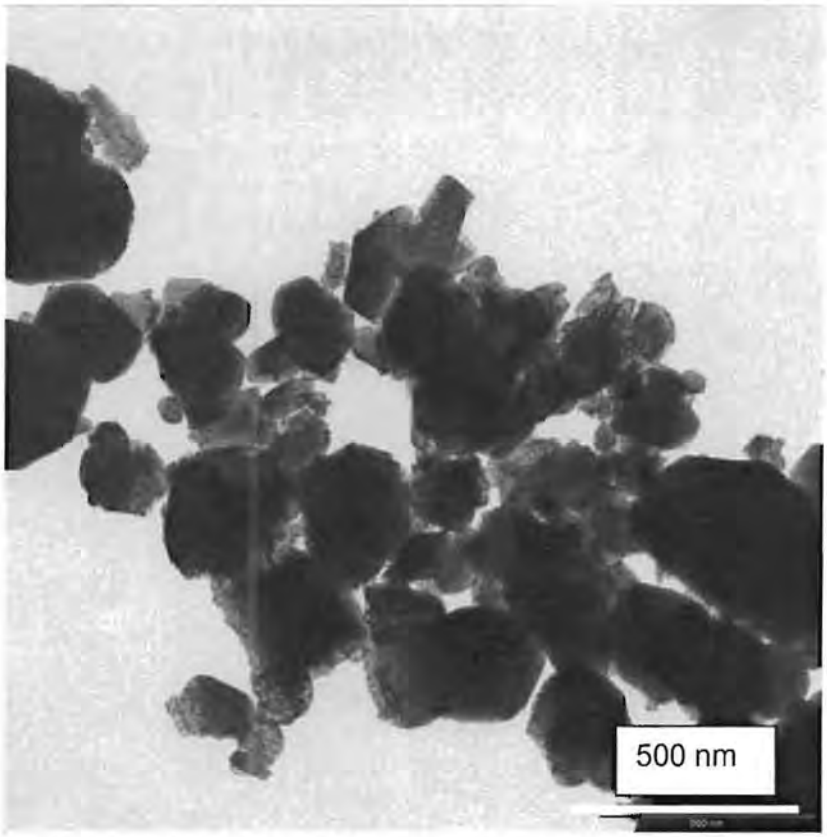

Figure 3.15: TEM image of tungsten nitride

Iron carbide/metallic iron, as seen in Figure 3.16, seems to be different from the iron oxide and nitride precursors. Some particles appear to be needle-shaped, with some of the needles being about 100 nm in length. Along the length, there appears to be flaws or cracks in the crystallite, which range from 47 nm to 54 nm and are on average 51 nm apart. The rest of the particles appear sintered, but also with similar flaws as seen on the needles.

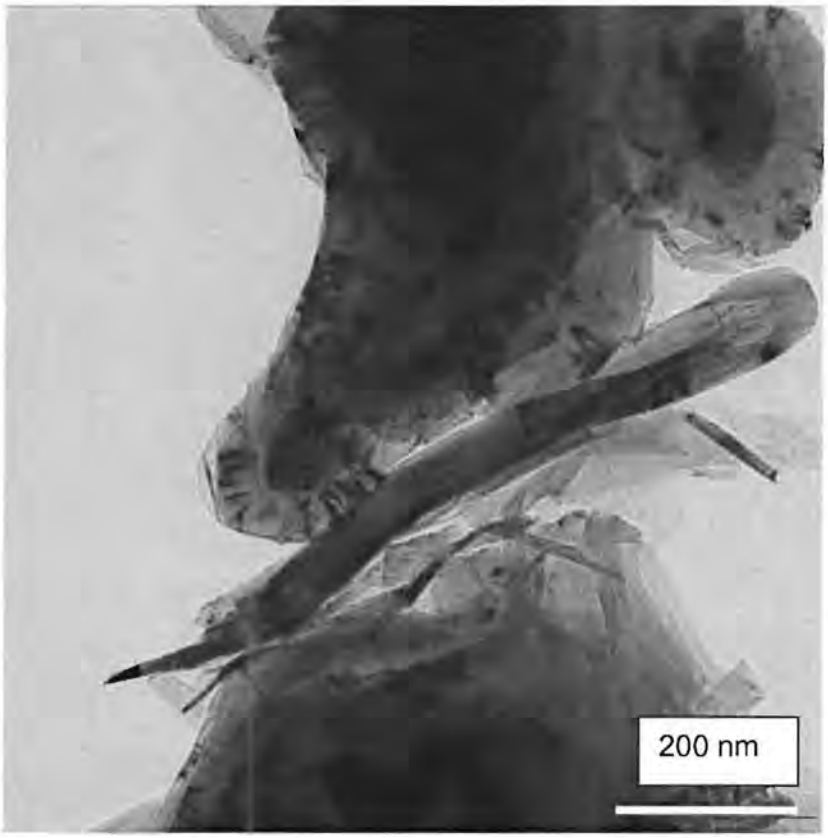

Figure 3.16: TEM image of iron carbide/metallic iron

It can be seen in Figure 3.17, that the molybdenum carbide crystallites are agglomerated as needle-like structures. The needles seem to be made up of crystallites that are less than 20 nm in size. The width of the needles range from 36 nm to 53 nm, and is on average 44 nm. The length of the needles is between 400 nm and 800 nm.

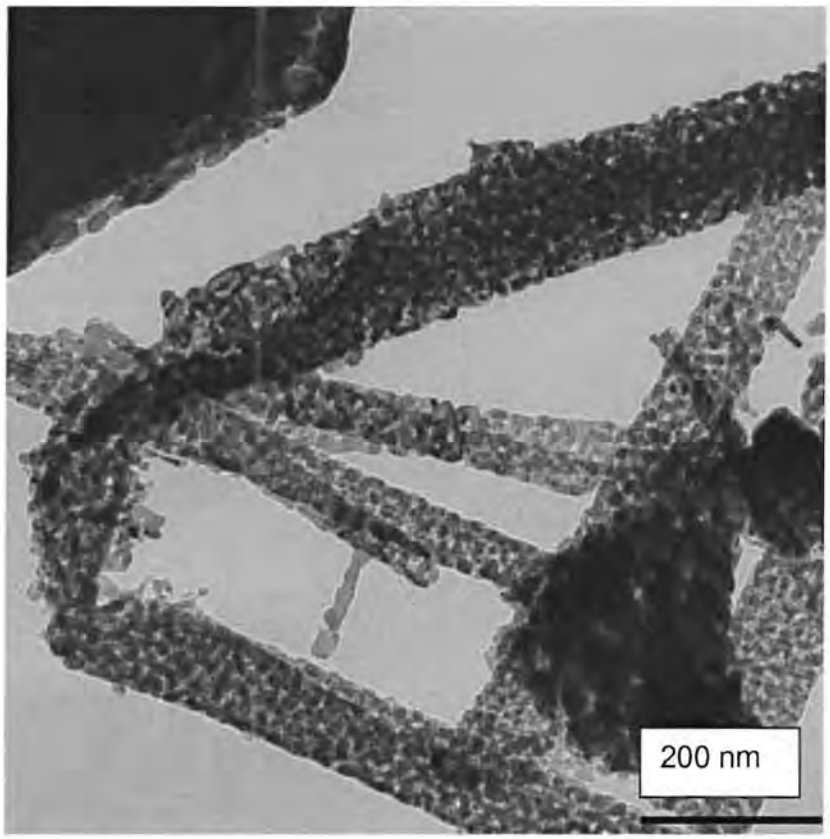

Figure 3.17: TEM image of molybdenum carbides ($Mo_2C/\alpha\text{-}MoC_{1-x}$)

It can be seen in Figure 3.18 that the crystallites of the tungsten carbide have two main shapes. The bulk of the crystallites are spherical, with a diameter ranging from 18 nm to 24 nm (average 21 nm). There are also some needle-shaped crystallites present, with a width of smaller than 50 nm and a length of up to 400 nm.

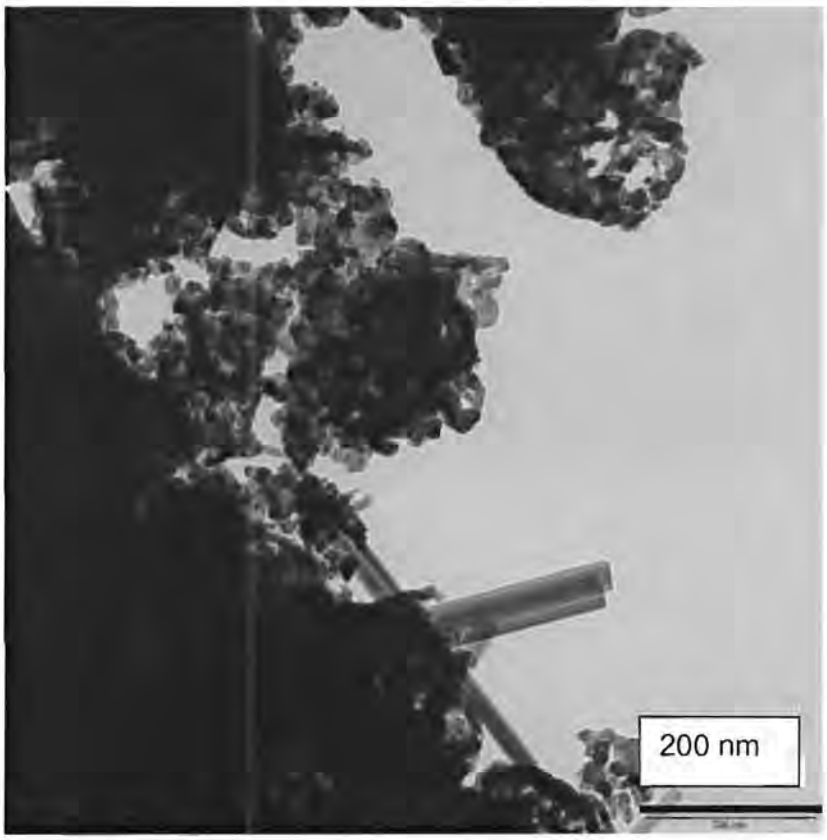

Figure 3.18: TEM image of tungsten carbide

3.1.4 Temperature programmed desorption of carbon monoxide (CO-TPD)

Temperature programmed desorption of carbon monoxide was carried out over the reduced oxide and carbidised iron species. The desorption temperature and the shape of the desorption peak are all analysed to provide information about the binding character of the adsorbate/substrate system.

Figure 3.19 shows the CO-TPD profile for reduced iron oxide. It can be seen that the major desorption peak occurs at about 400 °C, with smaller, broad peaks between 100 °C and 250 °C. The major peak is also not very sharp, as desorption appears to take place over a broad temperature range.

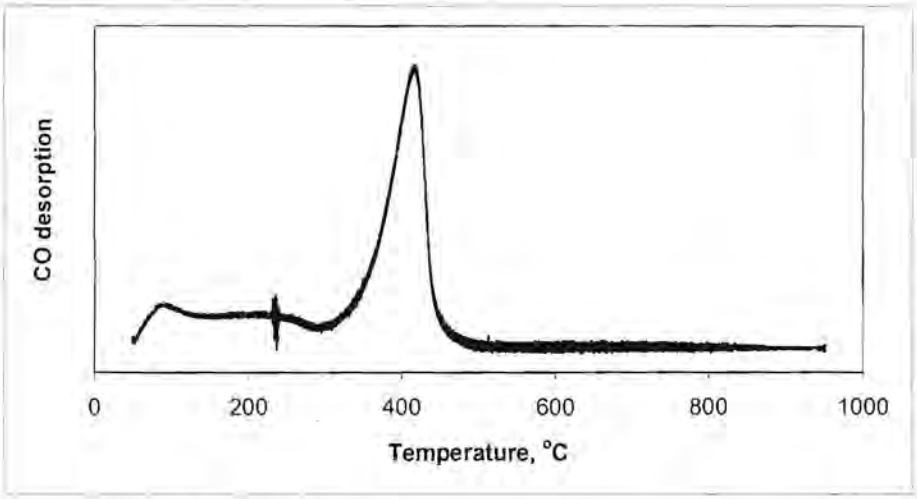

Figure 3.19: CO-TPD profile for reduced iron oxide (reduced at 420 °C for 16 hrs)

Figure 3.20 shows the CO-TPD profile of iron carbide/metallic iron. It can be seen that the major peak is at a very high temperature (950 °C). This peak is not due to CO desorption. There seems to be a desorption peak at about 150 °C. This peak is also rather broad.

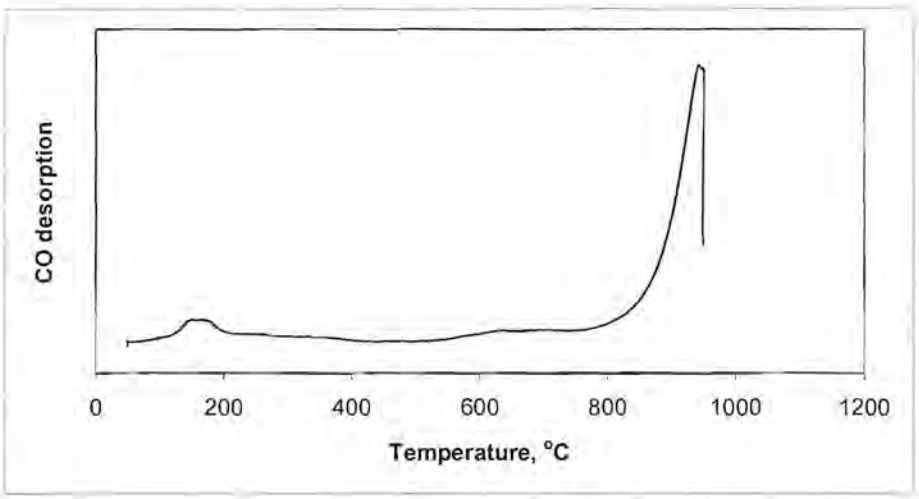

Figure 3.20: CO-TPD profile of metallic iron/iron carbide

A comparison of the two TPD profiles indicate that similar desorption behaviour occurs over the two iron-based materials.

3.2 Catalyst testing

The catalytic performance of the prepared carbidised materials as well as the iron oxide was tested under Fischer-Tropsch conditions in a Berty reactor. The catalyst naming is indicated in Table 3.11. Performance characterisation was based on activity and selectivity data obtained from reactions. Catalyst activity was reflected by the amount of $CO+CO_2$ converted under test conditions.

Table 3.11: Catalyst naming

Catalyst name	Material composition
Fe-O	Fe_2O_3
Fe-C	Fe/Fe_3C
Mo-C	$Mo_2C/\alpha\text{-}MoC_{1-x}$
W-C	WC

3.2.1 Fe-O

The testing of Fe-O was done as the base case. For these reactions, two precipitated iron oxide catalysts prepared at different places (Fe-O I at the University of Cape Town and Fe-O II at Sasol Technology) and different apparatus and chemicals were used. The drying temperature of Fe-O II was also slightly higher (150 °C) than that used for Fe-O I. The mass of unreacted feed and products was about 92% of the mass of reactants fed for both catalysts.

For the Fe-O I catalyst, the H_2 conversion starts off at 34% for the first two periods of synthesis and after three days on line it is at 43%. The CO conversion is stable at about 80% for all of the periods as indicated in Figure

for the three periods. The CO conversion is stable at about 86% throughout the run. This shows reasonable reproducibility for the activity of these two oxide-derived iron catalysts.

This conversion over the Fe-O catalysts is higher than that obtained by Herranz et al. (2006) employing a catalyst prepared in the same way at slightly different conditions. These authors obtained a CO conversion of 23% on a catalyst with the operating temperature at 300 °C. The different conversion can therefore be expected.

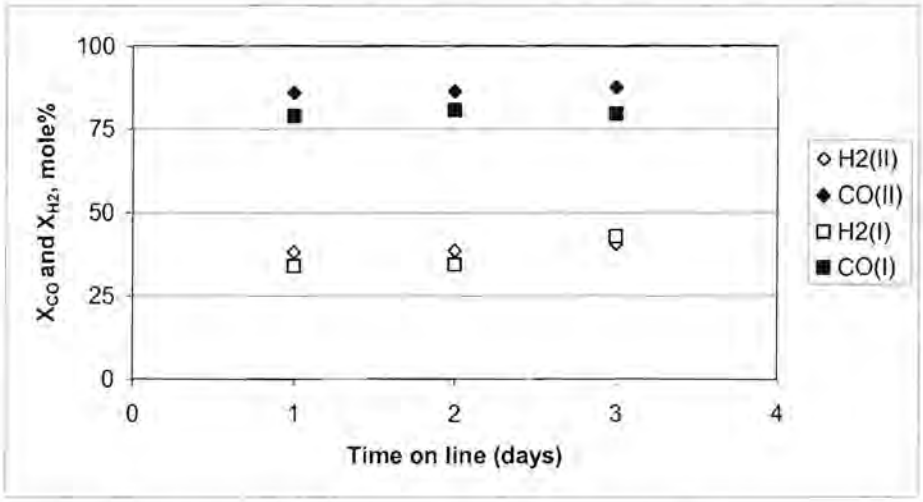

Figure 3.21: H_2 and CO conversion graph over Fe-O

It can be seen in Figure 3.22 that the $CO+CO_2$ conversion over the Fe-O I catalyst is about 40%. This is because the water-gas shift reaction is consuming some (10%) of the CO that is being converted. The same can be seen for the Fe-O II catalyst. The $CO+CO_2$ conversion over the Fe-O II catalyst is about 44%. This is very similar to the $CO+CO_2$ conversion observed over the Fe-O I catalyst.

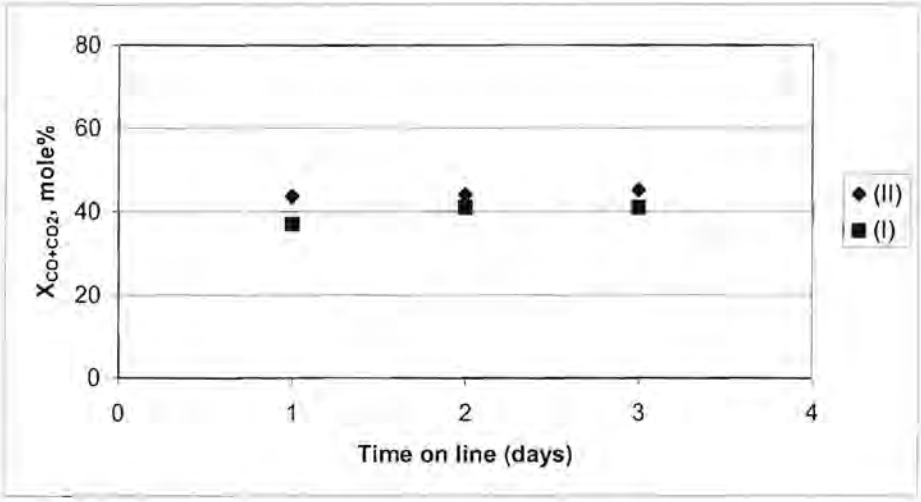

Figure 3.22: $CO+CO_2$ conversion graph over Fe-O

Figure 3.23 shows that CO_2 is being formed over the Fe-O I catalyst. It can be seen that the amount of CO_2 formed is about 10% of the CO_2 that was fed to the reaction. The CO_2 conversion is very similar for the Fe-O II catalyst, therefore also showing that the water-gas shift reaction is taking place over the catalysts.

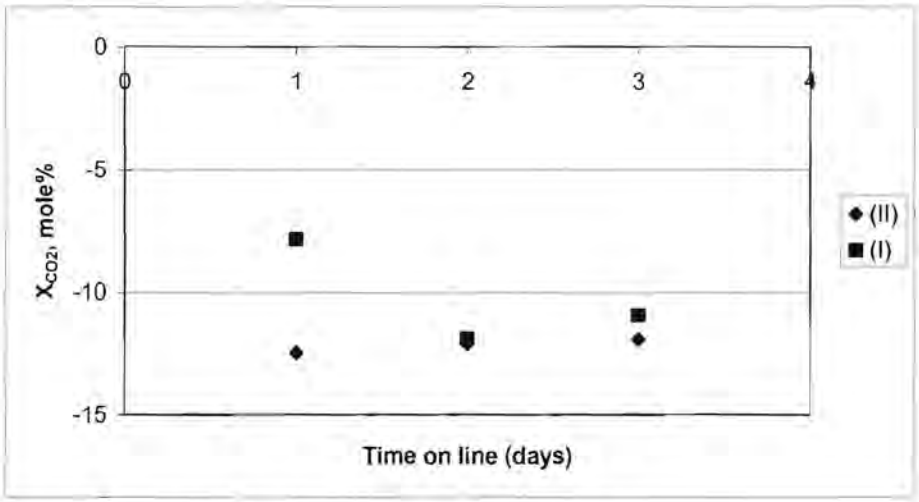

Figure 3.23: CO_2 conversion graph over Fe-O

The methane selectivity over the Fe-O I catalyst is about 11% (see Figure 3.24). There is a definite increase in methane selectivity over the three periods as indicated on the graph. Figure 3.24 also shows that the methane selectivity over Fe-O II is higher than that obtained over the Fe-O I catalyst,

since the value is around 20%. The difference in the methane selectivity is in part attributable to an error in determination from measurement. The difference in preparation conditions of the two catalysts could also justify differences.

Herranz et al. (2006) reported similar methane selectivity (19%) over their Fe catalyst as on the Fe-O II. Their catalyst was prepared in a similar way. The activation of their catalyst was, however, performed at atmospheric pressure.

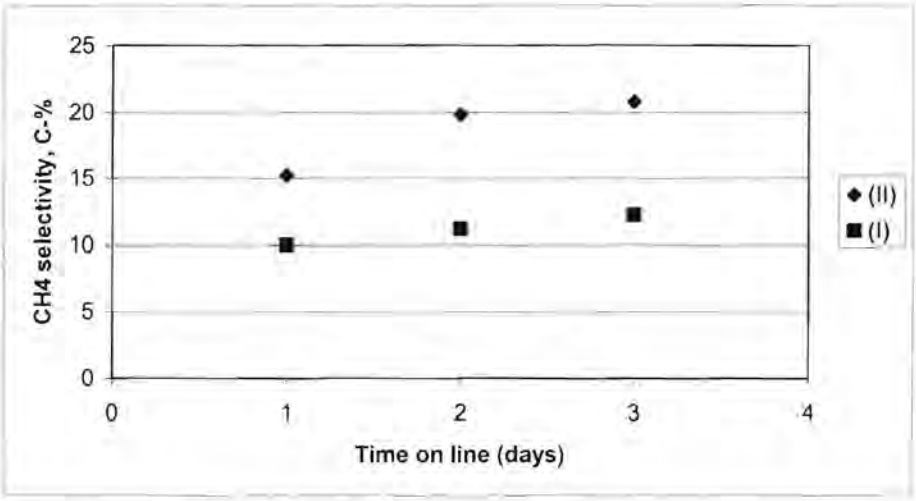

Figure 3.24: CH_4 selectivity graph over Fe-O

Figure 3.25 indicates that the chain growth probabilities obtained over the two Fe-O catalysts are 0.60 and 0.57 respectively, which are typically expected values for unpromoted catalysts operating at HTFT conditions (Dry, 1990). The CH_4 selectivity is relatively low, which is in accordance with these chain growth probabilities. The catalyst with the higher methane selectivity (Fe-O I) also rightly shows a lower chain growth probability. The chain growth probability obtained by Herranz et al. (2006) is 0.57. This corresponds to the value obtained over the Fe-O II catalyst. The Fe-O catalysts show a slight negative deviation in C_2, which can be ascribed to the high reactivity of C_2 (Schulz et al., 2002).

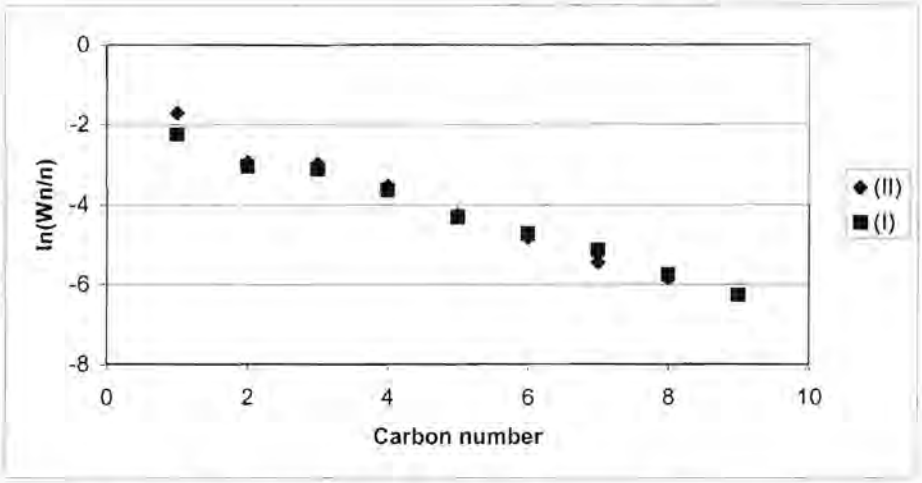

Figure 3.25: ASF distribution of products over Fe-O

Figure 3.26 indicates that the olefin content in the hydrocarbon product formed over the Fe-O I catalyst is relatively high, with the exception of C_2, which can be explained by increased reactivity of the C_2 olefin. The highest value over the carbon number range is 87%. The olefin content in the fraction C_3-C_7 is above 80%, but then starts to decrease from C_8 onwards. This might be caused by readsorption of the longer olefins and subsequent secondary hydrogenation.

The olefin content in the products obtained over Fe-O II is slightly lower than that obtained over Fe-O I. The maximum olefin content occurring at C_4 is 80%. The C_6-C_9 fraction has a lower olefin content, which seems to be constant from C_7 onwards.

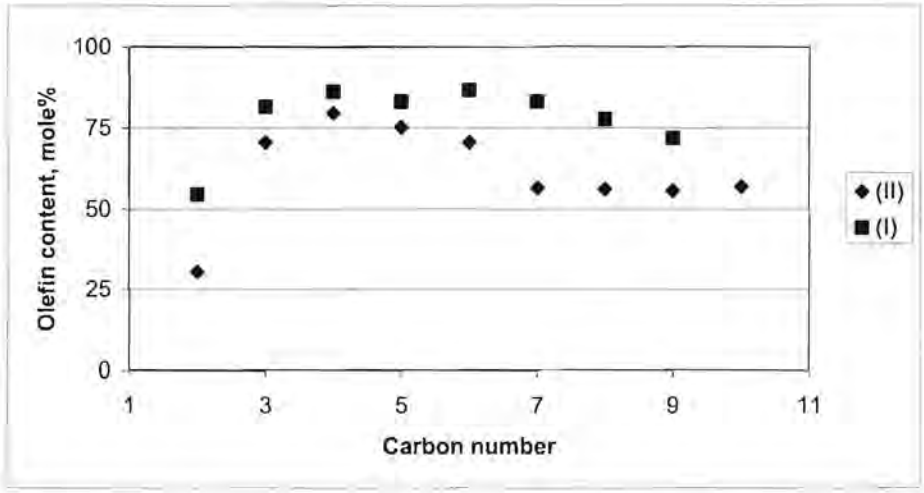

Figure 3.26: Olefin content in hydrocarbon products over Fe-O

Figure 3.27 shows the 1-olefin content in the hydrocarbon products formed over the Fe-O catalysts. The 1-olefin content formed over Fe-O I is constant with an increase in carbon number, up to about C_8. The high 1-olefin content indicates that there is very little double-bond isomerisation taking place over this catalyst. Only at C_{10} does the 1-olefin content begin to decrease, which could be the result of higher solubility of these long chains and subsequent readsorption and double bond isomerisation. The 1-olefin content in linear olefins is significantly lower over the Fe-O II catalyst. The same trend (constant up to about C_7) 1-olefin content as on the Fe-O I catalyst is also seen on Fe-O II.

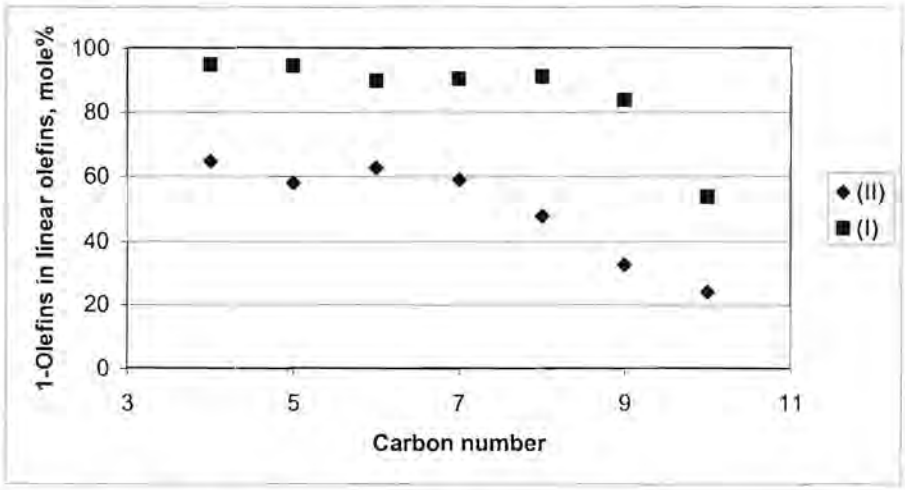

Figure 3.27: 1-Olefins in linear olefins over Fe-O

3.2.2 Fe-C

From the mass balance on the reaction over the Fe-C catalyst, it was calculated that only 93% of the reactants fed are accounted for.

Figure 3.28 shows that the H_2 conversion for the Fe-C catalyst was stable at about 24% for the first three periods and then went to 27% after four days on line. The CO conversion showed a steady increase over the four days, starting at 57% and ending the run at 69%. This indicates that the catalyst had not yet stabilised and was still transforming. This transformation could be from metallic iron and cementite (Fe_3C) to the active Hägg carbide ($Fe_{2.5}C$) phase, as was reported by Malan et al. (1961) and Herranz et al. (2006). The crystallites could also have been breaking up into smaller FeC_x crystallites which results in a larger number of active sites for CO adsorption and subsequent Fischer-Tropsch synthesis (Li et al., 2002).

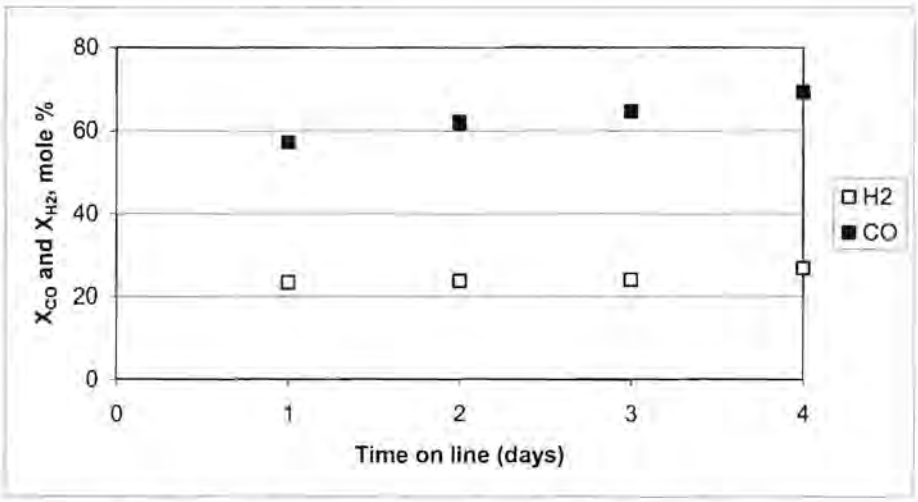

Figure 3.28: H_2 and CO conversion graph over Fe-C

It can be seen in Figure 3.29 that the $CO+CO_2$ conversion is only about 30%. The operating conditions are such that the water-gas shift reaction will be at equilibrium, but it seems as though the CO is being converted to CO_2, as indicated in Figure 3.30.

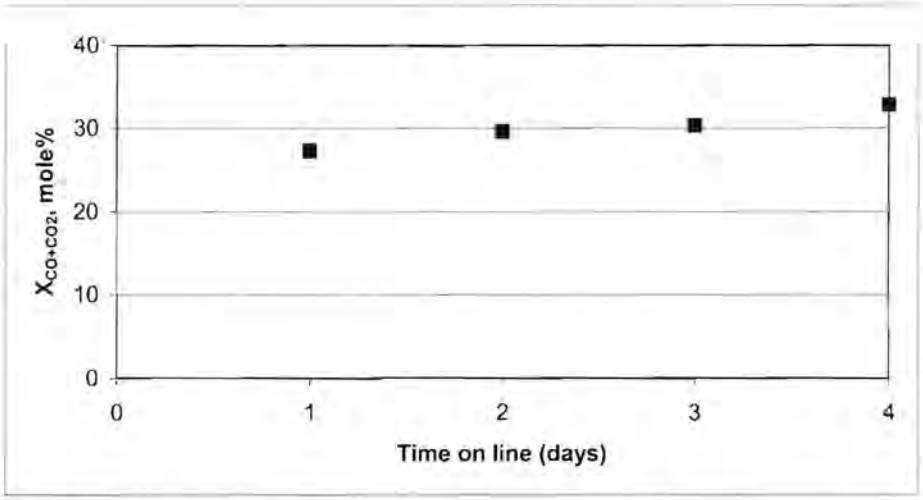

Figure 3.29: $CO+CO_2$ conversion graph over Fe-C

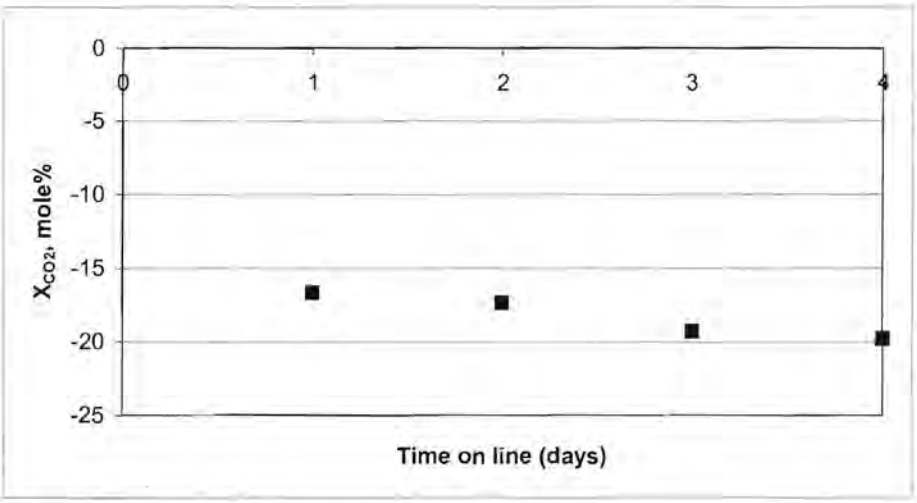

Figure 3.30: CO_2 conversion graph over Fe-C

The methane selectivity (Figure 3.31) of the Fe-C catalyst indicates an average of 21% over the four periods. There is a slight increase over time, which could be ascribed to the fact that the catalyst is still in the process of transforming to the stable iron phase. This methane selectivity is slightly higher than that obtained over pure cementite by Herranz et al (2006). These researchers reported a value of 16%. This discrepancy could be due to the fact that the operating temperature employed by them was lower (300 °C). An increase in methane selectivity with an increase in temperature is reported by Claeys (1997).

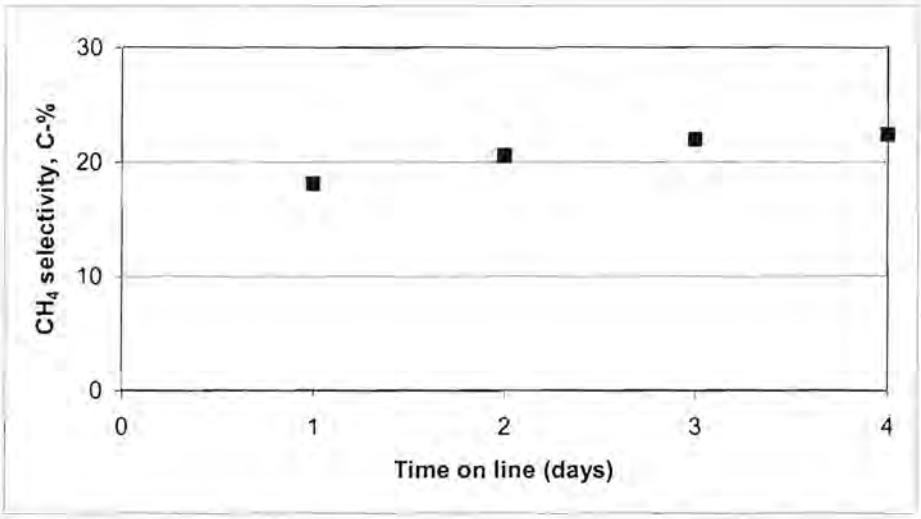

Figure 3.31: CH_4 selectivity graph over Fe-C

Figure 3.32 shows that the linear hydrocarbon products formed over Fe-C at about 48 hours on line show fairly linear ASF distribution within the range of carbon numbers indicated. The chain growth probability of 0.54, determined over the C_3-C_9 range, also corresponds to the relatively high methane selectivity. Herranz et al (2006) reported an alpha value of 0.58. This difference could be due to different operating conditions (300 °C, 10 bar, fixed bed reactor) employed by Herranz et al. (2006). The slightly lower value for C_2 is a noted deviation from the ASF distribution.

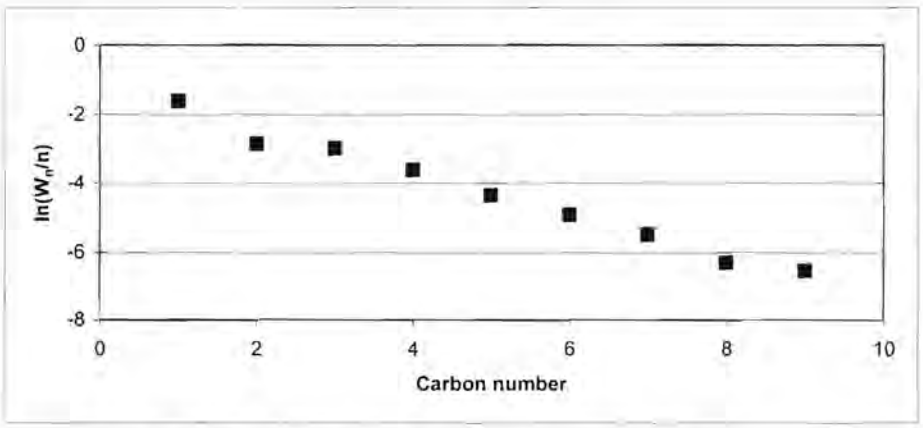

Figure 3.32: ASF distribution of products over Fe-C

The olefin content (see Figure 3.33) in the fraction of linear hydrocarbon product formed over the Fe-C catalyst is low for C_2. This could be a result of readsorption of ethane for further chain growth or desorption through hydrogenation. The olefin content of the C_3-C_7 fraction seems constant (82%), with a slightly higher maximum value at C_4. This might be explained by an overestimation from the GC analysis due to difficulty in separation between the 1-butene and 2-methyl propene. From C_8 onwards, there is a slight decrease in the olefin content because of the higher solubility of these olefins, and subsequent readsorption.

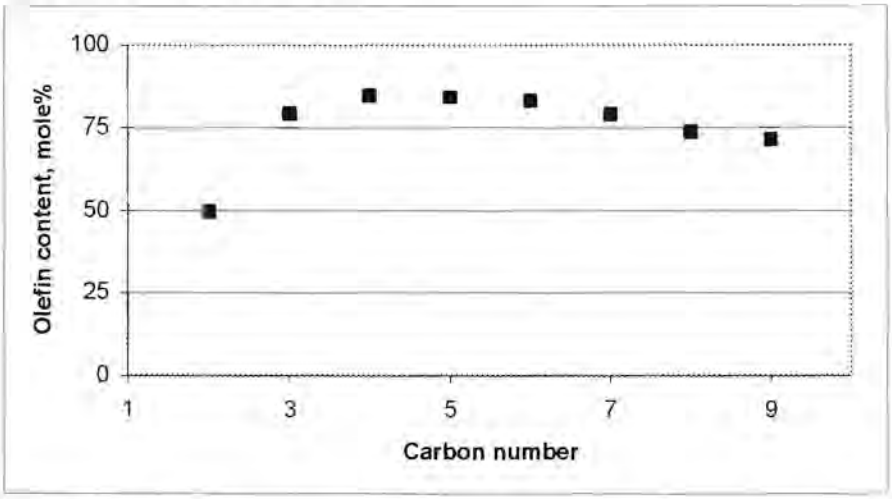

Figure 3.33: Olefin content in hydrocarbon products over Fe-C

Figure 3.34 shows that the 1-olefin content in linear olefins is almost constant at 80% for C_4-C_8. This indicates that there is not much double bond isomerisation of this fraction of olefins taking place over this catalyst. At higher carbon numbers, the 1-olefin content decreases, since there is more readsorption taking place due to higher solubility of these olefins. The fact that the 1-olefin content is less than 100% for C_4 and constant for the range C_4-C_8 might be taken as an indication that the internal olefins are formed in primary reactions. This has implications on the reaction pathway believed to be taking place on the catalyst, as deduced from the observed products.

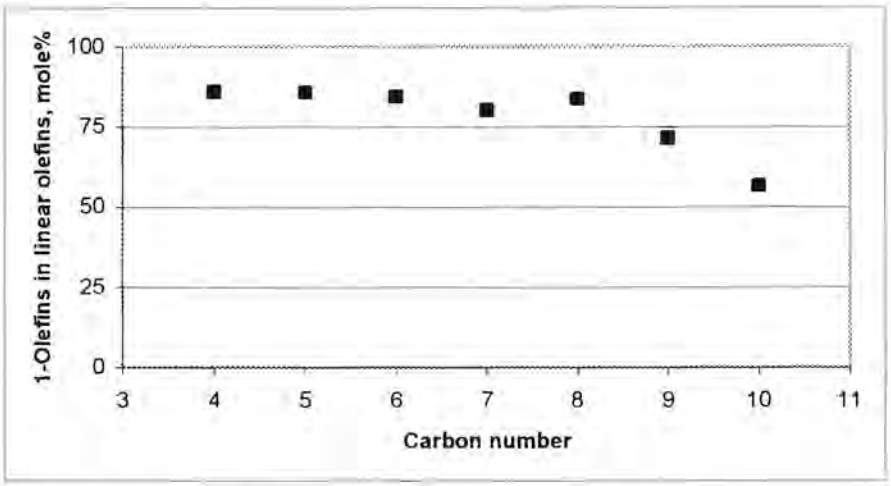

Figure 3.34: 1-Olefins in linear olefins over Fe-C

3.2.3 Mo-C

The mass balance of the Fischer-Tropsch synthesis over the Mo-C catalyst indicates that 99% of the reactants fed to the reactor are accounted for.

Figure 3.35 shows that the H_2 conversion for the Mo-C catalyst is about 5% throughout the run. The CO conversion is also stable at a value of between 6% and 7%. The correlation between H_2 and CO conversions obtained over the catalysts show similarity (CO conversion only slightly higher), which is different to the observation by Patterson et al. (2003) who reported a CO conversion twice that of H_2. This could be due to CO not being the only source of C in this reaction.

The conversions observed here (Figure 3.35) correspond to the conversions obtained by Patterson et al. (2003). They obtained a CO conversion of 14% and H_2 conversion of 8% over the Mo-C catalyst, despite the nine times greater surface area on the catalyst tested by them. The difference could be ascribed to the different operating conditions in terms of the feed and reaction temperature employed by these researchers.

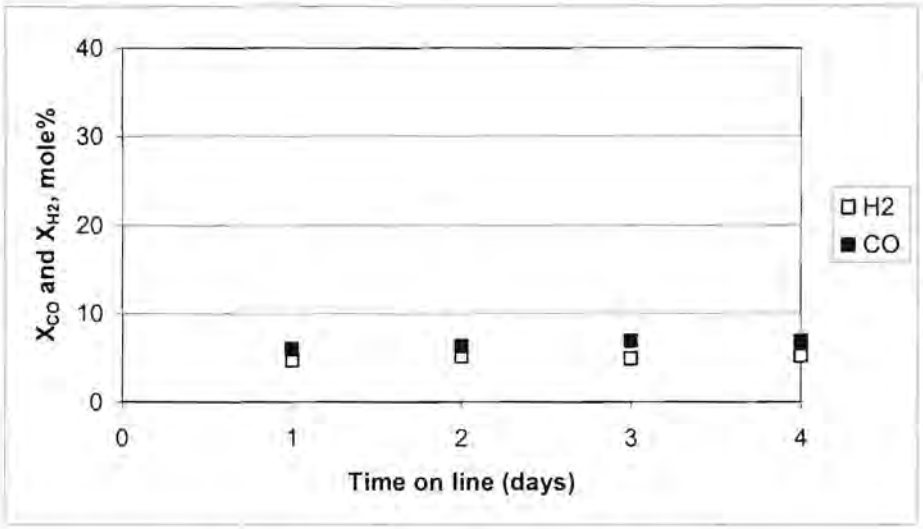

Figure 3.35: H_2 and CO conversion graph over Mo-C

The $CO+CO_2$ conversion (Figure 3.36) observed over the Mo-C catalyst is about 4%. Figure 3.37 indicates that no CO is being converted to CO_2 over the Mo-C catalyst. About 1% of the CO_2 that is co-fed to the reaction is converted in the reaction. This indicates that the reverse water-gas shift reaction is taking place over the Mo-C.

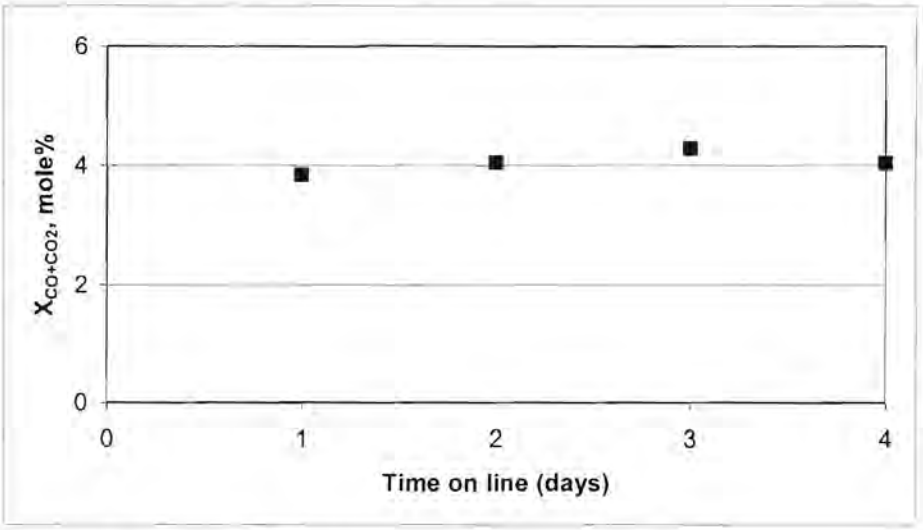

Figure 3.36: $CO+CO_2$ conversion graph over Mo-C

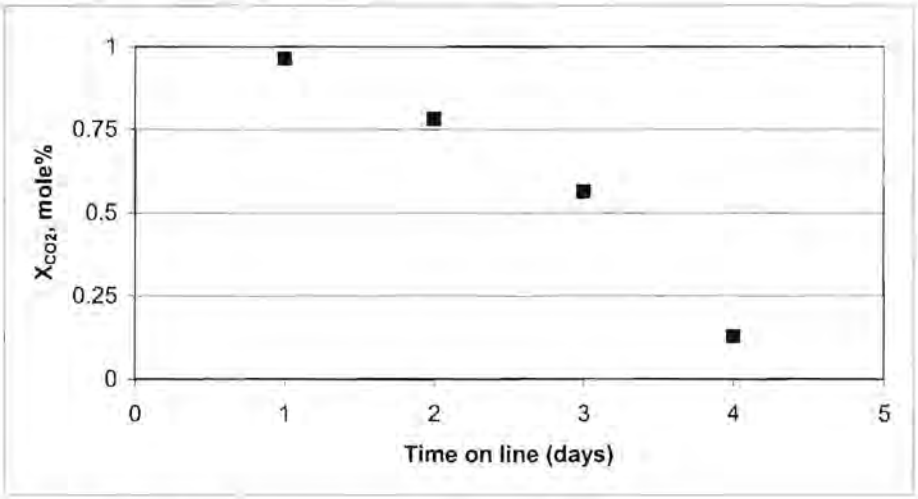

Figure 3.37: CO_2 conversion graph over Mo-C

It can be seen in Figure 3.38 that the methane selectivity over the Mo-C catalyst is about 60%. This is an indication that this catalyst is not facilitating much chain growth. The methane selectivity is also fairly constant over the four days, which could mean that the catalyst is stable.

The methane selectivity obtained by Patterson et al. (2003) was just lower than 40%. This lower value corresponds to the slightly higher CO conversion obtained over the catalyst, since it has been noted that lower methane selectivities can occur at higher CO conversion.

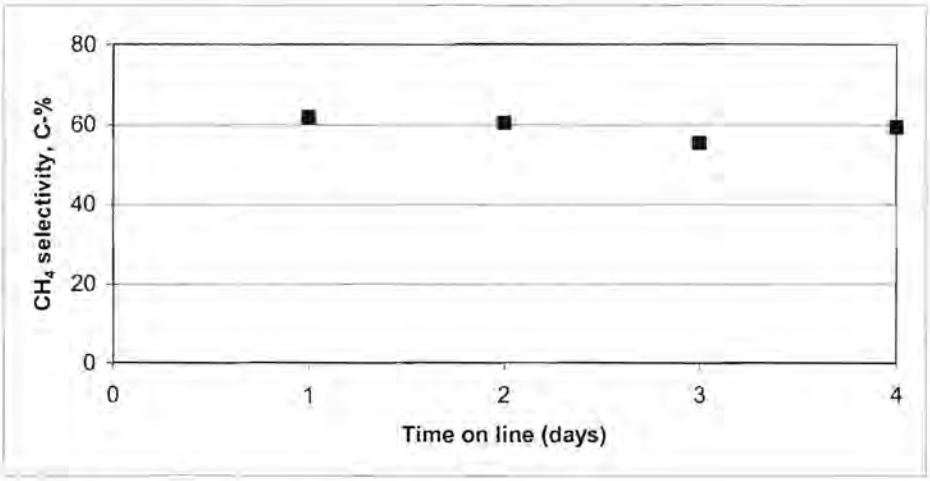

Figure 3.38: CH_4 selectivity graph over Mo-C

The chain growth probability of 0.38 (see Figure 3.39) and high methane selectivity correspond with each other. The fact that there is 60% methane formed shows that there is not much chain growth taking place on the catalyst. The linear hydrocarbon products up to about C_9 are used for the calculation of α for this catalyst at about 48 hours on stream.

The expected deviations from ASF distribution at C_1 and C_2 are not observed in the hydrocarbon products formed over this catalyst.

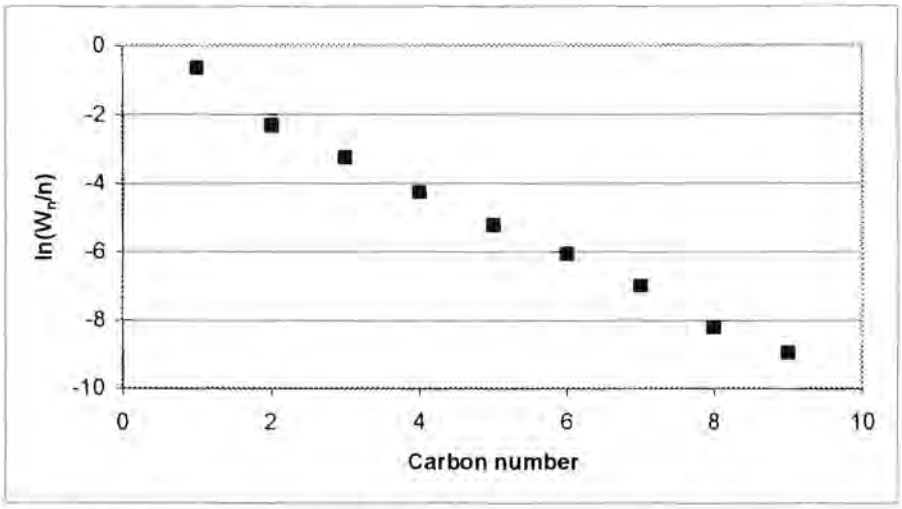

Figure 3.39: ASF distribution of products over Mo-C

It can be seen from Figure 3.40 that the olefin content of the C_2 fraction is relatively low because of readsorption and secondary hydrogenation of ethene that is taking place. There is an increase in the olefin content with carbon number, and the highest value of 65% occurs at C_4. The olefin content then decreases after that, up to C_7, which has a value of 45%. The general form of the graph indicates extensive secondary hydrogenation of the olefins over the catalyst.

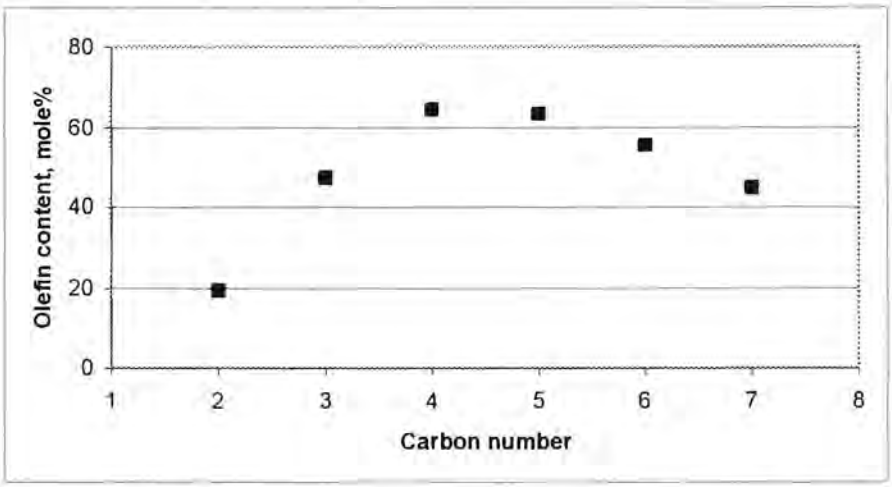

Figure 3.40: Olefin content in hydrocarbon products over Mo-C

It can be seen from Figure 3.41 that the 1-olefin fraction present in the linear olefin fraction is low. This is a result of double bond isomerisation. The average 1-olefin content in the C_4-C_7 fraction is 51%. The 1-olefin content is decreasing almost linearly over the indicated range, although this decrease is very slight.

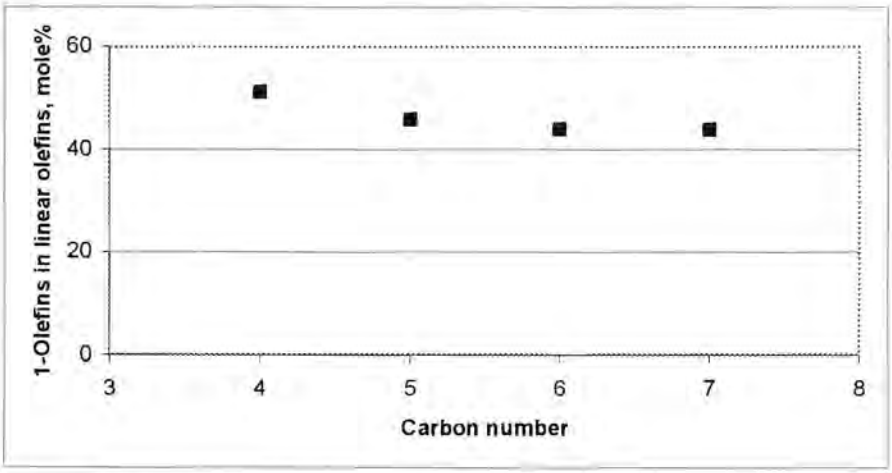

Figure 3.41: 1-Olefins in linear olefins over Mo-C

3.2.4 W-C

The mass balance of the reaction indicates a 97% accountability of the reactants.

It can be seen from Figure 3.42 that the H_2 conversion is decreasing slightly from 13% to a final value of 8%. The CO conversion, on the other hand, is stable throughout the run at a value of about 19%. The observation that in the first period, the H_2 conversion is more than half the CO conversion could be due to CO_2 being converted to CO.

The H_2 conversion is very similar to the 11% obtained by Patterson et al. (Patterson et al., 2003). The CO conversion, on the other hand is higher than the 16% reported by these authors. This observation is unexpected, due to 2.5 times higher surface area of the W-C catalyst tested by these authors, but could be explained by the lower operating temperature (300 °C) employed in the testing of their catalyst.

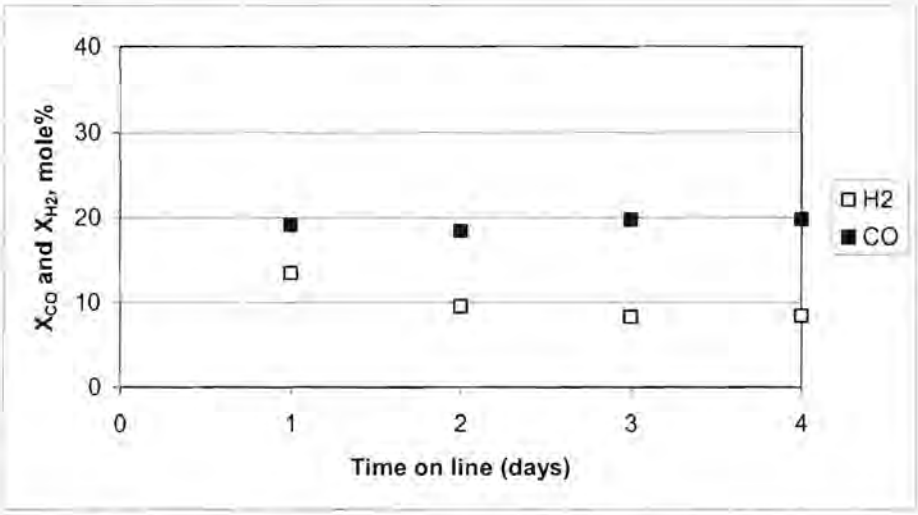

Figure 3.42: H_2/CO conversion graph over W-C

The CO+CO_2 conversion, as indicated in Figure 3.43, over the W-C catalyst after one day on line is greater than from the second day onwards. This could

be due to CO_2 also being converted in this period under Fischer-Tropsch conditions. Figure 3.44 confirms that initially some of the CO_2 is being converted, possibly into CO through the reverse water-gas shift reaction. Later the CO is converted into hydrocarbon products and CO_2.

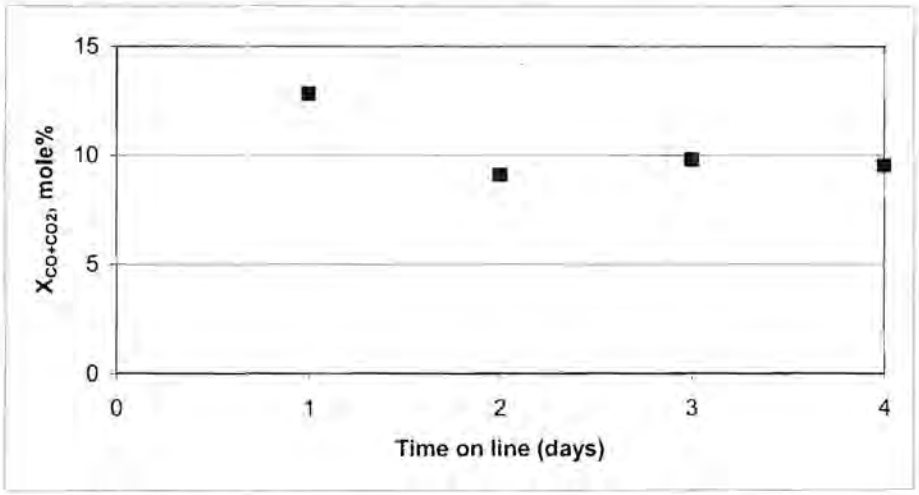

Figure 3.43: $CO+CO_2$ conversion graph over W-C

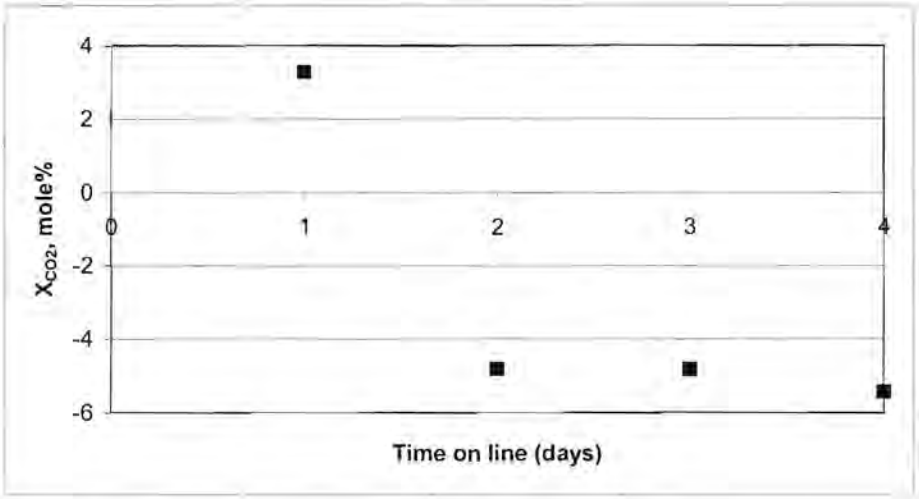

Figure 3.44: CO_2 conversion graph over W-C

The methane selectivity as indicated in Figure 3.45 is initially at 18%, but then as the catalyst stabilises under the Fischer-Tropsch conditions, the selectivity increases to about 30%. This level of methane selectivity then remains constant for the rest of the run.

The methane selectivity reported by Patterson et al. (Patterson et al., 2003) is about 60%. This higher value is consistent with the lower CO conversion obtained on their tungsten carbide catalyst.

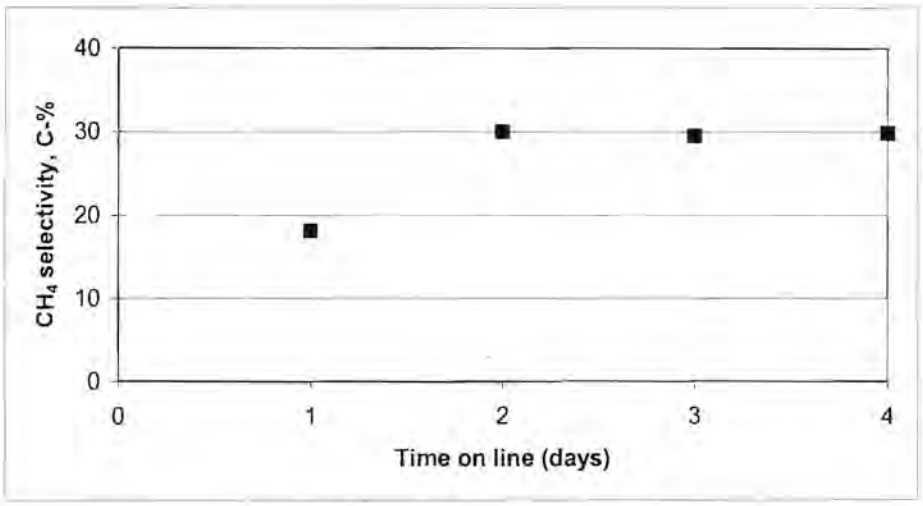

Figure 3.45: CH_4 selectivity graph over W-C

The chain growth probability (Figure 3.46) of the linear products of the W-C catalyst is 0.44, showing that shorter chains are favoured in the Fischer-Tropsch synthesis reaction. This is confirmed by the C_7 linear hydrocarbon being the longest chain observed in the product over this catalyst.

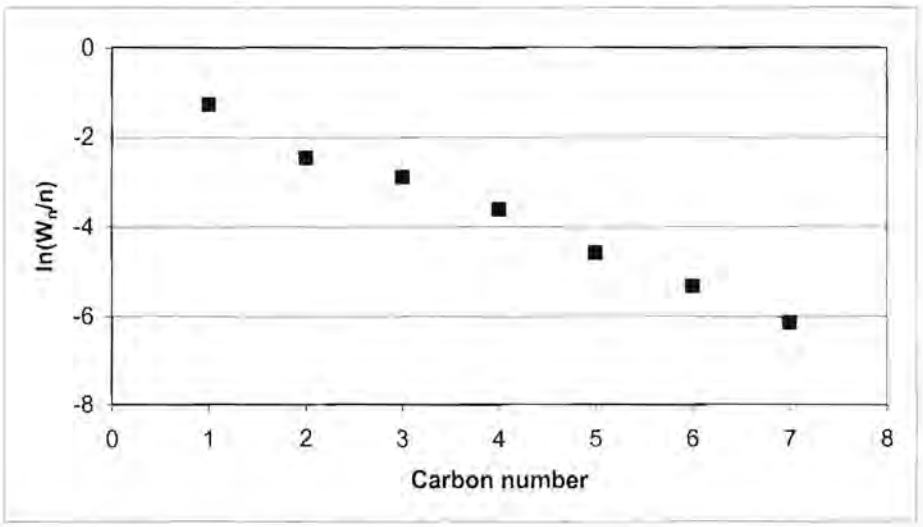

Figure 3.46: ASF distribution of products over W-C

Figure 3.47 shows the olefin content in the hydrocarbon product formed over W-C. The olefin content for the C_2 fraction is low as is expected, considering the fact that there is readsorption for further chain growth or desorption through hydrogenation of thane taking place. The average olefin content for the C_4-C_7 the carbon numbers is 58%, with the highest value occurring for C_4.

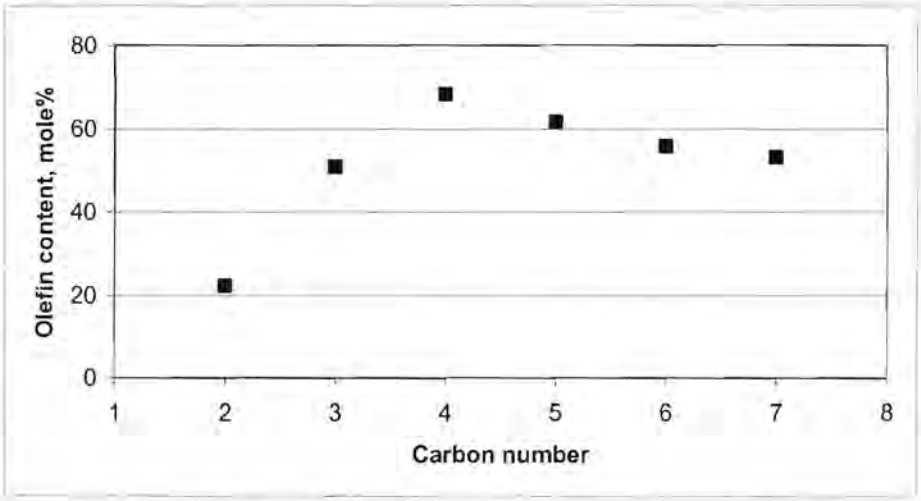

Figure 3.47: Olefin content in hydrocarbon products over W-C

Figure 3.48 shows the 1-olefin content of the W-C catalyst. The 1-olefin content in the linear olefins is very low and on average 28% for the C_4-C_7 fractions. This might suggest that double bond isomers are formed to a large extent over WC.

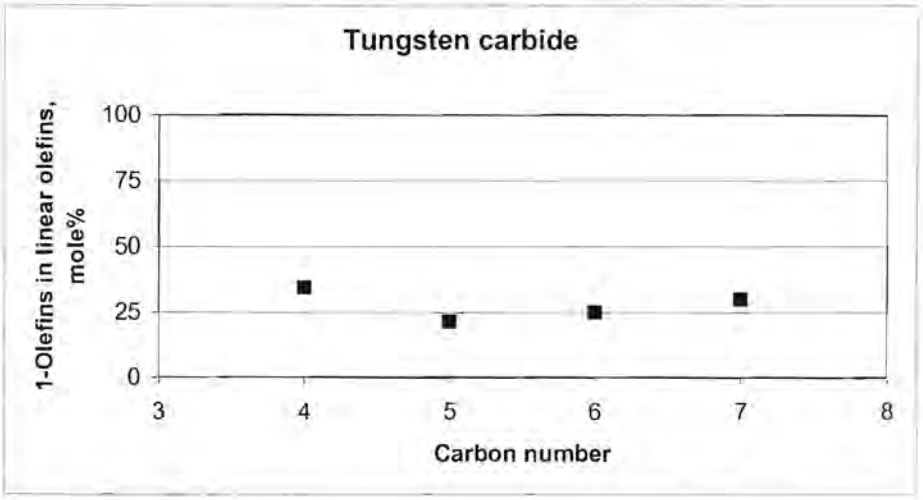

Figure 3.48: 1-Olefins in linear olefins over W-C

3.2.5 Oxygenate content

The oxygenate content, expressed as a percentage of the total hydrocarbon products of the C_2 fraction is presented in Figure 3.54. It can be seen that the oxygenate content of all the carbidised catalysts is between 8% and 10%, while that of the Fe-O catalysts are 12% and 12.4%. The oxygenate content appears to be affected by the electronic structure of the catalyst, since the Group VI metal carbides show a slightly lower oxygenate content than the iron catalysts. The iron catalysts (Fe-C and Fe-O) indicate that the activation method of the catalyst also possibly has an effect on the oxygenate content.

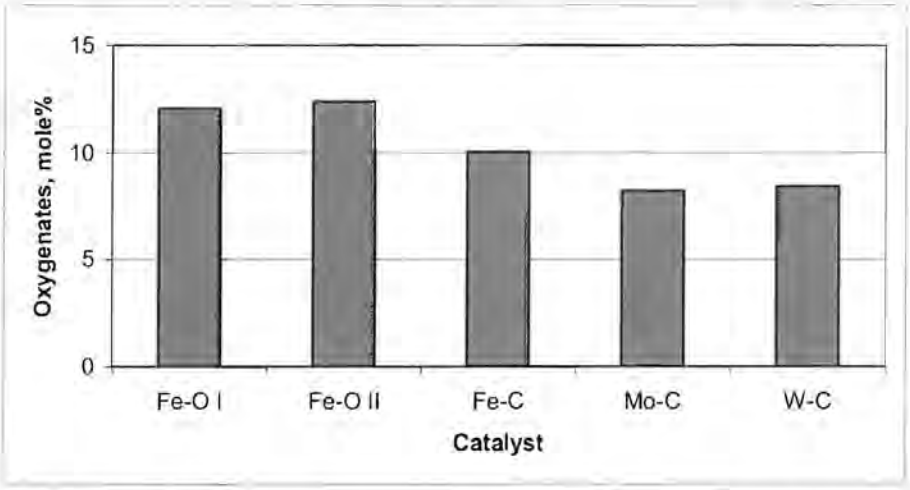

Figure 3.49: Oxygenate content in hydrocarbon products of C_2 fraction

The oxygenate content in the C_3 and C_4 in each case shows a decreasing trend, except for the W-C catalyst. In the C_5 fraction, there are hardly any oxygenates in the products formed in the Fischer-Tropsch synthesis.

3.2.6 Branched products

The fraction of branched to linear hydrocarbons in the C_5 fraction is indicated in Figure 3.50. The fraction of the branched products formed over the five catalysts, shows no functionality. The branched products make up a very small percentage of the hydrocarbon product formed over the catalysts.

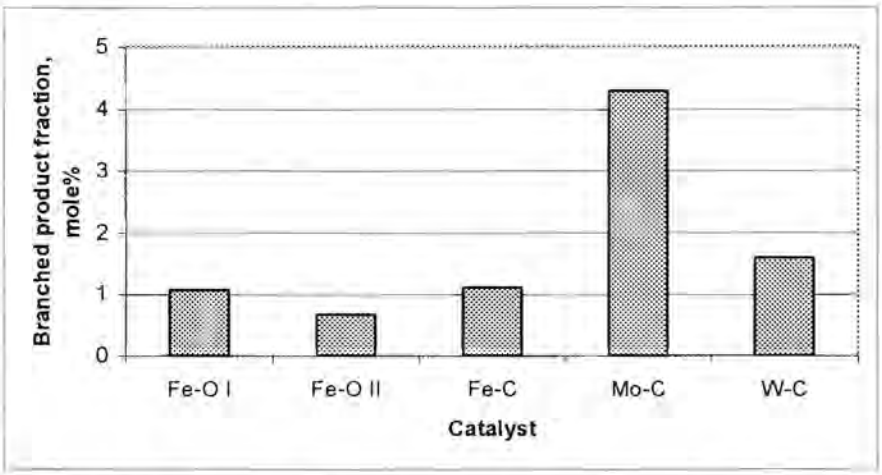

Figure 3.50: Fraction of branched products in linear C_5 hydrocarbons

3.3 Characterisation of spent catalysts

The spent catalysts were passivated using dry ice (CO_2), and kept for characterisation using XRD and TEM techniques. The characterisation was performed to observe any phase changes in the catalyst.

3.3.1 X-ray diffraction (XRD)

The XRD pattern of the spent Fe-O catalyst, as indicated in Figure 3.51, shows that the species has changed in the Fischer-Tropsch synthesis from the fresh, calcined catalyst that was loaded. The major peaks indicate the presence of synthetic magnetite (Fe_3O_4) and the Hägg carbide phase (Fe_5C_2). From the most intense peaks (by height) of the various phases, it appears as though Fe_5C_2 is the most abundant species.

$$\frac{I_{Fe_5C_2}}{I_{Fe_3O_4}} = 1.21 \qquad (1)$$

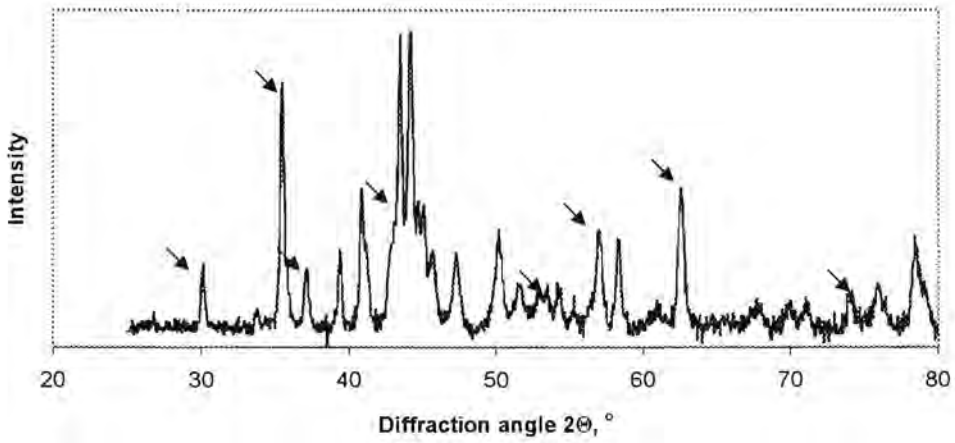

Figure 3.51: XRD pattern of spent Fe-O (Fe_3O_4 ↘ /Fe_5C_2)

The XRD pattern of the spent Fe-C, as indicated in Figure 3.52 shows that there is a difference in the phase of the spent catalyst from the fresh catalyst (Fe and Fe_3C). The major peak at 35.6° and the other peaks at 30.1°, 43.3°, 53.8°, 57.3° and 62.9° indicate the presence of magnetite (Fe_3O_4). These peaks all coincide with those of the phase Fe_2O_3 (synthetic maghemite-C), but the relative intensity of the peaks suggest that it is magnetite. The other distinguishable peaks represent the Hägg carbide phase (Fe_5C_2). The most intense peaks (by height) of the different iron phases indicate that the oxide is the most abundant phase present in the spent Fe-C catalyst.

$$\frac{I_{Fe_5C_2}}{I_{Fe_3O_4}} = 0.51 \qquad (2)$$

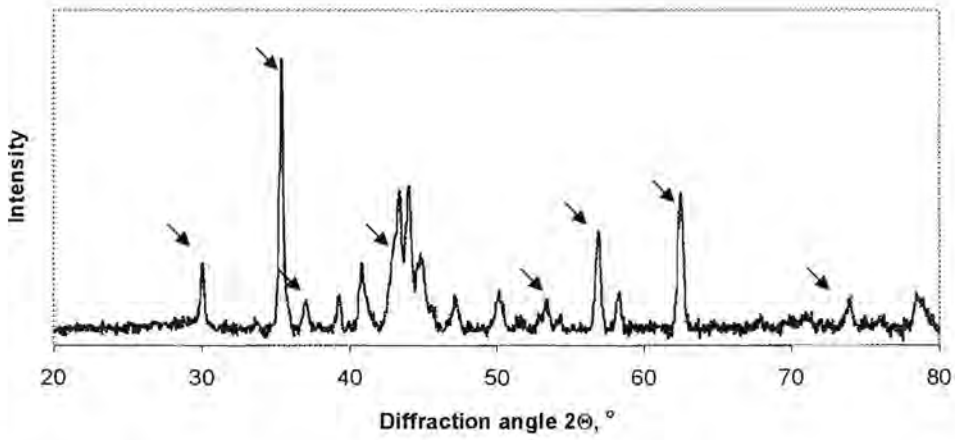

Figure 3.52: XRD pattern of spent Fe-C (Fe_3O_4 ↘/Fe_5C_2)

The XRD pattern (Figure 3.53) of the spent Mo-C catalyst appears to be the same as that of the fresh catalyst. The implication of this observation is that the Mo-C that was loaded into the reactor was stable in the Fischer-Tropsch reaction.

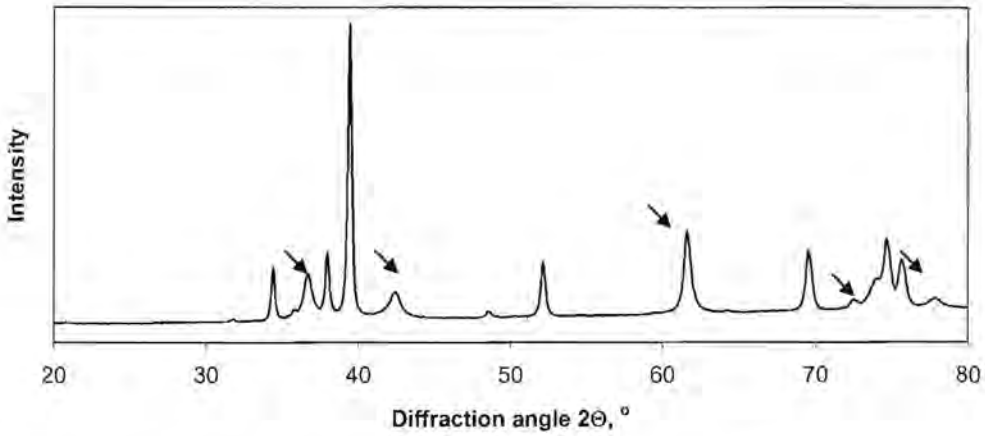

Figure 3.53: XRD pattern of spent Mo-C (Mo_2C/α-MoC_{1-x} ↘)

It can be seen from Figure 3.54 that the phase of the spent W-C catalyst is still exactly the same as the fresh catalyst. This indicates that the WC phase is stable under Fischer-Tropsch synthesis conditions.

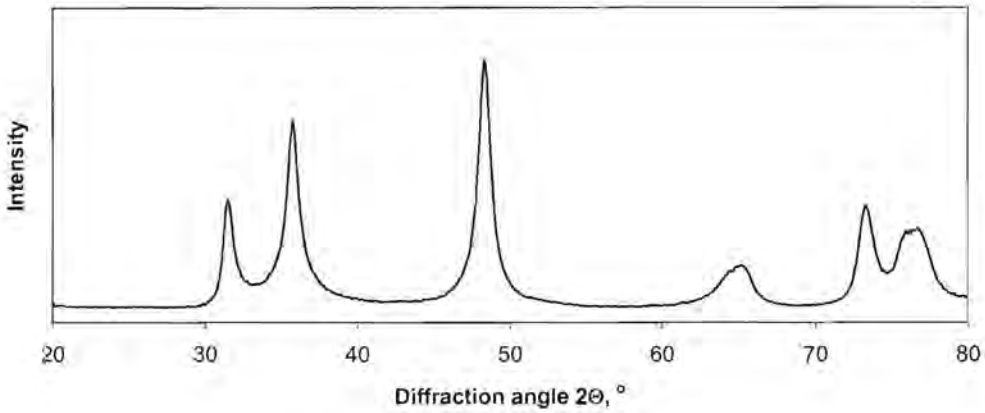

Figure 3.54: XRD pattern of spent W-C

3.3.2 Transmission electron microscopy (TEM)

Figure 3.55 shows that the particles of the spent Fe-O catalyst appear to have sintered in the Fischer-Tropsch reaction. There are still small crystallites present, but most of the particles are visible as large structures. There are also no amorphous graphite-like structures present. The crystallite diameters range from 37 to 50 nm, with an average crystallite size of 43 nm.

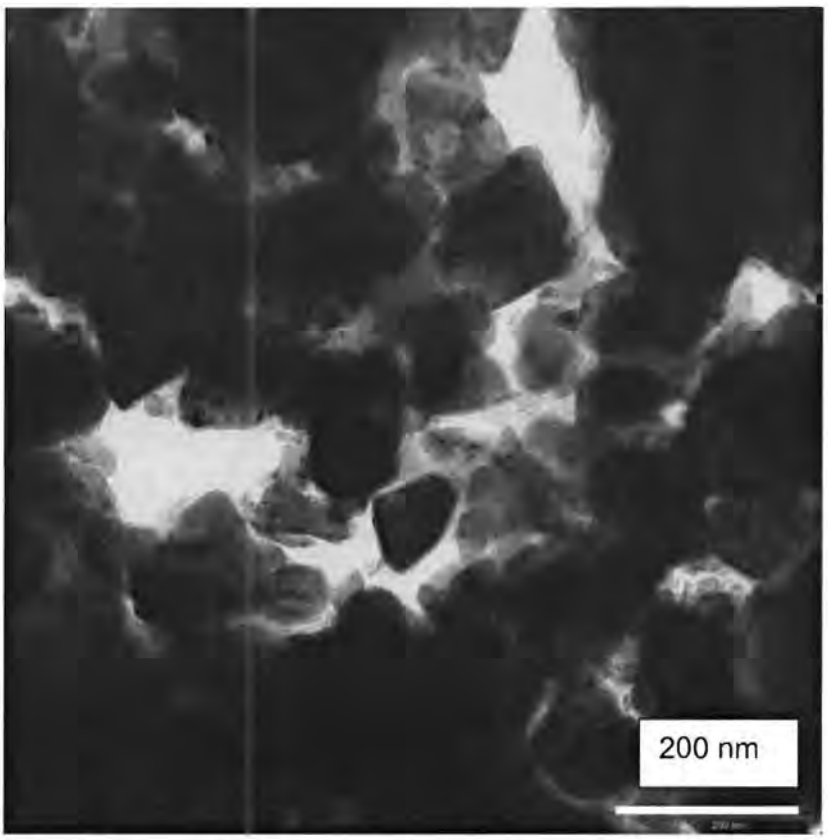

Figure 3.55: TEM image of spent Fe-O

The TEM image (Figure 3.56) of the spent Fe-C catalyst shows that a change (breakage) in the morphology of the crystallites has occurred. There are small spherical crystallites visible, as well as particles that appear platelet-like in shape. All the edges appear more rough and angular than those of the fresh catalyst crystallites. There are however, no graphite-like species visible. The sizes of the platelets are approximately equal to the distance between the flaws measured in the fresh catalyst. The crystallites range from 48 nm to 54 nm, with an average diameter of 50 nm.

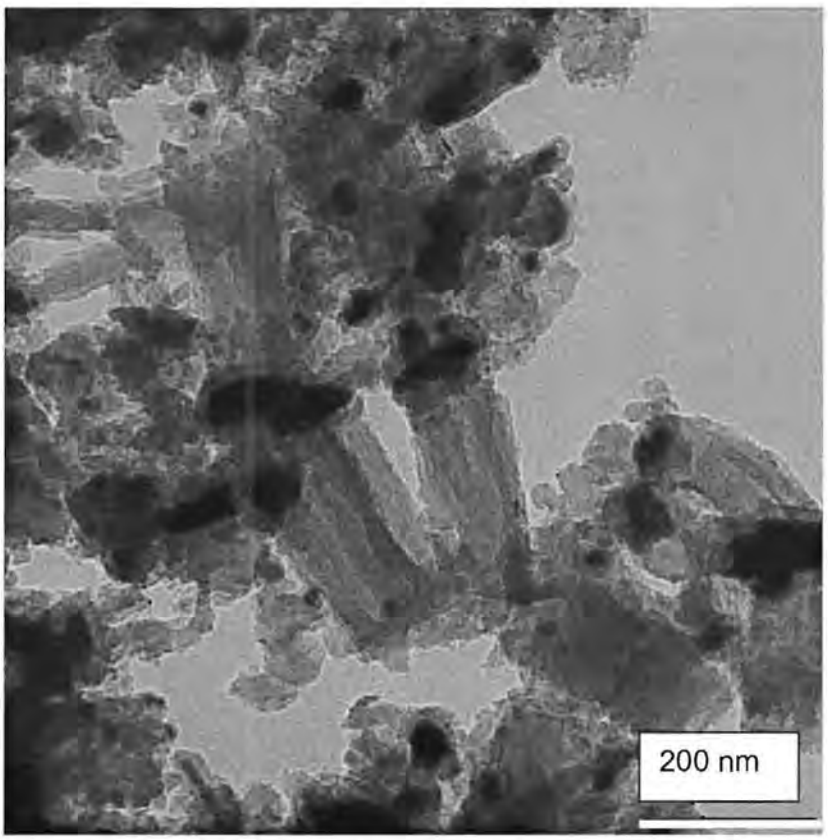

Figure 3.56: TEM image of spent Fe-C

It can be seen from Figure 3.57 that the crystallites of the spent Mo-C catalyst appear exactly the same as in the fresh catalyst. The same agglomerated needle-like structures that appear to consist of crystallites can be seen in the TEM image. The width of the needles appears to range from 37 nm to 51 nm, therefore essentially unchanged from those in the fresh catalyst. The average width of the needles is 46 nm.

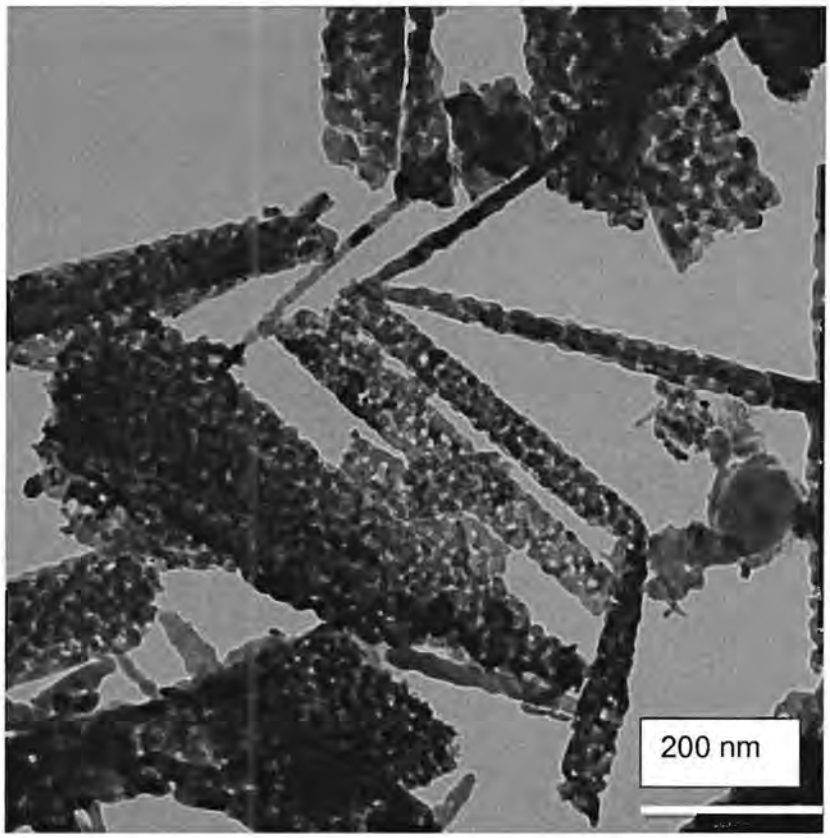

Figure 3.57: TEM image of spent Mo-C

The TEM image of the spent W-C catalyst, as indicated in Figure 3.58, shows that the morphology of the crystallites is very similar to the fresh catalyst crystallites. The crystallites in the image are not dispersed well enough to distinguish all the areas visible in the image, but the majority of crystallites are present as small spherical structures. The crystallites are still measuring about 20 nm in diameter, just as before being exposed to Fischer-Tropsch conditions. The sizes of the measured crystallites are between 18 nm and 22 nm.

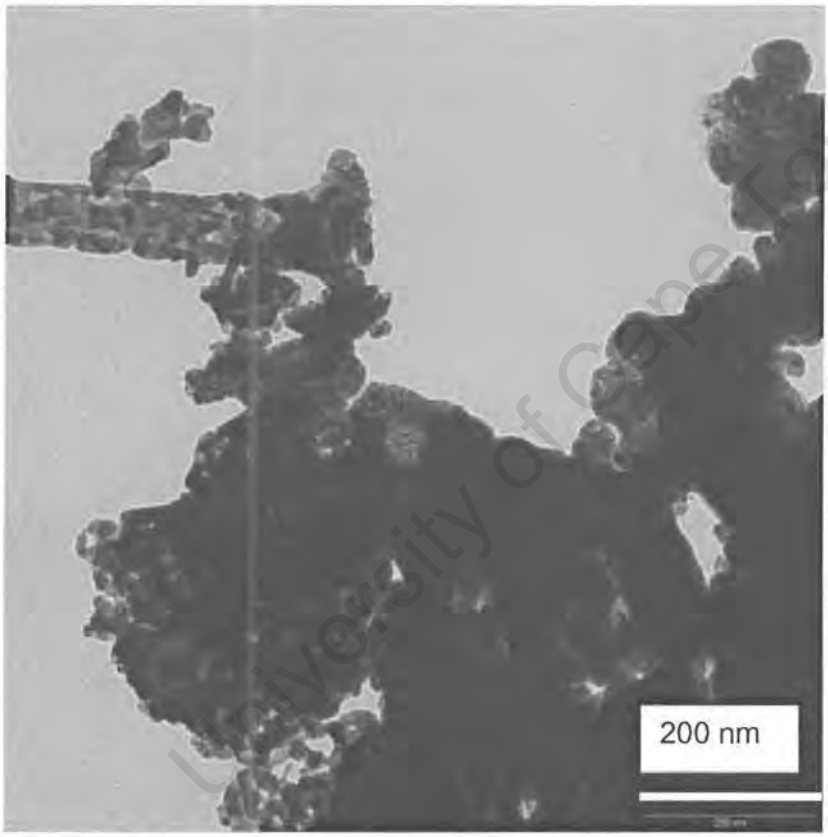

Figure 3.58: TEM image of spent W-C

4. Discussion

The early transition metal carbides have been found to be exceptional hydrogenation catalysts (Vidick et al., 1986). They have activity close to or surpassing those of the Group VIII noble metals for such diverse reactions such as methanation (Ranhotra et al., 1987), ammonia synthesis (Boudart et al., 1980), ammonia decomposition (Oyama, 1992 b), hydrocracking (Lee et al., 1987), hydrogenation of benzene and cyclohexene (Lee et al., 1991) and hydroisomerisation of n-hexane (Ledoux et al., 1992), n-heptane (Ribeiro et al., 1991 a) and methylcyclohexane (Ribeiro et al., 1991 b). Considerable work is also being done in the area of hydroprocessing (Schlatter et al., 1988), where the materials have been shown to have high activity for both hydrodesulfurisation (HDS) (Markel et al., 1990; Nagai and Miyao, 1993) and hydrodenitrogenation (HDN) (Lee et al., 1993; Sajkowski and Oyama, 1996; Colling and Thompson, 1994). Little has been published on early transition metal carbides as Fischer-Tropsch catalysts. The use of tungsten and molybdenum carbides as Fischer-Tropcsh catalysts has been investigated (Patterson et al., 2003). The molybdenum carbide was found to have a high water-gas shift activity, and the main hydrocarbon product on both catalysts was methane.

In this study, an investigation of the Fischer-Tropsch activity and selectivity of the transition metal (iron, molybdenum and tungsten) carbides (Fe-C, Mo-C and W-C) was carried out. The physical properties of the catalysts were related to their catalytic performance under Fischer-Tropsch synthesis conditions. The physical properties of the different metal carbides were characterised using BET surface area measurements, X-ray diffraction (XRD), Transmission Electron Microscopy (TEM) and Temperature Programmed Desorption of CO (CO-TPD). Table 4.1 summarises the physical properties of the catalysts obtained from the different characterisation procedures.

Table 4.1: Summary of the physical properties of catalysts

Species	Fe_2O_3	MoO_3	WO_3	Fe_2N	Mo_2N	W_2N	Fe/ Fe_3C	Mo_2C mix	WC
Surface area (m^2/g)	30	7	3	6	10	20	1	14	18
BET crystallite size (nm)	38	186	286	-	-	-	794	49	21
XRD crystallite size (nm)	40	52	62	48	24	16	60	43	22
TEM crystallite size (nm)	40	56	65	50	31	21	51	44	21

The surface area of the iron carbide/metallic iron catalyst does not correspond to the crystallite sizes. The BET measurements were repeated and were found to be reproducible. It must be noted that the measurements on the TEM image were done between the flaws within the visible structures. There were no single crystals visible on the images, but rather large particles that could have diameters in excess of 200 nm. The surface area measurements taken place on these large particles, since the BET surface area is measured on the places which are penetrable by the nitrogen used in the analysis.

4.1 Synthesis of catalysts

In the preparation of these catalysts, the metal oxide precursor was transformed to the nitride intermediate, which was in turn transformed to the carbide. In the transformation, the pseudomorphism reported by Boudart and coworkers (Volpe and Boudart, 1985 a; Volpe and Boudart, 1985 b; Lee et al., 1987; Lee et al., 1988) was not consistently observed. This topotactic

transformation could be limited to relatively small crystallites (7 nm in literature), which would explain that it did not occur in the prepared species. Another possibility is because the reactions were not quenched after the final stage of the heating profile, as was done in the literature. The phases of the molybdenum carbides (hexagonal) also differ from those reported by the authors mentioned above. These authors reported that the molybdenum and tungsten carbide was the pure face-centred cubic $MoC_{0.45}$ and $WC_{1.54}$ phases respectively. This further suggests that the temperature profiles used in this study are not the same as those reported in literature, due to quenching only being done once lower temperatures (500 °C) had been reached.

The XRD patterns for each species indicate that all the oxide precursors and prepared nitride intermediates are phase pure. The peaks that can be seen in each XRD-pattern are all indicative of the assigned phase. This means that all these transformations were complete. Only the carbidisation of the W_2N was complete. The iron nitride was transformed into a mixture of metallic iron and cementite. The following heating profile would have resulted in pure iron carbide: 500 °C for 4 hours, but this is for pure (100%) methane (Anderson, 1984) and therefore promotes free carbon formation. The fact that the species consisted of mostly the metallic phase would have had an impact on the stability in air. The molybdenum nitride was transformed into a mixture of molybdenum carbide, which consisted mostly of Mo_2C. The mixture of phases might have resulted from the slow cooling in the preparation. It is possible that in passing through the lower temperatures, the Mo_2C transformed to the carbide phase that is more stable under these conditions.

4.2 Stability in Fischer-Tropsch synthesis

The results from XRD and TEM show that the prepared species had fairly large crystallites. This physical property of the catalyst particles was required to promote the stability of the carbide phase under Fischer-Tropsch synthesis conditions. The stability of a small crystallite is decreased by the large surface energy contribution of the crystallites.

The effect of these large crystallites can be seen in the surface area measurements. The surface areas obtained by Patterson et al. (2003) that prepared molybdenum and tungsten carbides using the same method, was 95 m^2/g and 52 m^2/g respectively. The surface area on the iron carbide/metallic iron mixture (Fe-C) is very low. This could be explained by the large structures that can be seen on the TEM image of this species. The fact that it consists of mostly metallic iron also complicates the observed characterisation data. The temperature at which the carbidisation was performed was therefore incorrect to obtain phase-pure carbide.

Other than the difference brought on by the large crystallites, the lower surface area could also have been a result of the needle-like structures observed in the TEM images of the molybdenum carbide or the spherical crystallites in tungsten carbide. Boudart and coworkers (Volpe and Boudart, 1985 a; Volpe and Boudart, 1985 b; Lee et al., 1987; Lee et al., 1988) previously reported an anisotropic platelet shape for these early transition metal carbides. These researchers started off with these platelets and topotactically transformed these oxides through to the nitride and then the carbide. In terms of the spherical particles of the oxide precursors in this study, these platelets were seen throughout the transformation. In the carbidised materials the spherical particles were agglomerated as needles or clusters.

The transformation of the tungsten and molybdenum oxides to the corresponding nitrides is accompanied by a reduction in crystallite size. There is a slight enlargement of these nitride crystallites upon transformation to the carbide for the tungsten. This enlargement is due to the difference in the density of the different species. This observation is more pronounced than expected from density differences for the molybdenum. The temperature used for the transformation of the molybdenum species was near the melting temperature, which could explain the enlargement of these crystallites with carbidisation. The iron transformations are all accompanied by an increase in crystallite size.

There was no free carbon deposition observed in the spent catalysts. The XRD showed no graphite peaks, while the TEM images showed no material that was not attributable to the catalysts.

The molybdenum and tungsten carbides were unchanged in the Fischer-Tropsch synthesis. This is because the conversions obtained over these catalysts were well within the allowed conversion for stability of the carbides, as was calculated thermodynamically.

The Fe-C catalyst (cementite/metallic iron mixture) transformed to Hägg carbide and magnetite after about 96 hours on line. This was because the conversion obtained over the catalyst was very close to the limiting conversion for the carbide. With increased time on stream, the enrichment of carbon in the catalyst would lead to the formation of Hägg carbide. It was observed that stability conversion was exceeded in the last 48 hours on line. This is then the reason for the observed oxide phase present in the spent catalyst. It was noted that the crystallites had broken up during synthesis, leading to increased surface area.

The Fe-O catalyst showed the same phase transformations as the cementite/metallic iron (Fe-C) catalyst. This suggests that the phase of iron loaded into the reactor does not necessarily determine the catalyst stability.

4.3 Activity of metal carbides

The overall performance of the iron carbide/metallic iron catalyst, Fe-C was better than the molybdenum carbide and tungsten carbide catalysts in the Fischer-Tropsch synthesis. The Fe-O catalyst performed similarly to the Fe-C catalyst. This observation can probably be attributed to phase transformations of the iron-based catalysts in the Fischer-Tropsch environment, which resulted in the same phases as for Fe-O and Fe-C.

4.3.1 Catalyst activity for Fischer-Tropsch synthesis

The activity of the materials for Fischer-Tropsch synthesis is defined as the amount of $CO+CO_2$ being converted in the reaction. The BET surface areas are used to express specific activity, since if the sites are not accessible by N_2 in the BET measurement (physisorption), they will probably not be accessible by syngas (chemisorption) either.

Table 4.2: Specific activity of carbides for Fischer-Tropsch synthesis (with respect to BET surface area)

Catalyst	Fe-C	Mo-C	W-C
Activity ($\mu mol/m^2.s$)	50	4	3

The specific activity on the Fe-C catalyst is considerably higher than on the early transition metal carbides, despite the fact that the catalyst is operated near limiting conversion. This could be due to optimum metal-carbon (from the dissociation of CO on the surface) bond strength in the iron-based catalyst, with the bonding in molybdenum and tungsten carbides possibly being perhaps too weak.

The specific activity on the tungsten carbide catalyst is less that on the molybdenum carbide catalyst. Considering the additional electron shell on tungsten compared to molybdenum, this observation might be explained by weaker M-C bonding and therefore lower reactivity down the Group VI metals.

The relatively low activity on the early transition metal carbides could be explained by the operating conditions not being optimum for these catalysts. The fact that no transformation was observed on these catalysts with Fischer-Tropsch synthesis indicates the stability of these catalysts under these conditions. These carbides are likely to still be stable at higher temperature. From the thermodynamic considerations of the carbides under Fischer-Tropsch conditions it can be seen that the oxidation of iron-based catalysts is

more likely than for the early transition metal carbides at the employed operating conditions.

4.3.2 Water-gas shift activity

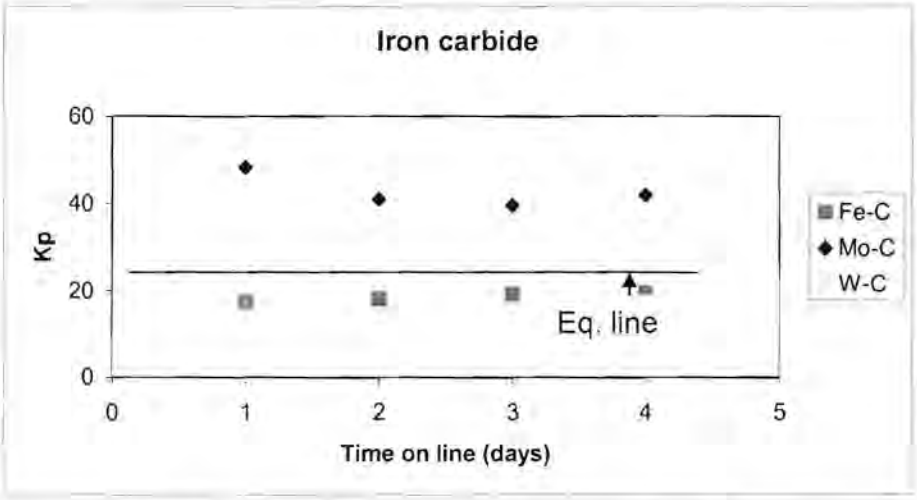

Figure 4.1: Equilibrium constants for water-gas shift reaction

The water-gas shift reaction can be represented as follows:

$H_2O + CO \rightarrow CO_2 + H_2$ (1)

The water-gas shift equilibrium constant is given by the following equation:

$$K_P = \frac{p_{H_2} \cdot p_{CO_2}}{p_{H_2O} \cdot p_{CO}} \quad (2)$$

The equilibrium constant calculated from the Gibbs free energy of the reaction at a specific temperature (330 °C) is 24. It can be seen from Figure 4.1 that the equilibrium constant for the water-gas shift reaction is relatively high for the molybdenum carbide catalyst. This observation corresponds with the findings of Patterson et al. (2003) that molybdenum carbide is a good water-gas shift catalyst.

Table 4.3: Specific activity of carbides for water-gas shift reaction (with respect to BET surface area)

Catalyst	Fe-C	Mo-C	W-C
Activity ($mmol/m^2.s$)	-3.8E-3	1E-5	3.7E-5 then -5.7E-5

The water-gas shift activity on the Fe-C catalyst indicates that CO_2 is being formed on the catalyst. The water-gas shift equilibrium constant tested under these conditions was about 20. The observed activity, taken in terms of the number of mole of CO_2 formed, indicates that the water-gas shift reaction rate over the carbide catalysts is very low. The activity on the molybdenum carbide is negative. This indicates that the reverse water-gas shift reaction is taking place to a small extent on the catalyst. The water-gas shift activity obtained on the tungsten carbide is initially positive and then it becomes negative. This indicates that under these conditions, the water-gas shift reaction is very close to equilibrium. The observed water-gas shift activities are strongly influenced be CO_2 being co-fed in the reaction.

Table 4.4: Summary of selectivity data over catalysts

	Fe-C	Mo-C	W-C
S_{CH4}, C-%	20	60	30
α-value	0.54	0.38	0.44
Olefin content in C_4, mol%	85	65	68
1-Olefins in n-olefin in C_4, mol%	86	51	34
Oxygenates in C_2, mol%	10	8	8
Branched in C_5, mol%	1.2	4.3	1.8

4.3.3 Chain growth probability

The chain growth probability observed in the hydrocarbon product formed over the Fe-C catalyst is higher than that of the tungsten carbide, with molybdenum carbide the lowest of the three catalysts. The observed effect seems to correlate with the electronic structures of these metals. The Fe-C catalyst, having the strongest M-C bonds, has the highest chain growth probability. This could be due to a higher availability of H-atoms on the catalyst surface, corresponding to weaker M-C bonds. The molybdenum and tungsten carbides have weaker M-C bonds and therefore less H-atoms available on the catalyst surface; hence lower chain growth probabilities.

This implies that chain growth is promoted by a higher electron density on the catalyst. Iron appears to be a better polymerisation catalyst than the early transition metal carbides. These early transition metal carbides have been reported to be good methanation catalysts (Ranhotra et al., 1987) and were reported to have methane as the main hydrocarbon product formed in Fischer-Tropsch synthesis (Patterson et al., 2003). The observations by these researchers correspond well to the observed chain growth probabilities in these carbides.

4.3.4 Hydrogenation of primary olefins

The olefin content in the Fischer-Tropsch product can yield information about the extent to which primarily formed olefins are hydrogenated. The olefin content in the hydrocarbon products formed over the transition metal carbides shows a trend corresponding to the M-C bond strength on the metal carbide catalysts (lower olefin content on early transition metal carbides). The effect of the catalyst surface on the olefin content indicates that the early transition metal carbides show increased hydrogenation activity, due to higher surface hydrogen availability. The early transition metal carbides have previously also been reported to show high hydrogenation activity (Vidick et al., 1986).

4.3.5 Double bond isomerisation

The 1-olefin content in the olefins formed in the Fischer-Tropsch reaction gives an indication of the extent to which double bond isomerisation of the primary olefins is taking place. The extent of the double bond isomerisation reaction on the Fe-C catalyst seems to be minimal. The molybdenum and tungsten carbides have mostly internal olefins present in the olefins, indicating that the primary olefins are readily being isomerised on the catalyst surface. The early transition metal carbides have been investigated in terms of performance as hydroisomerisation catalysts (Ledoux et al., 1992; Ribeiro et al., 1991a; Ribeiro et al., 1991b), and were found to show reasonable activity. Considering that for a double bond shift to take place the addition and removal of hydrogen is involved, this reaction can also be seen as hydroisomerisation. The effect observed in the 1-olefin content is indicating that the hydroisomerisation activity on the early transition carbides is higher than on the Fe-C. This can be explained by the availability of surface hydrogen on the catalyst as a result of the M-C bonds strength.

5. Conclusion

The main objective of this study was to determine the Fischer-Tropsch activity and selectivity of transition metal (iron, molybdenum and tungsten) carbides. The comparison of these materials in terms of performance as Fischer-Tropsch catalyst would then be possible.

The preparation of the carbides only resulted in a phase pure species for the tungsten (WC). The prepared molybdenum carbide was a mixture of Mo_2C and other carbide phases. The iron catalyst prepared was a mixture of metallic iron and cementite (Fe_3C).

A higher specific activity was observed on the iron carbide/metallic iron catalyst than on the early transition metal carbides. This was explained in terms of the electronic structure of the metal carbides, and therefore the strength of the metal-carbon (from CO dissociation) bond. The number of valence electrons on the metals was used to explain this difference in activity. The lower activity observed on the tungsten carbide than on the molybdenum carbide could be explained by the additional electron shell on the tungsten metal, compared to the molybdenum carbide.

The water-gas shift activity was also observed on these catalysts. The water-gas shift activity on the molybdenum carbide was found to be negative, while on the tungsten carbide a positive or negative activity could be obtained. The iron catalyst had positive water-gas shift activity. These activities were very close to zero in all cases, indicating water-gas shift equilibrium being approximated at these operating conditions.

The product selectivity on the iron carbide/metallic iron catalyst was more suited to Fischer-Tropsch synthesis. The early transition metal carbides yielded high methane selectivity, and chain growth probabilities of less than 0.45 were observed for these two carbide catalyst. The olefin content was

also found to be lower than in the iron carbide/metallic iron catalyst, with the level of 1-olefins in this olefin product also considerably lower than on the iron carbide/metallic iron catalyst. These observations could be explained by the availability of H-atoms on the catalyst surface, as a result of the observed M-C bond strength on the catalysts.

The conversion obtained on the iron catalysts led to oxidation, since the conversion was above the limiting conversion for the material. The iron carbide catalyst was initially a mixture of cementite and metallic iron, but transformed to a mixture of magnetite and Hägg carbide. The molybdenum and tungsten carbides were stable under Fischer-Tropsch conditions.

6. References

Anderson, R.B.
"The Fischer-Tropsch synthesis"
Academic Press Inc., London (1984), 31.

Bian, G., Fan, L., Fu, Y., Fujimoto, K.
High temperature calcined K-MoO_3/γ-Al_2O_3 catalysts for mixed alcohols synthesis from syngas: Effects of Mo loadings.
Applied Catalysis A: General **170** (1998), 255.

Biel, H.
The effect of water partial pressure on low temperature iron Fischer-Tropsch reaction rate, selectivity and catalyst structure.
MSc Thesis, University of Cape Town (2005).

Boudart, M., Oyama, S.T., Leclercq, L.
"Proceedings of the 7th International Congress of Catalysis"
(Seiyama, T., Tanabe, K., Eds.), Kodansha, Tokyo, vol. 1, (1980), 578.

Brewer, L.
"Phase Stability in Metals and Alloys"
(Rudman, P., Stringer, J., Jaffee, R.K., Eds.), McGraw-Hill, New York (1967), 39-61, 241-249, 344-346 and 560-568.

Brewer, L.
The responsibility of high temperature scientists.
High Temperature Science **16** (1984), 1.

Claeys, M.
Selektivität, Elementarschritte und kinetische Modellierung bei der Fischer-Tropsch-Synthese.
PhD Thesis, University of Karsruhe (1997).

Claeys, M. and van Steen, E.
"Studies in Surface Science and Catalysis"
(Steynberg, A., Dry, M., Eds.), Elsevier Science, B.V., vol. 152 (2004), 601.

Colling C.W. and Thompson, L.T.
The structure and function of supported molybdenum nitride hydro-denitrogenation catalysts.
Journal of Catalysis **146** (1994), 193.

Craxford, S.R. and Rideal, E.
Die Fischer-Tropsch-Synthese von Kohlenwasserstoffen und einige verwante Reaktionen.
Brennstof Chemie **20** (1939), 263.

Dry, M.E.
"Catalysis Science and Technology"
(Anderson, J.R., Boudart, M., Eds.), Springer, Berlin, vol. 1, (1981), 195-209.

Dry, M.E.
The Fischer-Tropsch process - commercial aspects.
Catalysis Today **6** (1990), 183.

Dry, M.E.
Practical and theoretical aspects of the catalytic Fischer-Tropsch process.
Applied Catalysis A: General **138** (1996), 319.

Dun, J.W., Gulari, E., Ng, K.Y.S.
Fischer-Tropsch synthesis on charcoal-supported molybdenum: The effect of preparation conditions and potassium promotion on activity and selectivity.
Applied Catalysis **15** (1985), 247.

Dwyer, D.J. and Hardenberg, J.H.
The catalytic reduction of carbon monoxide over iron surfaces: A surface science investigation.
Journal of Catalysis **87** (1984), 66.

Eliason, S.A. and Bartholomew, C.H.
Reaction and deactivation kinetics for Fischer-Tropsch synthesis on unpromoted and potassium promoted iron catalysts.
Applied Catalysis A: General **186** (1999), 229.

Engel, N.
Some new viewpoints on the metallic bond.
Ingenioeren **N101** (1939).

Fischer, F. and Tropsch, H.
Übe die Herstellung synthetischer Ölgemische (Synthol) durch Aufbau aus Kohlenoxyd und Wasserstoff.
Brennstof Chemie **7** (1926), 97.

Herranz, T., Rojas, S., Pérez-Alonso, F.J., Ojeda, M., Terreros, P.,
Fierro, J.L.G.
Genesis of iron carbides and their role in the synthesis of hydrocarbons from synthesis gas.
Journal of Catalysis **243** (2006), 199.

Iglesia, E.
Design, synthesis, and use of cobalt-based Fischer-Tropsch synthesis catalysts.
Applied Catalysis A: General **161** (1997), 59.

Kapoor, R. and Oyama, S.T.
Synthesis of high surface area vanadium nitride.
Journal of Solid State Chemistry **99** (1992), 303.

Knacke, O., Kubaschewski, O., Hesselmann, K.
"Thermochemical Properties of Inorganic Substances"
Springer-Verlag, Berlin, 2nd ed. (1991).

Ledoux, M.J., Huu, C.P., Guille, J., Dunlop, H.
Compared activities of platinum and high specific surface area Mo_2C and WC catalysts for reforming reactions: I. Catalyst activation and stabilization: Reaction of n-hexane.
Journal of Catalysis **134** (1992), 383.

Lee, J.S., Oyama, S.T., Boudart, M.
Molybdenum carbide catalysts I. Synthesis of unsupported powders.
Journal of Catalysis **106** (1987), 125.

Lee, J.S., Volpe, L., Ribeiro, F.H., Boudart, M.
Molybdenum carbide catalysts II. Topotactic synthesis of unsupported powders.
Journal of Catalysis **112** (1988), 44.

Lee, J.S., Yeom, M.H., Park, K.Y., Nam, I.-S., Chung, J.S., Kim, Y.G., Moon, S.H.
Preparation and benzene hydrogenation activity of supported molybdenum carbide catalysts.
Journal of Catalysis **128** (1991), 126.

Lee, K.S., Abe, H., Reimer, J.A., Bell, A.T.
Hydrodenitrogenation of Quinoline over High-Surface-Area Mo_2N.
Journal of Catalysis **139** (1993), 34.

Li, S., Meitzner, G., Iglesia, E.
Structure and site evolution of iron oxide catalyst precursors during the Fischer-Tropsch synthesis.
Journal of Physical Chemistry B **105** (2001), 5743.

Li, S., Ding, W., Meitzner, G.D., Iglesia, E.
Spectroscopic and transient kinetic studies of site requirements in iron-catalyzed Fischer-Tropsch synthesis.
Journal of Physical Chemistry B **106** (2002), 85.

Loaiza-Gil, A., Fontal, B., Rueda, F., Mendialdua, J., Casanova, R.
On carbonaceous deposit formation in carbon monoxide hydrogenation on a natural iron catalyst.
Applied Catalysis A: General **177** (1999), 193.

Luo, M. and Davis, B.H.
Fischer–Tropsch synthesis: Group II alkali-earth metal promoted catalysts.
Applied Catalysis A: General **246** (2003), 171.

Maitlis, P.M., Long, H.C., Quyoum, R., Turner, M.L., Whang, Z.-Q.
Heterogeneous catalysis of C-C bond formation: black art or organometallic science.
Journal of Chemical Society Chemical Communications (1996), 1.

Maitlis, P.M., Quyoum, R., Long, H.C., Turner, M.L.
Towards a chemical understanding of the Fischer–Tropsch reaction: alkene formation.
Applied Catalysis A: General **186** (1999), 363.

Malan, O., Louw, J., Ferreira, L.
Eisencarbidphasen in Benzin-Sinthese-Katalysatoren.
Brennstoff Chemie **42** (1961), 209.

Markel, E.J., Van Zee, J.W.
Catalytic hydrodesulfurization by molybdenum nitride.
Journal of Catalysis **126** (1990), 643.

McGee, R.C.V., Bej, S.K., Thompson, L.T.
Basic properties of molybdenum and tungsten nitride catalysts.
Applied Catalysis A: General **284** (2005), 139.

Nagai, M. and Miyao, T.
Hydrodesulfurization of dibenzothiophene on alumina-supported molybdenum nitride.
Catalysis Letters **18** (1993), 9.

Niemantsverdriet, J.W., van der Kraan, A.M., van Dijk, W.L.,
van der Baan, H.S.
Behavior of metallic iron catalysts during Fischer-Tropsch synthesis studied with Moessbauer spectroscopy, x-ray diffraction, carbon content determination, and reaction kinetic measurements.
Journal of Physical Chemistry **84** (1980), 3363.

Ning, W., Koizumi, N., Chang, H., Mochizuki, T., Itoh, T., Yamada, M.
Phase transformation of unpromoted and promoted Fe catalysts and the formation of carbonaceous compounds during Fischer-Tropsch synthesis reaction.
Applied Catalysis A: General **312** (2006), 35.

Oyama, S.T.
PhD Thesis, Stanford University (1981).

Oyama, S.T.
Crystal structure and chemical reactivity of transition metal carbides and nitrides.
Journal of Solid State Chemistry **96** (1992a), 442.

Oyama, S.T.
Kinetics of ammonia decomposition on vanadium nitride.
Journal of Catalysis **133** (1992b), 358.

Oyama, S.T.
Preparation and catalytic properties of transition metal carbides and nitrides.
Catalysis Today **15** (1992c), 179.

Oyama, S.T.
"The Chemistry of Transition Metal Carbides and Nitrides"
Blackie Academic and Professional, London (1996).

Patterson, P.M., Das, T.K., Davis, B.H.
Carbon monoxide hydrogenation over molybdenum and tungsten carbides.
Applied Catalysis A: General **251** (2003), 449.

Patzlaff, J., Liu, Y., Graffmann, C., Gaube, J.
Studies on product distributions of iron and cobalt Fischer-Tropsch synthesis.
Applied Catalysis A: General **187** (1999), 109.

Pichler, H. and Schulz, H.
Neuere Erkenntnisse auf dem Gebiet der Synthese von Kohlenwasserstoffen aus CO und H_2.
Chemie Ingenieur Technik **42** (1970), 1162.

Ranhotra, G.S., Bell, A.T., Reimer, J.A.
Catalysis over molybdenum carbides and nitrides : II. Studies of CO hydrogenation and C_2H_6 hydrogenolysis.
Journal of Catalysis **108** (1987), 40.

Ribeiro, F.H., Boudart, M., Dalla Betta, A., Iglesia, E.
Catalytic reactions of n-alkanes on β-W_2C and WC: The effect of surface oxygen on reaction pathways.
Journal of Catalysis **130** (1991a), 498.

Ribeiro, F.H., Dalla Betta, A., Boudart, M., Baumgartner, J., Iglesia, E.
Reactions of neopentane, methylcyclohexane, and 3,3-dimethylpentane on tungsten carbides: The effect of surface oxygen on reaction pathways.
Journal of Catalysis **130** (1991b), 86.

Sajkowski, D.J. and Oyama, S.T.
Catalytic hydrotreating by molybdenum carbide and nitride: unsupported Mo_2N and Mo_2C/Al_2O_3.
Applied Catalysis A: General **134** (1996), 339.

Schlatter, J.C., Oyama, S.T., Metcalfe, J.E., Lambert, Jr., J.M.
Catalytic behavior of selected transition metal carbides, nitrides, and borides in the hydrodenitrogenation of quinoline.
Industrial and Engineering Chemistry Research **27** (1988), 1648.

Schulz, H. and Claeys, M.
Reactions of α-olefins of different chain length added during Fischer–Tropsch synthesis on a cobalt catalyst in a slurry reactor.
Applied Catalysis A: General **186** (1999), 90.

Schulz, H. Nie, Z., Ousmanov, F.
Construction of the Fischer–Tropsch regime with cobalt catalysts.
Catalysis Today **71** (2002), 351.

Shroff, M.D., Kalakkad, D.S., Coulter, K.E., Köhler, S.D., Harrington, M.S., Jackson, N.B., Sault, A.G., Datye, A.K.
Activation of precipitated iron Fischer-Tropsch synthesis catalysts.
Journal of Catalysis **156** (1995), 185.

Storch, H.H., Golumbic, N., Anderson, R.B.
"The Fischer-Tropsch and Related Synthesis"
John Wiley & Sons, New York (1951).

Storms, E.K.
"The Refractory Carbides"
Academic Press, New York (1967).

Toth, L.E.
"Transition Metal Carbides and Nitrides"
Academic Press, New York (1971).

Vannice, M.A.
The catalytic synthesis of hydrocarbons from H_2/CO mixtures over the group VIII metals I. The specific activities and distributions of supported metals.
Journal of Catalysis **37** (1975), 449.

Vidick, B., Lemaitre, J., Leclercq, L.
Control of the catalytic activity of tungsten carbides : III. Activity for ethylene hydrogenation and cyclohexane dehydrogenation.
Journal of Catalysis **99** (1986), 439.

Volpe, L. and Boudart, M.
Compounds of molybdenum and tungsten with high surface area I. Nitrides.
Journal of Solid State Chemistry **59** (1985a), 332.

Volpe, L. and Boudart, M.
Compounds of molybdenum and tungsten with high surface area II. Carbides.
Journal of Solid State Chemistry **59** (1985b), 348.

Volpe, L. and Boudart, M.
Topotactic preparation of powders with high specific surface area.
Catalysis Reviews. Science and Engineering **27** (1985c), 515.

Woo, H.C., Park, K.Y., Kim, H.G., Nam, I.S., Chung, J.S., Lee, J.S.
Mixed alcohol synthesis from carbon monoxide and dihydrogen over potassium-promoted molybdenum carbide catalysts.
Applied Catalysis A: General **75** (1991), 349.

7. Appendices

Appendix A: XRD reference patterns

The reference patterns of a particular phase of species are in each case matched to the observed peaks. The peaks that cannot be distinguished are in most cases due to overlapping of the peaks and in only a few cases, due to the noise levels in the spectrum.

A.1 Iron oxide

Fe_2O_3 Reference peaks		Observed peaks	
2 theta	Intensity	2 theta	Intensity
24.1	30	24.1	30
33.2	100	33.2	90
35.6	70	35.6	100
40.9	20	40.9	30
49.5	40	49.5	40
54.1	45	54.1	50
57.4	5	57.4	5
57.6	10	57.6	10
62.4	30	62.4	30
64.0	30	64.0	30
71.9	10	71.9	10
72.3	6	72.3	6
75.4	8	75.4	8

A.2 Molybdenum oxide

MoO_3 Reference peaks		Observed peaks	
2 theta	Intensity	2 theta	Intensity
23.3	82	23.3	50
25.7	61	25.7	60
27.3	100	27.3	100
29.7	13	29.7	10
33.1	19	33.1	19
33.7	35	33.7	35
34.4	6	34.4	-
35.5	12	35.5	12
38.6	12	38.6	12
39.0	31	39.0	31
39.7	18	39.7	18
42.4	9	42.4	-
45.7	13	45.7	15
46.3	17	46.3	17
49.2	21	49.2	21
50.0	11	50.0	11
51.6	5	51.6	5
52.0	5	52.0	5
52.8	17	52.8	17
54.1	8	54.1	8
55.2	13	55.2	15
56.4	13	56.4	13
57.7	15	57.7	11
58.1	6	58.1	-
58.8	16	58.8	16
61.6	5	61.6	-
62.9	10	62.9	10
64.5	12	64.5	12
64.9	12	64.9	12
66.8	5	66.8	-
67.5	5	67.5	5
69.5	6	69.5	6

A.3 Tungsten oxide

WO_3 Reference peaks		Observed peaks	
2 theta	Intensity	2 theta	Intensity
23.1	100	23.1	100
23.6	97	23.6	90
24.4	99	24.4	97
26.6	19	26.6	20
28.6	16	28.6	17
28.9	17	28.9	17
33.3	39	33.3	40
33.6	27	33.6	25
34.2	62	34.2	60
35.4	6	35.4	6
35.7	6	35.7	6
41.4	14	41.4	14
41.9	14	41.9	14
46.0	5	46.0	5
47.3	9	47.3	9
48.2	9	48.2	9
49.9	24	49.9	25
50.3	13	50.3	13
50.7	12	50.7	12
50.8	9	50.8	9
53.5	12	53.5	12
53.7	8	53.7	10
54.2	9	54.2	9
54.3	8	54.3	8
54.8	10	54.7	10
55.0	7	55.0	-
55.4	8	55.4	-
55.6	8	55.6	-
55.8	10	55.8	10
56.0	18	56.0	18
56.1	15	56.1	-

A.4 Iron nitride

Fe_2N Reference peaks		Observed peaks	
2 theta	Intensity	2 theta	Intensity
37.4	14	37.4	15
40.9	20	40.9	20
42.8	100	42.8	100
56.6	25	56.6	25
67.6	2	68.0	20
75.7	25	75.7	25

A.5 Molybdenum nitride

Mo_2N Reference peaks		Observed peaks	
2 theta	Intensity	2 theta	Intensity
37.4	100	37.4	100
43.4	48	43.4	70
63.1	30	63.1	50
75.7	40	75.7	40
79.7	12	79.7	10

A.6 Tungsten nitride

W_2N Reference peaks		Observed peaks	
2 theta	Intensity	2 theta	Intensity
37.7	100	37.7	100
43.8	47	43.8	75
63.7	33	63.7	50
76.5	44	76.5	44

A.7 Iron carbide/Metallic iron

Fe_3C Reference peaks		Observed peaks	
2 theta	Intensity	2 theta	Relative intensity
37.7	25	37.7	3
37.8	35	37.8	4
39.8	40	39.8	4
40.6	35	40.6	3
42.9	80	42.9	8
43.7	100	43.7	10
44.6	45	44.6	-
45.0	45	45.0	-
45.8	65	45.8	7
48.6	20	48.6	5
49.1	45	49.1	6
51.8	14	51.8	2
54.4	12	54.4	2
56.0	10	56.0	1
58.0	25	58.0	2
59.7	8	59.7	1
61.3	10	61.3	2
70.8	10	70.8	1
77.9	14	77.9	2
78.5	8	78.5	1
Fe Reference peaks		Observed peaks	
44.7	100	44.7	100
65.0	20	65.0	20

A.8 Molybdenum carbides

Mo_2C Reference peaks		Observed peaks	
2 theta	Intensity	2 theta	Relative intensity
34.4	20	34.4	20
38.0	25	38.0	25
39.4	100	39.4	100
52.1	20	52.1	20
61.5	17	61.5	30
69.6	17	69.6	20
74.6	15	74.6	25
75.5	10	75.5	15
α-MoC_{1-x}		Observed peaks	
36.2	100	36.2	15
42.5	80	42.5	10
61.5	50	61.5	- (overlapping)
73.7	30	73.7	5
77.9	30	77.9	7

A.9 Tungsten carbide

WC Reference peaks		Observed peaks	
2 theta	Intensity	2 theta	Intensity
31.5	45	31.5	60
35.6	100	35.6	80
48.3	100	48.3	100
64.0	20	64.0	20
65.7	6	65.7	6
73.1	25	73.1	45
75.4	14	75.4	15
77.1	30	77.1	30

A.10 Spent iron catalysts

Fe_3O_4 Reference peaks		Observed peaks	
2 theta	Intensity	2 theta	Intensity
30.1	30	30.1	30
35.4	100	35.4	100
37.1	8	37.1	10
43.1	20	43.1	20
53.4	10	53.4	10
56.9	30	56.9	30
62.5	40	62.5	40
73.9	10	73.9	10
Fe_5C_2 Reference peaks		Observed peaks	
34.2	10	34.2	10
36.2	20	36.2	20
37.6	20	37.6	20
39.9	50	39.9	30
41.4	50	41.4	50
43.9	100	43.9	100
44.6	100	44.6	100
45.8	20	45.8	60
47.6	50	47.6	30
50.7	70	50.7	40
51.9	10	51.9	10
53.2	10	53.2	10
54.9	10	54.9	10
56.8	10	56.8	10
58.8	70	58.8	40
61.8	10	61.8	10
68.4	10	68.4	10
70.2	10	70.2	10
71.4	10	71.4	10
74.7	20	74.7	20
76.1	20	76.1	20
79.1	50	79.1	50

Appendix B: TCD data for Fischer-Tropsch synthesis

Time on stream TCD data – Fe-O I catalyst							
TOS	TCD areas						X_{CO},
(Hrs)	H_2	Ar	N_2	CO	CH_4	CO_2	mol%
17.33	48.50	24.77	0.44	3.69	1.25	17.69	78.94
40.83	50.03	25.90	0.46	3.65	1.51	15.79	80.63
63.91	44.01	26.25	1.57	3.88	1.67	15.74	79.65

Time on stream TCD data – Fe-O II catalyst							
TOS	TCD areas						X_{CO},
(Hrs)	H_2	Ar	N_2	CO	CH_4	CO_2	mol%
22.67	49.05	27.15	0.52	2.75	2.27	16.54	85.88
46.25	48.36	27.10	0.52	2.65	2.96	16.43	86.29
72.75	46.96	27.29	0.53	2.46	3.22	16.51	87.51

Time on stream TCD data – Fe-C catalyst							
TOS	TCD areas						X_{CO},
(Hrs)	H_2	Ar	N_2	CO	CH_4	CO_2	mol%
17.83	53.71	23.33	0.41	7.10	1.38	13.14	57.19
39.66	53.18	23.49	0.40	6.28	1.70	13.41	62.01
63.82	52.21	23.65	0.41	5.91	1.87	13.68	64.52
87.65	51.58	24.21	0.42	5.23	2.11	14.07	69.23

Time on stream TCD data – Mo-C catalyst							
TOS	TCD areas						X_{CO},
(Hrs)	H_2	Ar	N_2	CO	CH_4	CO_2	mol%
18.75	54.85	19.88	0.39	13.83	0.54	10.59	5.92
50.92	53.77	19.77	0.42	14.22	0.58	10.34	6.29
65.42	54.44	19.87	0.40	14.01	0.57	10.53	6.90
88	55.06	19.97	0.40	13.75	0.60	10.56	6.84

Time on stream TCD data – W-C catalyst							
TOS	TCD areas						X_{CO},
(Hrs)	H_2	Ar	N_2	CO	CH_4	CO_2	mol%
19.75	55.07	21.82	0.38	12.79	0.55	10.01	19.05
41.83	55.72	20.64	0.43	12.13	0.68	10.42	18.39
66.33	55.72	20.54	0.38	11.79	0.71	10.38	19.66
89.49	55.54	20.57	0.36	11.69	0.70	10.46	19.73

Appendix C: Fischer-Tropsch synthesis FID data (%C-atom selectivity)

Fe-O I catalyst – TOS 41 hrs							
N_C	n-Par	i-Par	1-Ol	int-Ol	i-Ol	Ox	Total
1	10.55	0.00	0.00	0.00	0.00	0.80	11.36
2	2.25	0.00	7.15	2.15	0.00	1.58	13.13
3	1.33	0.00	11.83	0.00	0.00	1.33	14.49
4	0.92	0.00	9.05	0.50	0.00	0.62	11.09
5	0.73	0.00	5.67	0.33	0.07	0.50	7.29
6	0.54	0.20	4.29	0.49	1.12	0.01	6.80
7	0.39	0.37	2.91	0.85	0.58	0.12	5.22
8	0.31	0.42	2.04	0.20	0.72	0.12	3.81
9	0.19	0.62	1.27	0.25	0.85	0.12	3.30
10	0.14	0.38	0.89	0.77	0.42	0.04	2.64
11	0.11	0.06	0.63	0.41	0.42	0.04	1.66
12	0.09	0.16	0.42	0.22	0.38	0.01	1.27
13	0.06	0.15	0.30	0.11	0.42	0.00	1.05
14	0.05	0.11	0.19	0.01	0.14	0.00	0.50
15	0.03	0.02	0.11	0.00	0.07	0.00	0.23
16	0.03	0.00	0.09	0.00	0.06	0.00	0.18
17	0.02	0.00	0.05	0.00	0.02	0.00	0.09
18	0.01	0.00	0.03	0.00	0.00	0.00	0.04
19	0.01	0.00	0.02	0.00	0.00	0.00	0.03
20	0.01	0.00	0.01	0.00	0.00	0.00	0.02

Fe-O II catalyst – TOS 46 hrs							
N_C	n-Par	i-Par	1-Ol	int-Ol	i-Ol	Ox	Total
1	17.86	0.00	0.00	0.00	0.00	0.80	18.66
2	6.80	0.00	3.61	0.00	0.00	1.47	11.88
3	3.71	0.00	11.30	0.00	0.00	1.00	16.01
4	2.14	0.00	6.00	3.27	0.00	0.25	11.67
5	1.68	0.00	3.15	2.29	0.05	0.14	7.29
6	1.37	0.19	2.20	1.31	0.26	0.01	5.34
7	1.09	0.51	1.15	0.80	0.20	0.06	3.80
8	0.73	0.44	0.75	0.83	0.18	0.03	2.26
9	0.60	0.43	0.36	0.76	0.20	0.03	2.38
10	0.46	0.43	0.23	0.72	0.22	0.01	2.06
11	0.34	0.18	0.14	0.44	0.16	0.01	1.26
12	0.25	0.14	0.11	0.23	0.22	0.00	0.96
13	0.19	0.15	0.06	0.07	0.22	0.00	0.69
14	0.15	0.15	0.05	0.08	0.09	0.00	0.52
15	0.13	0.01	0.02	0.00	0.09	0.00	0.26
16	0.09	0.00	0.02	0.00	0.05	0.00	0.15
17	0.01	0.00	0.08	0.00	0.02	0.00	0.10
18	0.00	0.00	0.05	0.00	0.00	0.00	0.06

Fe-C catalyst – TOS 40 hrs							
N_C	n-Par	i-Par	1-Ol	int-Ol	i-Ol	Ox	Total
1	19.89	0.00	0.00	0.00	0.00	0.84	20.73
2	5.16	0.00	6.31	0.00	0.00	1.28	12.76
3	2.22	0.00	12.78	0.00	0.00	1.15	16.15
4	1.36	0.00	8.17	1.31	0.00	0.37	11.21
5	0.92	0.00	4.61	0.76	0.07	0.19	6.46
6	0.68	0.06	3.15	0.57	0.14	0.00	4.64
7	0.47	0.17	1.95	0.48	0.18	0.06	3.31
8	0.29	0.19	1.00	0.19	0.30	0.06	2.02
9	0.26	0.26	0.74	0.30	0.37	0.04	1.96
10	0.24	0.26	0.65	0.50	0.30	0.01	1.95
11	0.20	0.03	0.48	0.35	0.21	0.02	1.30
12	0.16	0.10	0.34	0.20	0.22	0.01	1.03
13	0.15	0.11	0.24	0.06	0.22	0.00	0.78
14	0.13	0.12	0.17	0.10	0.11	0.00	0.62
15	0.14	0.03	0.12	0.00	0.08	0.00	0.37
16	0.12	0.00	0.08	0.00	0.10	0.00	0.30
17	0.10	0.00	0.06	0.00	0.01	0.00	0.18
18	0.08	0.00	0.05	0.00	0.00	0.00	0.13
19	0.07	0.00	0.03	0.00	0.00	0.00	0.10
20	0.02	0.00	0.07	0.00	0.00	0.00	0.09
21	0.01	0.00	0.06	0.00	0.00	0.00	0.07
22	0.01	0.00	0.05	0.00	0.00	0.00	0.06

Mo-Ccatalyst – TOS 51 hrs							
N_C	n-Par	i-Par	1-Ol	int-Ol	i-Ol	Ox	Total
1	52.59	0.00	0.00	0.00	0.00	1.37	53.96
2	15.91	0.00	3.83	0.00	0.00	1.62	19.74
3	5.89	0.00	5.95	0.00	0.00	0.71	12.55
4	1.98	0.00	1.85	1.77	0.00	0.00	5.61
5	1.04	0.00	0.77	0.91	0.12	0.00	2.84
6	0.62	0.00	0.34	0.44	0.13	0.00	1.40
7	0.35	0.00	0.18	0.11	0.19	0.00	0.64
8	0.22	0.00	0.00	0.00	0.00	0.00	0.22

W-C catalyst – TOS 42 hrs							
N_C	n-Par	i-Par	1-Ol	int-Ol	i-Ol	Ox	Total
1	27.69	0.00	0.00	0.00	0.00	2.07	29.76
2	13.10	0.00	3.84	0.00	0.00	1.46	18.40
3	7.55	0.00	8.88	0.00	0.00	1.03	17.46
4	3.37	0.00	2.50	4.76	0.00	0.00	10.63
5	1.96	0.00	0.65	2.41	0.08	0.00	5.10
6	1.28	0.00	0.40	1.21	0.00	0.00	2.89
7	0.80	0.28	0.21	0.50	0.52	0.00	2.32

Appendix D: Atomic absorption spectroscopy (AAS)

Atomic absorption spectroscopy uses the absorption of light to measure the concentration of gas-phase atoms. Since samples in this study are solids, the analyte atoms or ions must be vaporized in a flame. The atoms absorb ultraviolet or visible light leading to transitions to higher electronic energy levels. The analyte concentration is determined from the amount of light absorption. Concentration measurements are determined from a working curve after calibrating the instrument with standards of known concentration.

The AAS analyses were done by digesting the finely milled samples in aqua regia with the addition of hydrofluoric acid and perchloric acid. The sample is made up to a known volume, filtered and read on the AA spectrophotometer. The spectrophotometer used was a manual Varian AA30 instrument with a nitrous oxide flame to reduce interferences. This analysis was only performed on iron and molybdenum oxides, since a tungsten lamp was not available.

The sample (0.1 g) was weighed out into a 250 ml wide-mouthed Erlenmeyer flask. 10 ml of HCl/HF mixture (30 vol% HCl) was added and heated to 80 °C. 10 ml HNO_3 (60%) was carefully added into the flask and the mixture was allowed to evaporate at 80 °C until about 2 ml remained in the flask. After this, 5 ml of concentrated $HClO_4$ was added into the flask and the mixture was again boiled until 2 ml of the sample remained in the flask. This was then transferred to a 100 ml volumetric flask and made up with distilled water. The samples were subsequently read on the spectrophotometer. Elemental compositions in the catalyst samples were obtained by combining oxygen balance and concentration ratios from AAS results.

Atomic absorption spectroscopy was used to ascertain the metal content in the oxide precursors. The concentration value obtained from the analysis was converted into a percentage. To convert the concentration value obtained from AAS data to a weight percentage metal in the species, the following calculation was done:

$$M(wt\%) = \frac{c}{m \times 100}$$

where c is the concentration in mg/l (ppm) obtained from AAS, m is the mass of sample digested and made up to 100 ml for measurement.

The metal content in iron oxide and molybdenum oxide are shown in Table 3.10, compared to the metal content expected from the molecular formula of that particular compound.

Table D1: Metal content in oxides

Species	Metal measured (wt %)	Metal calculated (wt %)
Iron oxide	71.4	69.9
Molybdenum oxide	38.3	66.7
Molybdenum oxide (fresh 1)	45.7	66.7
Molybdenum oxide (fresh 2)	24.5	66.7
Molybdenum oxide (fresh 3)	14.5	66.7
Molybdenum oxide (fresh 4)	79.9	66.7
Molybdenum oxide (fresh 5)	49.1	66.7

The iron content in iron oxide is within the error of the instrument and corresponds to the Fe_2O_3 phase. The molybdenum content, however, showed a lower measured value. MoO_3 is known to be relatively non-hygroscopic and fairly stable in air, which indicated that there was an error in the measurement. The AAS was therefore repeated using freshly calcined MoO_3. Four samples of the same species were submitted. Digestion was done using

the method described in the experimental section for the first three samples. In each case there was a precipitate that formed. The fourth sample was therefore digested using only aqua regia, while the fifth was done in a 25% ammonia solution. The results indicate that the measured molybdenum content is inconsistent, irreproducible and sensitive to the way in which digestion was done.